

Application of satellite SAR interferometry to the observation  
of ground surface deformations

July 2019

يۈسۈپجان ئەمەت

Yusupjiang Aimaiti

Graduate School of Engineering

CHIBA UNIVERSITY

(千葉大学審査学位論文)

Application of satellite SAR interferometry to the observation  
of ground surface deformations

2019 年 7 月

千葉大学大学院工学研究科

建築・都市科学専攻都市環境システムコース

ユスプジャン アイマイテイ

# Abstract

Ground surface deformations due to human and naturally induced factors are geohazards and may cause damage to buildings and other infrastructures. Excessive ground movements can even lead to loss of human lives. Therefore, Identifying and regularly monitoring the ground deformations is crucial before it could become latent risk factors. Interferometric synthetic aperture radar (InSAR) technique provides an all-weather imaging capability for measuring continuous ground surface deformation and detecting minor surface changes. In this research, several InSAR techniques were applied to multi-satellite SAR images to monitor the surface deformation induced by human activities and natural causes.

The first case study was conducted for the Xinjiang Uyghur Autonomous Region, China. The land-surface deformation was investigated in Karamay, a typical oil-producing city, using both ALOS PALSAR and ENVISAT ASAR data. Two-pass differential SAR interferometry (D-InSAR), Persistent Scatterer (PS-InSAR) and Small Baseline Subset (SBAS-InSAR) processes were applied to the two datasets. The influences caused by the different band wavelengths and the methods were compared and discussed. The second case was conducted in Urayasu City, Chiba Prefecture. The long-term land deformation patterns were investigated using ERS-1/-2 (C-band), ALOS PALSAR and ALOS-2 PALSAR-2 (L-band) images. Comparing with the leveling data obtained by field surveys, the results obtained by InSAR techniques showed good agreement. The last case study was detecting the landslides induced by the 2018 Hokkaido Eastern-Iburi Earthquake. The coherence and the intensity difference were calculated from the pre- and post-event ALOS-2 PALSAR-2 images to extract changed regions. The results were verified by comparing with optical satellite images and truth data. The outcome of this research further proves the suitability and effectiveness of InSAR measurements in the ground surface deformation monitoring.

**Keywords:** ERS-1/-2; ENVISAT-ASAR; PALSAR; PALSAR-2; ground surface deformation; D-InSAR; PS-InSAR; SBAS-InSAR

## Table of contents

<b>Table of contents</b> .....	ii
<b>Acknowledgments</b> .....	v
<b>Curriculum Vitae</b> .....	vi
<b>Publications</b> .....	vii
<b>1. Introduction</b> .....	1
1.1. Background and objective .....	1
1.2. Outline of the thesis.....	2
<b>2. Theoretical concepts of SAR interferometry</b> .....	4
2.1. Synthetic Aperture Radar (SAR).....	4
2.2. SAR sensors .....	5
2.2.1. ERS-1/-2 and ENVISAT ASAR .....	6
2.2.2. ALOS PALSAR and ALOS-2 PALSAR-2 .....	8
2.3. InSAR.....	11
2.4. Multi-temporal InSAR-stacking technique .....	14
<b>3. Monitoring of Land-Surface Deformation in the Karamay Oilfield, Xinjiang, China Using SAR Interferometry</b> .....	15
3.1. Introduction .....	15
3.2. Study Area and Data Sets .....	17
3.2.1. Study area .....	17
3.2.2. Data Sets .....	18
3.3. Methodology .....	19
3.3.1. D-InSAR.....	19
3.3.2. PS and SBAS-InSAR .....	19

3.3.3. Pearson Correlation Coefficient and Root Mean Square Error .....	21
3.4. Results and Analysis.....	21
3.4.1. Results of D-InSAR Interferometry .....	21
3.4.2. Results of PS and SBAS-InSAR Interferometry .....	24
3.5. Comparison and Discussion .....	29
3.6. Conclusion.....	31
<b>4. Multi-Sensor InSAR Analysis of Progressive Land Subsidence over the Coastal City of Urayasu, Japan.....</b>	<b>32</b>
4.1. Introduction .....	32
4.2. Study area.....	34
4.3. Data Sets and Methods .....	35
4.3.1. Data Sets.....	35
4.3.2 Methodology.....	36
4.4. Results .....	40
4.4.1. Time-Series Analysis of the ERS-1/-2 Data from May 1993 to February 2006 .....	40
4.4.2. Time-Series Analysis of the PALSAR Data from June 2006 to December 2010 .....	45
4.4.3. Time-Series Analysis of the PALSAR-2 Data from December 2014 to November 2017 .....	49
4.5. Discussion .....	51
4.5.1. Comparison of the InSAR-Derived Results with the Leveling Data.....	52
4.5.2. Spatial and Temporal Patterns of Land Subsidence .....	54
4.5.3. The Use of Different SAR Sensors in Land Subsidence Monitoring .....	56
4.5.4. Land Subsidence and Possible Causes .....	56
4.6. Conclusion.....	61
<b>5. Earthquake-induced landslide mapping using PALSAR-2 data.....</b>	<b>63</b>
5.1. Introduction .....	63

5.2. Study area.....	64
5.3. Data sets and preprocessing.....	66
5.3.1. SAR and optical satellite data.....	66
5.3.2. Truth data and field survey .....	69
5.4. Methodology .....	70
5.4.1. Synthetic Aperture Radar: Interferometry and coherence .....	70
5.4.2. SAR coherence and intensity difference .....	74
5.4.3. Statistical method .....	74
5.4.4. Decision tree method.....	74
5.6. Results .....	75
5.6.1. Landslide classification using descending and ascending SAR images .....	75
5.6.2. Quantitative analysis of the landslide classification accuracy.....	75
5.7. Conclusion.....	86
<b>6. General conclusions.....</b>	<b>88</b>
<b>References .....</b>	<b>90</b>

## Acknowledgments

First and foremost, I would like to express my deepest appreciation to my advisor, Professor Fumio Yamazaki, and assistant Professor Wen Liu for their continuous help and patient guidance during the three years of Ph.D. study. It might be very difficult for me to finish my thesis without their constant encouragements and adequate guidance. By this opportunity, I also would like to thank the rest of my thesis committee Prof. Josaphat Tetuko Sri Sumantyo, Prof. Shigeo Shioda, and Prof. Yoshihisa Maruyama for their valuable comments and advices.

I would like to thank laboratory secretary Miss Mariko Naruke for her kind help and assistance during my stay in Japan. I also would like to thank all lab members who create a good atmosphere in the Yamazaki laboratory & Maruyama laboratory; former students of Yamazaki laboratory, Luis Angel Moya Huallpa and Homa Zakeri for their friendship and valuable advice for my research.

I would like to acknowledge the European Space Agency (ESA) and Japan Aerospace Exploration Agency (JAXA) for providing satellite SAR data, and Geospatial Information Authority of Japan (GSI) for providing other auxiliary data used in this thesis. I am also grateful for the TOYOTA TSUSHO corporation for their financial support until finish doctoral degree.

Last but not least, I would like to thank my angel mother Patemnisahan Amat for her everlasting love and support through over my life. I also thank my beloved wife Pariza Momin, she always been by my side and took the biggest burden during my Ph.D. study.

ياشلىق ئادەمنىڭ زىلۋا بىر چېغى،  
تولمۇ قىستا ئۇنىڭ ئۆمرى بىراق.  
يىرتىلسا كالىندارنىڭ بىر ۋارىقى،  
ياشلىق گۈلدىن تۆكىلىدۇ بىر يوپۇرماق.

لۇتپۇللا مۇتەللىپ





## Publications

- Aimaiti, Y., Yamazaki, F., & Liu, W. (2018). Multi-sensor InSAR analysis of progressive land subsidence over the Coastal City of Urayasu, Japan. *Remote Sensing*, 10(8), 1304.
- Zhang, R., Liang, T., Guo, J., Xie, H., Feng, Q., & Aimaiti, Y. (2018). Grassland dynamics in response to climate change and human activities in Xinjiang from 2000 to 2014. *Scientific reports*, 8(1), 2888.
- Aimaiti, Y., Yamazaki, F., Liu, W., & Kasimu, A. (2017). Monitoring of land-surface deformation in the karamay oilfield, Xinjiang, China, using SAR interferometry. *Applied Sciences*, 7(8), 772.
- Aimaiti, Y., Yamazaki, F., & Liu, W. (2018). Mapping progressive land subsidence in Urayasu city, Japan, based on multi-temporal DInSAR approach. *International Symposium on Remote Sensing (ISRS)*, 2018.05
- Aimaiti, Y., Liu, W., & Yamazaki, F. (2017). Land surface deformation measurement by SAR interferometry using L band and C band data sets. *International Symposium on Remote Sensing (ISRS)*, 2017.05.

# Chapter 1

## Introduction

### 1.1. Background and objective

In general, the ground surface of the earth deforms either by anthropogenic or naturally induced factors and by their integrated effects. Natural factors such as big earthquakes (Massonnet *et al.*, 1993; Ozawa *et al.*, 2011), slow-moving landslides (Calò *et al.*, 2012), volcanic activities and land subsidence (Ruch *et al.*, 2008; Bayuaji, Sumantyo and Kuze, 2010)etc., are the main contributors of ground surface deformation. Anthropological causes such as mining activities (i.e. extraction of groundwater, oil and gas from underground reservoirs, and the injection of wastewater) would induce deformation in reservoirs by changing the reservoir pressure and consequently generate measurable surface deformations in the form of subsidence or uplift (Khakim, Tsuji and Matsuoka, 2012; Aimaiti *et al.*, 2017). The excessive surface deformation can cause damage to engineering structures and other infrastructure, such as railroads, roads, buildings, and oil and gas pipelines (Guéguen *et al.*, 2009; Grzovic and Ghulam, 2015). Those geohazards may threaten human lives and lead to enormous economic losses. Thus, identifying the signs of impending land deformation is mandatory in correcting the potential problems before associated accidents/incidents occur (Guglielmi *et al.*, 2015).

Ground surface deformations can be detected and monitored by various geodetic techniques, such as global positioning system (GPS)/global navigation satellite system (GNSS), tiltmeter and leveling survey. Although these techniques can provide precise ground deformation measurements at millimeter or centimeter level, due to their spatial density is limited, they cannot acquire dense ground displacement measurements with a large-scale coverage in a short time and at a low cost (Hsieh *et al.*, 2011). Synthetic aperture radar (SAR) interferometry (InSAR) is a proven remote sensing technique that uses the phase differences information of SAR images to measure ground surface deformations. Since the first application of InSAR to detecting the small ground motion of agricultural field (Gabriel, Goldstein and Zebker, 1989), it has been giving increasing attention and widely used because of its large scale coverage and high temporal measurement capability (Pepe and Calò, 2017). Over the years, the new generation and increase of satellite SAR sensors have enabled us to compute surface deformations from the global scale to individual buildings. And the new advanced InSAR techniques have also been proposed to

improve the precision of deformation measurement by the joint analysis of a set of SAR images (Zhang, Ding and Lu, 2015; Osmanoglu *et al.*, 2016). However, it is evident that both leveling and InSAR technique has advantages and disadvantages. How to determine the optimal method should be depending on the characteristic of measured ground deformation and the availability of the data. The combination of both techniques can be an effective way to optimize the accuracy of ground deformation measurement (Zhu *et al.*, 2014).

The research objective of this thesis is to investigate the features and feasibility of C-band and L-band radar images in the extraction of ground deformations at different study areas. The traditional and advanced InSAR methods and GPS observations are also implemented to improve the accuracy of estimated ground deformations. We also present the 2018 Hokkaido Eastern-Iburi Earthquake as a model case of natural disasters. The landslide areas induced by the earthquake are detected using coherence and intensity difference of the pre and post-event ALOS-2 PALSAR-2 images.

## **1.2. Outline of the thesis**

This dissertation is composed of six chapters. The flowchart of the thesis is shown in **Figure 1.1**. The basic organization of this dissertation is as follows:

Chapter 1 introduces the outline of the dissertation, which includes the main topics, background, objectives, and structure of the thesis.

Chapter 2 describes the principle and history of SAR interferometry. In addition, the general information of four primarily used SAR sensors also described.

Chapter 3 presents a case study of ground surface deformation monitoring in Karamay, a typical oil-producing city, in the Xinjiang Uyghur Autonomous Region, China. The Two-pass differential SAR interferometry (D-InSAR), Persistent Scatterer (PS-InSAR) and Small Baseline Subset (SBAS-InSAR) processes were applied to the ALOS PALSAR and ENVISAT ASAR data sets. The influences caused by the different band wavelengths and the methods were compared and discussed. The subsurface water injection was the primary contributor to the ground deformation.

Chapter 4 presents the analysis of progressive land subsidence over the coastal city of Urayasu, Japan. In this chapter, we investigate the long-term land deformation patterns in Urayasu City, three sets of synthetic aperture radar (SAR) data acquired during 1993–2006 from European Remote Sensing satellites (ERS-1/-2 (C-band)), during 2006–2010 from the Phased Array L-band

Synthetic Aperture Radar onboard the Advanced Land Observation Satellite (ALOS PALSAR (L-band)) and from 2014–2017 from the ALOS-2 PALSAR-2 (L-band) were processed by using multitemporal interferometric SAR (InSAR) techniques. Leveling survey data were also used to verify the accuracy of the InSAR-derived results.

Chapter 5 presents our attempt to identify the landslides induced by the 2018 Hokkaido Eastern-Iburi Earthquake. The coherence and intensity calculated from the six pre- and post-event ALOS-2 PALSAR-2 images in descending and ascending orbit were used to extract landslide areas. To improve the accuracy of identified landslides, I have tried six different combination methods. Moreover, the results were verified by comparing with optical satellite images and truth data.

Chapter 6 describes the general conclusion and summary from all the chapters of the dissertation. The discussions and future prospective of the study are also presented.

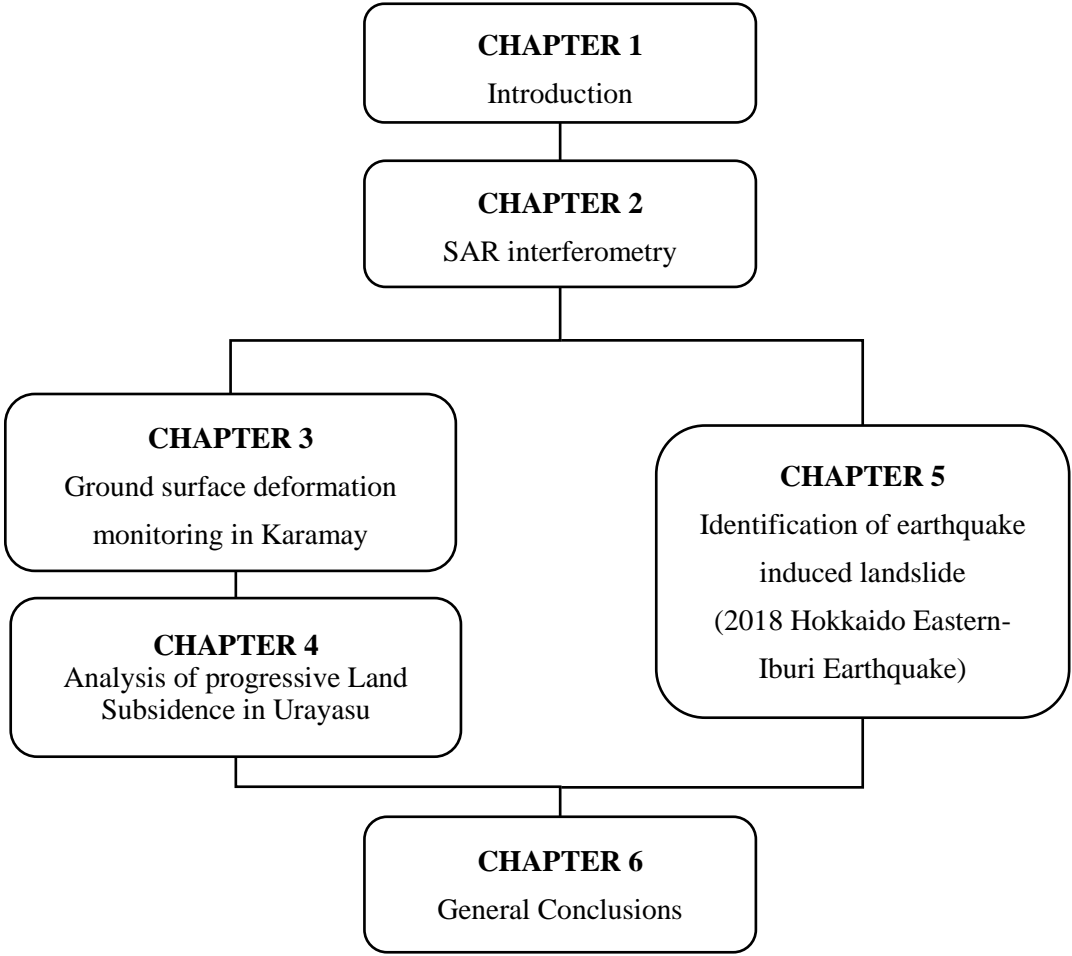


**Figure 1-1** Flowchart of the dissertation

## Chapter 2

### Theoretical concepts of SAR interferometry

#### 2.1. Synthetic Aperture Radar (SAR)

Radio Detection and Ranging (Radar) is a detection system that emits electromagnetic waves from the transmitter (Antenna) and receiving the returned signals from the object to determine the range, angle, and velocity of objects. It was initially developed and used in the military to detect the location and motion of airplanes and sea vessels (Watson, 2009). Although the Radar could detect the object during all weather conditions, it was difficult to achieve high azimuth resolution which needs a very big antenna (impossible to carry by aircraft). To overcome the limitation of Radar, Carl Wiley was first introduced the synthetic aperture radar (SAR) in 1951 and followed the first experiment carried out in 1953 (WILEY and A., 1985). Since then, experiments continued with the airborne SAR, and the first spaceborne SAR-SEASAT was on board in 1978 (Jordan, 1980). As a pioneering mission, it leads a new generation of SAR sensors and has been widely used in various earth observation missions.

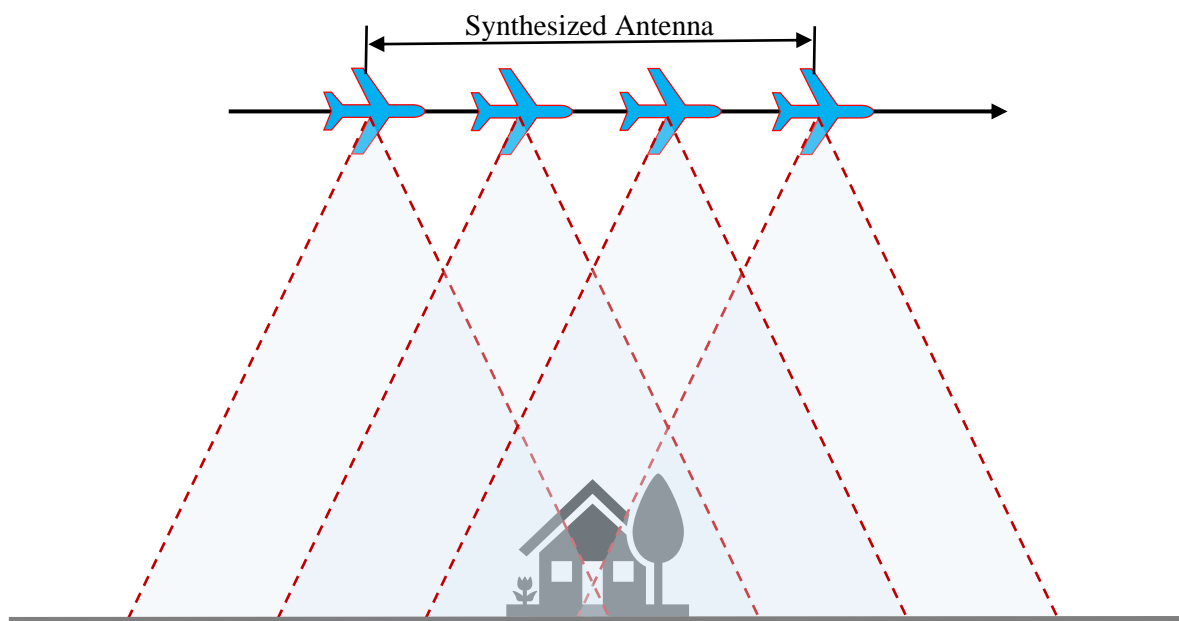


**Figure 2.1** A general scheme of formation of a synthetic antenna array

SAR is an imaging Radar which utilizes the flight path of the platform (space and airborne) to simulate an extremely large antenna to generate high-resolution radar images of the observing objects (**Figure 2.1**). Most of the airborne and spaceborne SAR systems have a fixed side-looking geometry (Moreira *et al.*, 2013), and measuring the distance to objects in slant-range rather than the true horizontal distance of the ground (**Figure 2.2**). Hence, it produces images in varying scale, moving from near to far range. Radar's side-looking geometry can result in several image effects (Slant-range distortion) such as foreshortening, layover, and shadow.

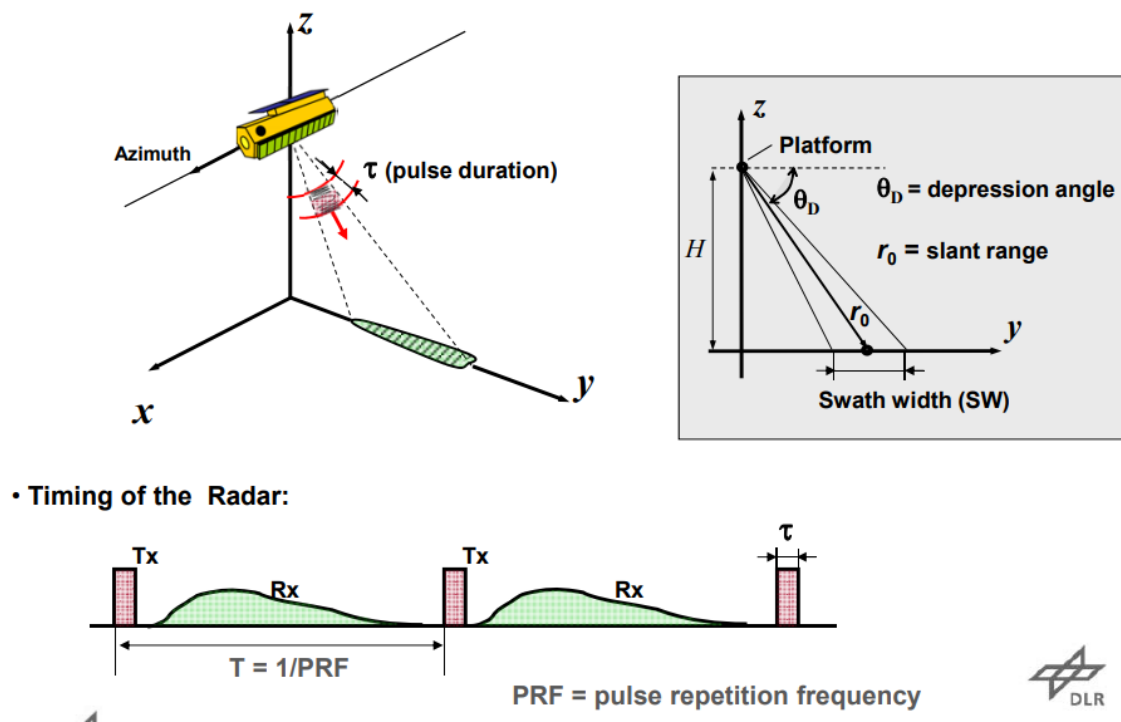


**Figure 2.2** An illustration of side looking Radar imaging geometry and timing (image credit: DLR)

( <https://earth.esa.int/documents/10174/642943/6-LTC2013-SAR-Moreira.pdf>.)

## 2.2. SAR sensors

The SAR sensors are different from the optical sensors, which observes the ground surface through actively sending microwave and receiving its reflections from the object. Because of its ability to measure ground surface differences at any time (independent of weather and daylight conditions), it has become one of the most valuable tools for remote sensing of the earth and its environment. Due to the remarkable improvements in SAR sensors, more than 15 spaceborne

SAR sensors are being operated for various applications (Moreira *et al.*, 2013). And the high-resolution SAR sensors, COSMO-SkyMed (CSM) and TerraSAR-X (TSX) SAR sensors can acquire images with a ground resolution of 1 to 5 m, providing detailed surface information.

In this study, considering the availability of SAR sensors, four sets of SAR images taken by different satellite sensors were used. Since our research is observing the ground surface deformation and its changing trends at a regional level, we used the moderate resolution ERS-1/-2, ENVISAT ASAR, and ALOS PALSAR, a high-resolution mode ALOS-2 PALSAR-2 images. An overview of these sensors and their main characteristics are as follows.

### **2.2.1. ERS-1/-2 and ENVISAT ASAR**

The European Space Agency developed the European Remote Sensing satellites ERS-1 and ERS-2 as a family of multi-disciplinary Earth Observation Satellites. The ERS-1 was launched on 17 July 1991 into a sun-synchronous polar orbit at an altitude of 782-785 km, with an overall weight of 2384 kg (at launch) and an overall height of 11.8 m. It carried an array of earth-observation instruments (i.e., RA (Radar Altimeter-Ku band), ATSR-1 (Along-Track Scanning Radiometer), SAR-C band, Wind Scatterometer, and MWR is a Microwave Radiometer) could gather information about the land, water, ice, and atmosphere. ERS-1 has 3 and 35-day repeat cycles and a resolution of around 20 m and 100 km coverage (**Figure 2.3**). ERS-1 has ended its mission on 10 March 2000, after a nearly two-decade (1991-2000).

As a successor to ERS-1, ERS-2 was launched on 21 April 1995. It carried one new instrument, the Global Ozone Monitoring Experiment (GOME). It has a total weight of 2,516 kg, with a repeat cycle of three or 35 days, and shares the same orbit with ERS-1 and passes the same point on the ground one day later than ERS-1 (**Figure 2.4**). After spent 16 years in orbit, ERS-2 has ended its mission on Sept. 5, 2011 (1995-2011).

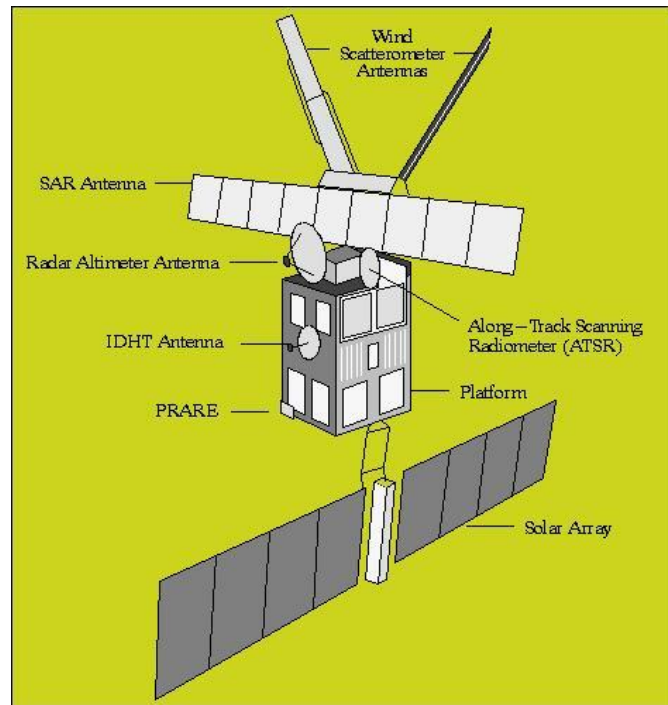
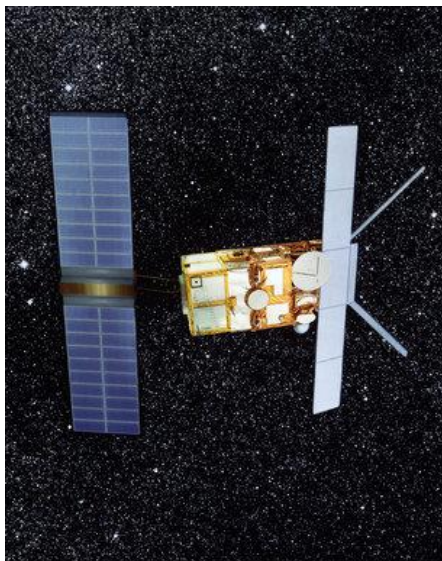


**Figure 2.3** A view of the ERS-1 spacecraft in orbit (left) and Illustration of the deployed ERS-1 spacecraft (right) (image credit: ESA)

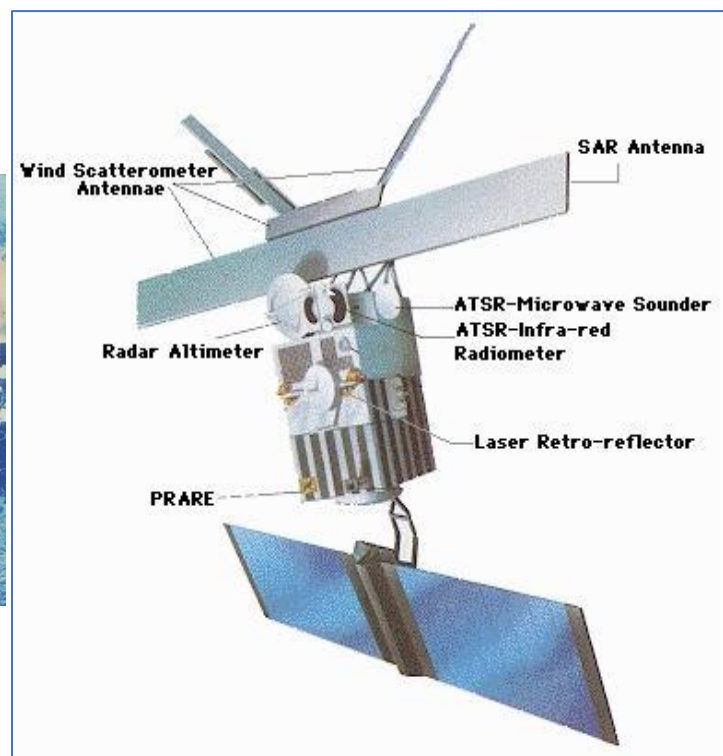


**Figure 2.4** A view of the ERS-2 spacecraft (left) and Illustration of the deployed ERS-2 spacecraft (right) (image credit: ESA)



The Environmental satellite (Envisat) is a successor to ERS and was launched by the European Space Agency on 1 March 2002 with 10 instruments. Envisat has a total weight of eight tons, with a repeat cycle of 35 days. The Advanced Synthetic Aperture Radar (ASAR) operated in the C band in image mode was used in this thesis. Envisat has ended its mission on 08 April 2012.

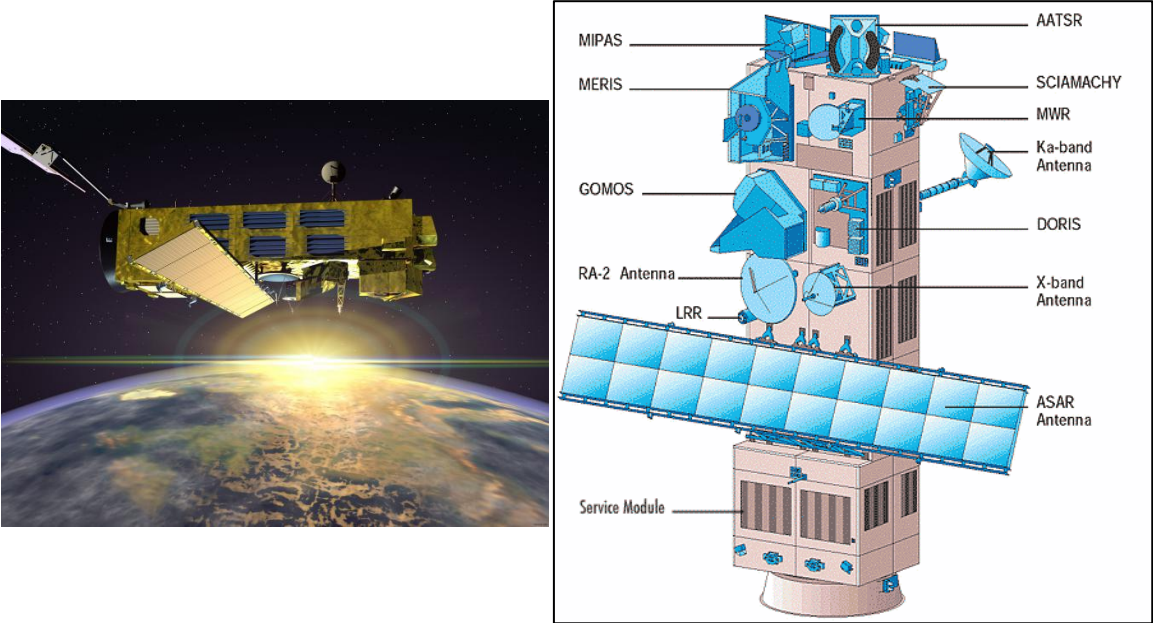


**Figure 2.5** A view of the Envisat spacecraft (left) and Illustration of the Envisat spacecraft (right) (image credit: ESA)

**2.2.2. ALOS PALSAR and ALOS-2 PALSAR-2**

Phased Array L-band Synthetic Aperture Radar (PALSAR) is one of the sensors on board the Advanced Land Observing Satellite “DAICHI” (ALOS), which is shown in **Figure. 2.6**. ALOS was launched on January 24, 2006 and operated by Japan Aerospace Exploration Agency (JAXA). When the Tohoku earthquake hit Japan in March 2011, the ALOS took more than 400 images over disaster-stricken areas to provide disaster information. However, a power generation anomaly caused a communication loss on April 22, 2011, and thus JAXA completed its operation on May 12, 2011. The observation of PALSAR sensor was carried out by the L-band with the 23.6 mm wavelength and had three main modes: High resolution, ScanSAR, and Polarimetric mode. The High-resolution mode includes two types: single (FBS) and dual polarization (FBD). In this study, the SAR images taken by the FBS and FBD mode are mainly used to mapping the ground deformation. The detailed information of the PALSAR sensor and detail information for each mode is shown in **Table 2.1**.

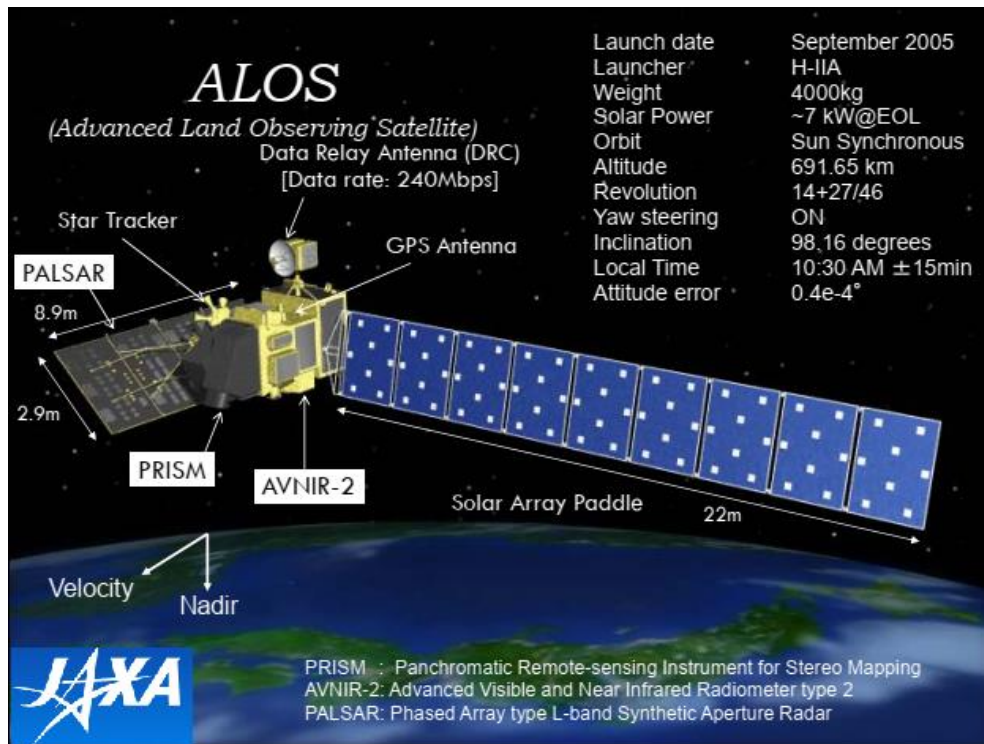


**Figure 2.6** The overall view and Illustration of the ALOS satellite (image credit: JAXA)

**Table 2.1** Parameters for each observing mode (adapted from the website of PASCO Co.)

Mode	High resolution		ScanSAR	Polarimetric (Experimental*1)
	Bandwidth	28 MHz	14 MHz	14 MHz, 28 MHz
Polarization	HH or VV	HH+HV or VV+VH	HH or VV	HH+HV+VH+VV
Range of incidence angles	8 - 60°	8 - 60°	18 - 43°	8 - 30°
Ground resolution	7 - 44 m	14 - 88 m	100m (multi look)	24 - 89 m
Swath	40 - 70 km	40 - 70 km	250 - 350 km	20 - 65 km

(Source: <http://en.alos-pasco.com/alos/palsar/>.)

The ALOS-2 is the successor of the ALOS launched on May 24, 2014, yet the structure is quite different from ALOS. The ALOS equipped with three sensors, AVNIR-2, PRISM, and PALSAR, and the new satellite is specialized for SAR. As a new generation, the capacity of the PALSAR-2 sensor has significantly improved from the PALSAR in all aspects, such as resolution, observation band, and repeat cycle. PALSAR-2 have a spotlight mode (1m×3m (in azimuth and range direction)), while PALSAR has

a maximum of 10-meter resolution (**Figure 2.7**). The revisit time was also reduced from 46 days to 14 days. Therefore, it will allow comprehensive monitoring of disasters around the world with more detailed information.

**Table 2.2** Characteristics and specifications of PALSAR-2

Observation mode	Spotlight	Stripmap					ScanSAR			
		Ultrafine [3m]	High sensitive [6m]		Fine [10m]		Normal		Wide	
Bandwidth (MHz)	84	84	42		28		14	28	14	
Resolution(m)	3×1 (Rg×Az)	3	6		10		100 (3 looks)		60	
Incidence angle (deg.)	8 - 70	8 - 70	8 - 70	20 - 40	8 - 70	23.7	8 - 70		8 - 70	
Swath (km)	25×25 (Rg×Az)	50	50	40	70	30	350 (5 scans)		490 (7 scans)	
Polarization*	SP	SP/DP	SP/DP/CP	FP	SP/DP/CP	FP	SP/DP		SP/DP	
NESZ (dB)	-24	-24	-28	-25	-26	-23	-26	-23	-26	
S/A (dB)	Rg	25	25	23	23	25	20	25	25	20
	Az	20	25	20	20	23		20		20

\* SP: HH or HV or VV, DP: HH+HV or VV+VH, FP: HH+HV+VH+VV, CP: compact pol. (Source: JAXA)



**Figure 2.7** A view of the ALOS-2 PALSAR-2 satellite in orbit. (Image source: JAXA)

### 2.3. InSAR

Interferometric Synthetic Aperture Radar (InSAR) is a proven remote sensing technique that uses the phase information of two or more SAR images over the same region to measure ground surface movements. **Figure 2.8** shows the basic geometrical configuration of InSAR, both master and slave acquisitions illuminate the same ground on the earth.  $B$  is the distance between two antennas, called baseline,  $\theta$  is the look angle, and the slant ranges from Master and Slave to the target points are  $R_1$  and  $R_2$ , respectively and  $\alpha$  is the angle between the baseline and the horizontal. The major component causing the interferogram can be resolved as  $\phi_{topo}$  (topographic change in the terrain),  $\phi_{defo}$  (Surface deformation caused by natural processes or human activities) and  $\phi_{atmo}$  (temporal and spatial differences in atmospheric delays). In addition to these, there are some other noise factors that are due to various error and unknown factors. All these contributions are superimposed, resulting in the observed total interferometric phase:

$$\phi = \phi_{topo} + \phi_{defo} + \phi_{atmo} + \phi_{scat} + \phi_{orb} + \phi_{noise} + 2\pi\alpha \quad (2.1)$$

With phase  $\phi_{scat}$  is the phase due to changes in scattering characteristics of the reflected surface, phase  $\phi_{orb}$  is the phase shift due to the error in orbit determination and phase  $\phi_{noise}$  is the remaining

phase delay due to the thermal noise of the instrument. The last term represents the unknown integer number of phase cycles.

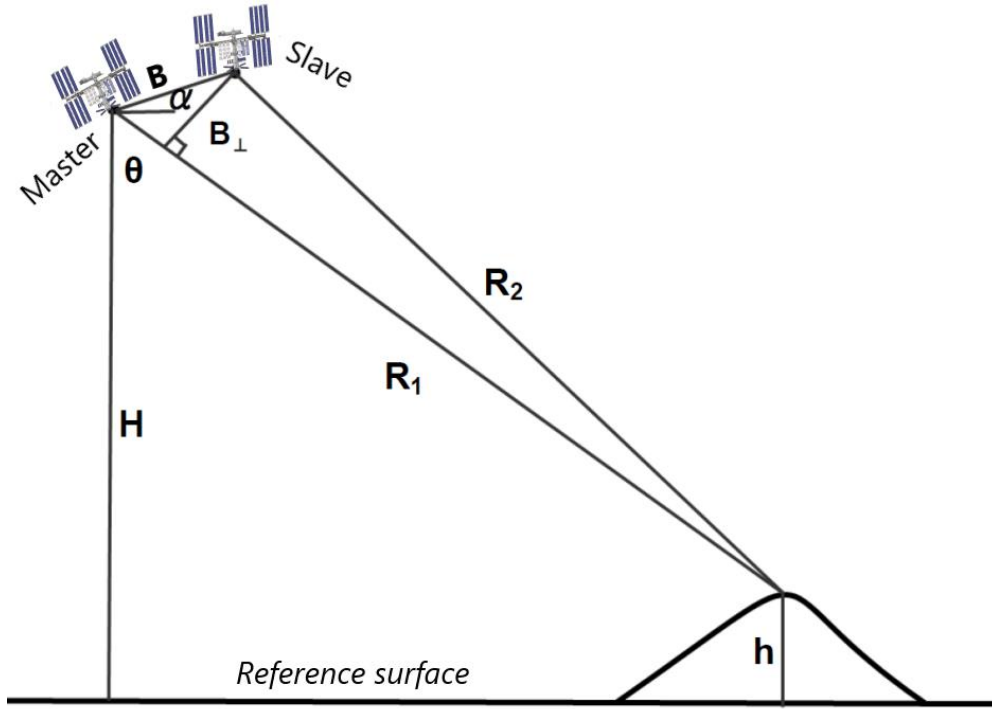


**Figure 2.8** The geometry of InSAR

In the above expression  $\phi_{topo}$  can be expressed as follows:

$$\phi_{topo} = -\frac{4\pi}{\lambda} \frac{B_{\perp}}{R \sin \theta} h \quad (2.2)$$

with  $B_{\perp}$  the perpendicular baseline,  $\lambda$  the wavelength,  $R$  the slant range,  $\theta$  the look angle and  $h$  the height above the reference spheroid or ellipsoid.

If the slant range difference is given by  $\Delta R = R_2 - R_1$ , then the measured interferometric phase is

$$\phi = -\frac{4\pi}{\lambda} \Delta R \quad (2.3)$$

This is  $2\pi$  times the round-trip distance difference in wavelengths. By applying the law of cosines in  $\Delta S_1 P S_2$ ,  $\Delta R$  can be solved as

$$\Delta R = \sqrt{R_1^2 + B^2 - 2R_1 B \sin(\theta_1 - \beta)} - R_1 \quad (2.4)$$

There are two InSAR techniques to remove topographic phase from the interferogram: one is the DEM method (Massonnet *et al.*, 1993) and the other is the three-pass method (Zebker *et al.*, 1994). The first method is also called two path InSAR method (DInSAR), which uses an existing DEM and calculate the topographic phase from the DEM and subtracted from the interferogram. The second method uses three SAR image pairs and one interferogram as a reference, which is believed to contain the topographic phase only. This approach has the advantage in that all data structure is kept within the SAR data geometry while the DEM method can produce errors by misregistration between SAR data and cartographic DEM. However, the three-pass approach is restricted by data availability. In **Figure 2.9**, we show an example DInSAR interferometry computed over Urayasu city, Chiba Prefecture, Japan, using two SAR images acquired using ALOS-PALSAR 2 satellite on December 4, 2014, and September 07, 2017.

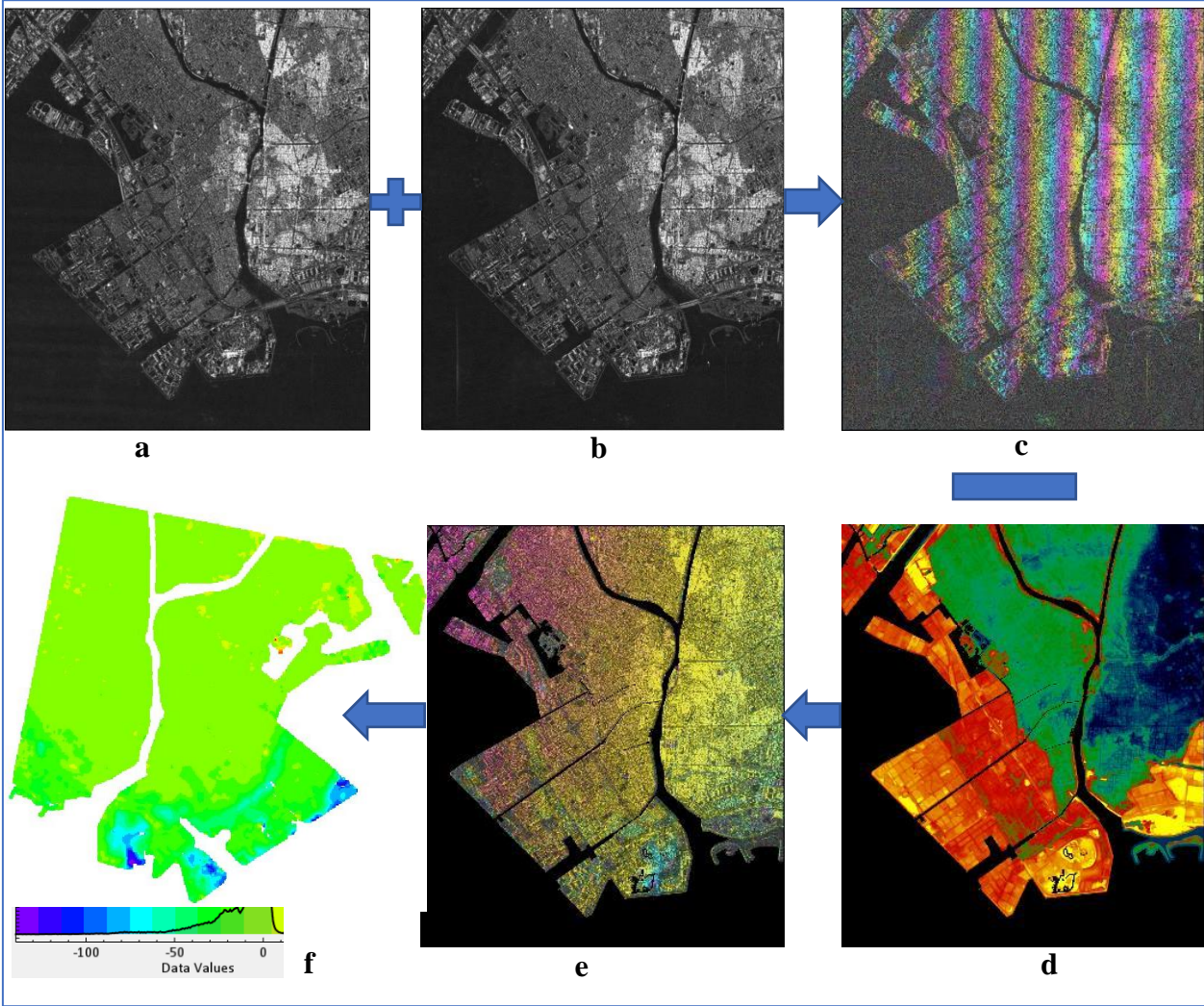


**Figure 2.9** An example interferogram computed over Urayasu city, Japan using the two-path DInSAR method. (note: a and b represent the master and slave image, respectively; c represents

the calculated first interferogram;  $d$  is the reference DEM (5m) in slant range;  $e$  represents the flattened and filtered interferogram;  $f$  represents the final geocoded product).

## 2.4. Multi-temporal InSAR-stacking technique

As the conventional InSAR method is limited by the so-called temporal and geometrical decorrelation as well as by atmospheric artifacts (Prati, Ferretti and Perissin, 2010). One of the big effects is an atmospheric delay, and it has significant characters that it is correlated spatially and uncorrelated temporally. These features inspired the development of multi-temporal InSAR analysis techniques. Over the years, new advanced InSAR techniques have been proposed to improve the precision of deformation measurement by the joint analysis of a set of SAR images.

The advanced multi-temporal InSAR techniques are mainly classified into two categories, Permanent Scatterer InSAR (PSI) and Small Baseline Subset (SBAS). The PSI focuses on the use of time series SAR images to detect coherent radar signals (pointwise and stable scatterers) over a sequence of interferograms (Ferretti, Prati and Rocca, 2000, 2001; Hooper and Zebker, 2007). The introduce of PSI was a breakthrough that increased the estimation of terrain velocity up to millimeter level. SBAS-use of all available SAR images with small baselines and a time interval to achieve a high degree of the spatial coverage of distributed scatters (Berardino *et al.*, 2002). PSI and SBAS can mitigate the random atmospheric noise with a statistical approach. Nowadays, the number of satellite data sources is increasing steadily, and several algorithms have been developed (e.g., Intermittent SBAS (ISBAS) (Sowter *et al.*, 2013), SqueeSAR (Ferretti *et al.*, 2011), Stanford Method for Persistent Scatterers (StaMPS) (Hooper, 2008), Stable Points Network (SPN) (Crosetto *et al.*, 2008), Quasi Persistent Scatterers (QPS) (Perissin and Wang, 2012), Persistent Scatterer Pairs (PSP) (Costantini *et al.*, 2008), Interferometric Point Target Analysis (IPTA) (Werner *et al.*, 2004), Coherent Pixels Technique (CPT) (Blanco-Sánchez *et al.*, 2008), Temporarily Coherent Point InSAR (TCPInSAR) (Zhang, Ding and Lu, 2011) and Delft Persistent Scatterer Interferometry (DePSI) (Kampes, 2005) etc.). Therefore, the advanced multi-temporal InSAR methods are becoming a standard for ground surface monitoring instead of conventional InSAR.

## Chapter 3

# Monitoring of Land-Surface Deformation in the Karamay Oilfield, Xinjiang, China Using SAR Interferometry

### 3.1. Introduction

Interferometric Synthetic Aperture Radar (InSAR) is a proven remote sensing technique that uses the phase information of SAR images to measure ground surface movements. However, the conventional InSAR method is limited by the so-called temporal and geometrical decorrelation as well as by atmospheric artifacts (Prati, Ferretti and Perissin, 2010). Over the years, new advanced InSAR techniques have been proposed to improve the precision of deformation measurement by the joint analysis of a set of SAR images (Zhang, Ding and Lu, 2015; Osmanoglu *et al.*, 2016), for example, Permanent Scatterer InSAR (PS-InSAR<sup>TM</sup>)—use of time series SAR images to detect coherent radar signals over a sequence of interferograms (Ferretti, Prati and Rocca, 2000, 2001); Small Baseline Subset (SBAS)—use of all available SAR images with small baselines to achieve a high degree of spatial coverage of distributed scatters (Berardino *et al.*, 2002); Persistent Scatterer Pairs (PSP)—works with pairs of points to identify and analyze persistent scatterer (Costantini *et al.*, 2008); Quasi Persistent Scatterers (QPS)—utilizes partially coherent targets to increase the spatial density of the observations (Perissin and Wang, 2012); Stable Points Network (SPN), which has three key features (i.e., pixel selection, use of multi-master images and modeling capability) and less sensitive to geometric decorrelation (Crosetto *et al.*, 2008); SqueeSAR<sup>TM</sup>—a second generation of PS-InSAR<sup>TM</sup> which combines both the persistent and distributed scatterers (Ferretti *et al.*, 2011); Stanford Method for Persistent Scatterers (StaMPS)—similar to PS-InSAR, but the PS points are defined as the scatters with stable phase characters (Hooper, 2008); Temporarily Coherent Point InSAR (TCPInSAR)—detecting the ground deformation rate and solving the phase ambiguities without phase unwrapping (Zhang, Ding and Lu, 2011); and Intermittent SBAS (ISBAS)—an extension of SBAS-InSAR that use the pixels which are intermittently coherent in addition to those consistently stable over time (Sowter *et al.*, 2013), etc. These methods have been widely used to measure human- and naturally induced ground deformation, such as earthquake deformation (Liu *et al.*, 2015; Ganas *et al.*, 2016), mining



subsidence (Samsonov, d'Oreye and Smets, 2013; Li *et al.*, 2016), volcano deformation (Chaussard, Amelung and Aoki, 2013; Jo, Jung and Won, 2017), landslides (Calò *et al.*, 2014; Schulz *et al.*, 2017) and glacier movement (Satyabala, 2016; Sánchez-Gámez *et al.*, 2017). Additionally, several studies pertaining to gas/oil extraction-induced and CO<sub>2</sub>/water injection-induced surface deformation have been carried out (Tamburini *et al.*, 2010; Heimlich *et al.*, 2015; Yang *et al.*, 2015; Shirzaei *et al.*, 2016; Sun *et al.*, 2017).

In particular, the extraction of ground water, oil and gas from underground reservoirs, and the injection of waste-water would induce deformation in reservoirs by changing the reservoir pressure and consequently generate measurable surface deformations in the form of subsidence or uplift (Khakim, Tsuji and Matsuoka, 2012). The excessive surface deformation can cause damage to engineering structures and other infrastructure, such as railroads, roads, buildings, and oil and gas pipelines (Guéguen *et al.*, 2009; Grzovic and Ghulam, 2015). Thus, identifying the signs of impending land deformation is important in correcting the potential problems before associated accidents/incidents occur (Guglielmi *et al.*, 2015).

As one of the largest oilfields in China, the Karamay oilfield has large amount of heavy and ultra-heavy oil deposits (Xu, 2013). After several years of oil field development, a subsurface water injection project was initiated in 1985 to increase the oil production (Li, X.; Li, W.; Gao, B.; Yang, 2012). Despite the Karamay oilfield being in production since 1897 (Pang, 2001), due to the lack of ground measurement data, few studies have been conducted related to the land deformation in this area. Ji *et al.* (Ji *et al.*, 2016) first applied the InSAR technique with Advanced Land Observing Satellite (ALOS) Phased Array L-band Synthetic Aperture Radar (PALSAR) images acquired between October 2006 and December 2010 for investigating land-surface displacement in the Karamay oil field, and they detected a significant land uplift area located around the Hei103 well region and concluded that the land uplift may have been caused by subsurface water injection. However, the agreement of the results obtained by different microwave bands of SAR has not yet been achieved. To further understand land-surface deformation in the Karamay oilfield, this paper will make use of three InSAR methods. First, the two-path differential SAR interferometry (D-InSAR) method was applied to three L-band SAR images acquired by ALOS-PALSAR over the study area in the period from 20 January 2007 to 25 January 2009; Second, we further applied the Persistent Scatterer (PS) and Small baseline subset (SBAS)-InSAR technique to 21 C-band images acquired by the Environmental Satellite (ENVISAT) C-band Advanced Synthetic Aperture Radar (ASAR) for the period 30 September

2003 to 15 June 2010. Moreover, comparisons of different InSAR methods and the comparison of satellite-derived deformation rates with the results of a previous continuous Global Positioning System (GPS) station was conducted. This research is intended to assist with identifying areas experiencing ground deformations, in turn helping local authorities concentrate on the detailed monitoring, investigation and risk mitigation over large areas at relatively low costs.

## **3.2. Study Area and Data Sets**

### **3.2.1. Study area**

Karamay is a prefecture-level city in the northern part of the Xinjiang Uyghur Autonomous Region, the People's Republic of China. Karamay covers an area of 9500 km<sup>2</sup> and consists of four administrative districts, Urho, Baijiantan, Karamay and Dushanzi (**Figure 3.1**). Oil and natural gas are the main natural resources in Karamay with characteristics of large storage and higher quality. The region is in the mid-latitudes and has a typical temperate continental desert climate. The geomorphological type is predominantly Gobi Desert (Pan *et al.*, 2012) with an altitude of 250 m to 500 m. Of interest, the relatively minor change in elevation assists with achieving a more accurate result in the SAR interferometry by minimizing the Digital Elevation Model (DEM) error.

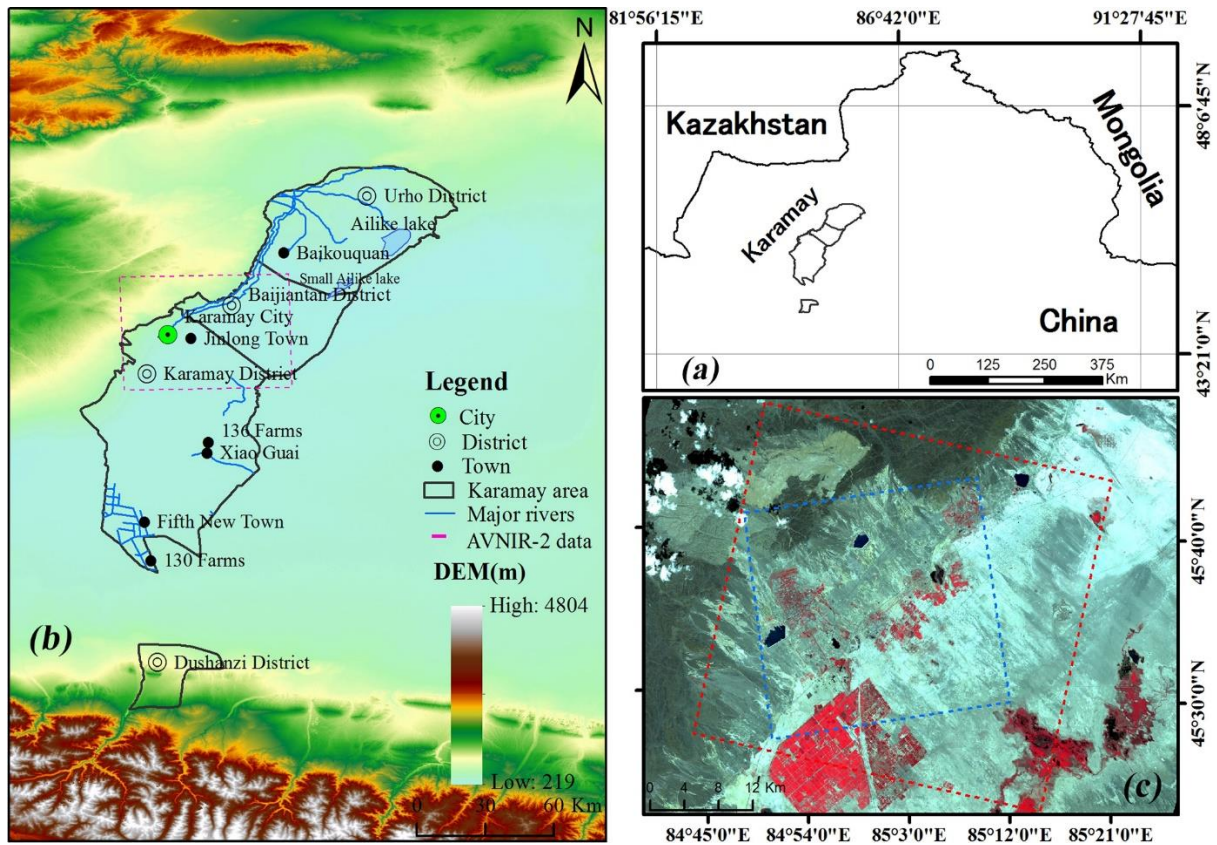


**Figure 3.1.** (a) Geographic location of the study area; (b) Administrative districts of the study area superimposed on the topographic map; (c) ALOS-Advanced Visible and Near Infrared Radiometer type 2 (AVNIR-2) false color composite image of the study area on 15 July 2008. The red and blue dashed lines represent the coverage of ENVISAT-ASAR and ALOS-PALSAR data sets. ALOS: Advanced Land Observing Satellite; ENVISAT: Environmental Satellite; ASAR: Advanced Synthetic Aperture Radar; PALSAR: Phased Array L-band Synthetic Aperture Radar.

### 3.2.2. Data Sets

The L-band ALOS satellite data sets covering the region of interest were provided by the Japan Aerospace Exploration Agency (JAXA). The SAR interferograms were computed from PALSAR fine-beam single-polarization (FBS) data taken on three different dates (20 January 2007, 10 December 2008, and 25 January 2009), and predominantly over the winter season to minimize the adverse impact that vegetation has on the accuracy of SAR interferometry. Observation parameters for all the images were as follows: reference system for planning (RSP) number 94; path number 501; and acquired in the ascending orbit with an off-nadir angle of  $34.3^\circ$ . We also used twenty-one C-band ENVISAT-ASAR images provided by the European Space Agency (ESA) and acquired in the period from 30 September 2003 to 15 June 2010. These data

sets were acquired in the descending orbit with an incidence angle of  $22.9^\circ$ . A Shuttle Radar Topography Mission-3 (SRTM-3) version-4 (90 m resolution) was used to eliminate the topographic phase, which was downloaded from (<http://www.cgiar-csi.org/>). **Figure 3.1** shows the cover ranges of the ALOS and ENVISAT data.

### **3.3. Methodology**

#### **3.3.1. D-InSAR**

D-InSAR is a technique capable of detecting land-surface deformation by analyzing a single interferogram that is derived from a pair of SAR images with the addition of a DEM (Rosen *et al.*, 2000). In this study, the two-pass interferometry method was implemented by using two ALOS-PALSAR Single Look Complex (SLC) images for interferogram generation, and then, the topographic phase was removed using the SRTM DEM data. To remove noise and to smooth the interferogram, the Goldstein–Werner filtering process was applied (Goldstein and Werner, 1998), and the coefficient in the filtering process was set to 0.2. Finally, the InSAR products were geocoded from the Range-Doppler coordinates to the map geometry with a pixel resolution of 25 m. The SARscape® Modules (5.1) for ENVI (5.3) software suit was employed to process the level-1.1 data and perform interferometric analyses.

#### **3.3.2. PS and SBAS-InSAR**

PS-InSAR is one of the promising approaches that improves the precision of conventional InSAR displacement measurements. The PS-InSAR algorithm utilizes a time series of radar images to detect coherent radar signals from PS points to derive information of the terrain motion (Ferretti, Prati and Rocca, 2000, 2001; Hooper *et al.*, 2004). Another algorithm called SBAS-InSAR was also employed, which utilizes all available SAR images with small baselines to get high degree of spatial coverage of distributed scatters (Berardino *et al.*, 2002). Both algorithms can compensate the disadvantages of the conventional D-InSAR, namely, phase errors due to geometrical and temporal decorrelation as well as atmospheric disturbance (Grzovic and Ghulam, 2015).

The ENVISAT-ASAR data were processed using both the PS and SBAS-InSAR methods. For PS-InSAR, we selected the slant-range image (28 November 2006) as a master image and generated 20 interferograms. The perpendicular baseline ranged from 43 m to 951 m, the temporal baseline ranged from 68 days to 1277 days, and selected the potential PS candidates with a

coherence threshold of 0.67. For SBAS-InSAR, we selected the slant-range image (28 October 2008) as a super master image. To reduce the geometrical and temporal decorrelation, the threshold criteria with a maximum temporal baseline of 735 days and a maximum perpendicular baseline of 483 m were used, and then, 68 interferograms were generated. **Figure 3.2** shows the time-baseline plot for the ENVISAT-ASAR images used for PS and SBAS-InSAR processing. A combination of the minimum cost flow (MCF) network (Costantini, 1998) and Delauney 3D method (Hooper and Zebker, 2007) was employed for phase unwrapping with an unwrapping coherence threshold of 0.35. After that, a screening process of flattened, filtered interferograms and unwrapped phases for checking some unwanted behaviors and data problems, which were caused by strong orbit inaccuracy, non-coherent pairs, atmospheric artefacts, residual topography etc., and 12 interferometric pairs were discarded from further processing. For refinement and reflattening, the reference points where the unwrapped phase value close to zero and flat areas identified from a topographic map projected in the line of sight (LOS) direction were chosen (Ahmad Abir *et al.*, 2015). A custom atmospheric filtering was performed with a low-pass spatial filter with a  $1.2 \text{ km} \times 1.2 \text{ km}$  window on each single acquisition, and a high-pass filter at 365 days on these preliminary results to recover the final and cleaned displacement time series. Finally, geocoding was done in the original satellite LOS direction with a pixel resolution of 25 m. The same software package used for D-InSAR was also used in the PS and SBAS-InSAR processing chain.

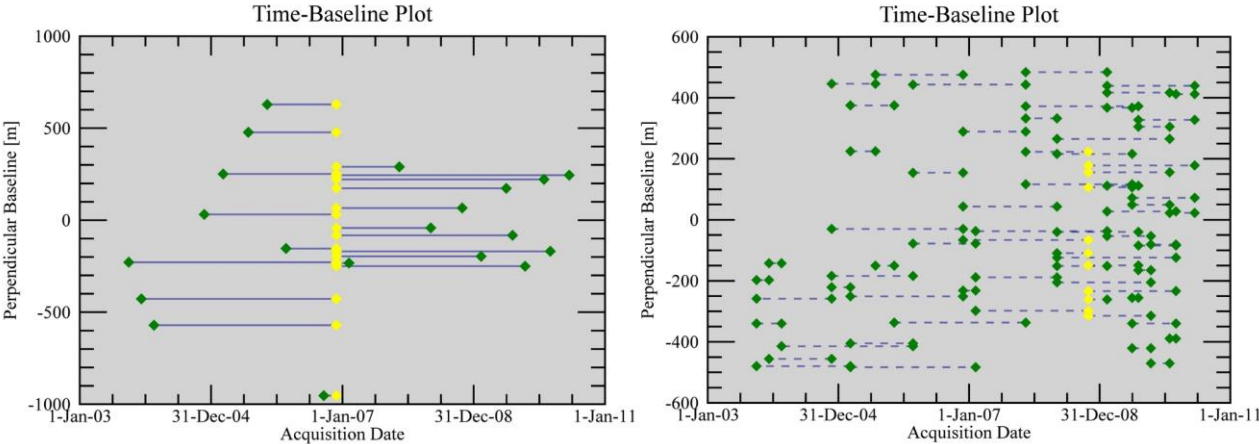


**Figure 3.2.** Perpendicular baseline variations for both PS and SBAS-InSAR interferograms. Green diamonds represent selected interferogram pairs, and the yellow diamonds represent the selected master image of PS (left side: 28 November 2006) and SBAS (right side: 28 October 2008). PS: Persistent Scatterer; SBAS-InSAR: Small Baseline Subset-Interferometric Synthetic Aperture Radar.

### 3.3.3. Pearson Correlation Coefficient and Root Mean Square Error

The deformation rate derived from different methods with respect to each pixel in major deformation areas were compared using the Pearson correlation coefficient ( $r$ ) and the root mean square error (RMSE). During the estimation, we only considered the common valid pixels taken from the deformation map of three InSAR methods. The Pearson's  $r$  is often measured as a correlation coefficient with 0 indicating no linear relationship between the variables, +1 indicating a perfect increasing linear relationship and vice versa (Lawrence, I., 1989).

$$r = \frac{\sum_{i=1}^n (x_i - \bar{x}) \cdot (y_i - \bar{y})}{\sqrt{\sum_{i=1}^n (x_i - \bar{x})^2 \cdot \sum_{i=1}^n (y_i - \bar{y})^2}} \quad (1)$$

where  $n$  is the total number of common valid pixels of the selected reference points,  $x$  and  $y$  ( $\bar{x}$  and  $\bar{y}$  mean values) are the values of the pixels taken from the selected reference points.

The RMSE values can be used to compare the individual model performance to that of other predictive models; it is often used in the field of geosciences, where researchers use the RMSE for model errors and comparison (McKeen *et al.*, 2005; Chatterjee *et al.*, 2013; Du *et al.*, 2016).

$$RMSE = \sqrt{\frac{\sum_{i=1}^n (X_{m,i} - X_{s,i})^2}{n}} \quad (2)$$

where  $n$  is the total number of common valid pixels of the selected reference points,  $X_{m,i}$  and  $X_{s,i}$  are the deformation rate values of the reference points taken from the deformation map of two InSAR methods, respectively.

## 3.4. Results and Analysis

### 3.4.1. Results of D-InSAR Interferometry

The coherence is an indicator of InSAR data quality and significantly influences the accuracy of the phase in interferograms (Zou *et al.*, 2009). As shown in **Figure 3.3**, the mean coherence is lower (0.39) for the data pairs with long time intervals and relatively large perpendicular baselines (20 January 2007 and 10 December 2008,  $B_p = 643$  m). Meanwhile, the mean coherence is higher (0.65) for the data pairs with short time intervals and relatively small perpendicular baselines (10

December 2008 and 25 January 2009,  $B_p = 472$  m). Good quality interferograms were generated from these two data pairs (Figure 3.4); the interferogram with a relatively small perpendicular baseline shows good coherence (Figure 3.3b), but no significant land deformation was found (Figure 3.4b). It is due to the short interval of time, which was 46 days. Therefore, we used the differential interferogram generated from the large perpendicular baseline pair, which showed clear deformation at two sites in the study area. These areas are indicated by blue dashed circles in Figure 3.4a. Although the small time baseline image pair was not used for final displacement map generation, it served as a good example of showing the difference of different perpendicular baseline image pairs, and, provided useful clues for further data selection and analyzes.

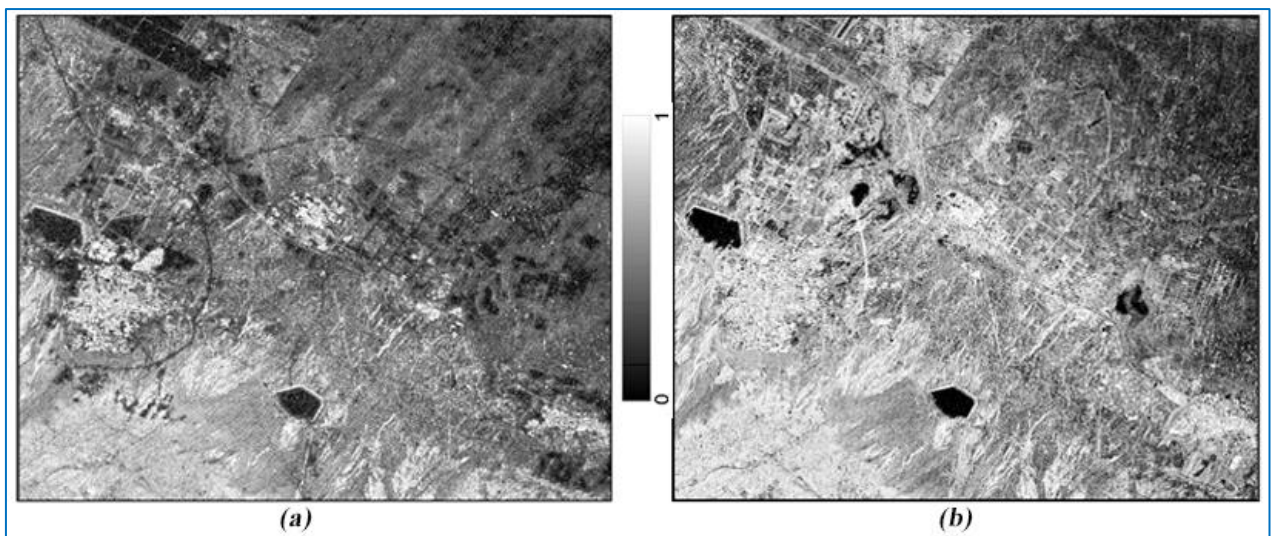


**Figure 3.3.** Coherence images of the interferograms generated from the data pair (a) (20 January 2007 and 10 December 2008,  $B_p = 643$  m) and (b) (10 December 2008 and 25 January 2009,  $B_p = 472$  m).

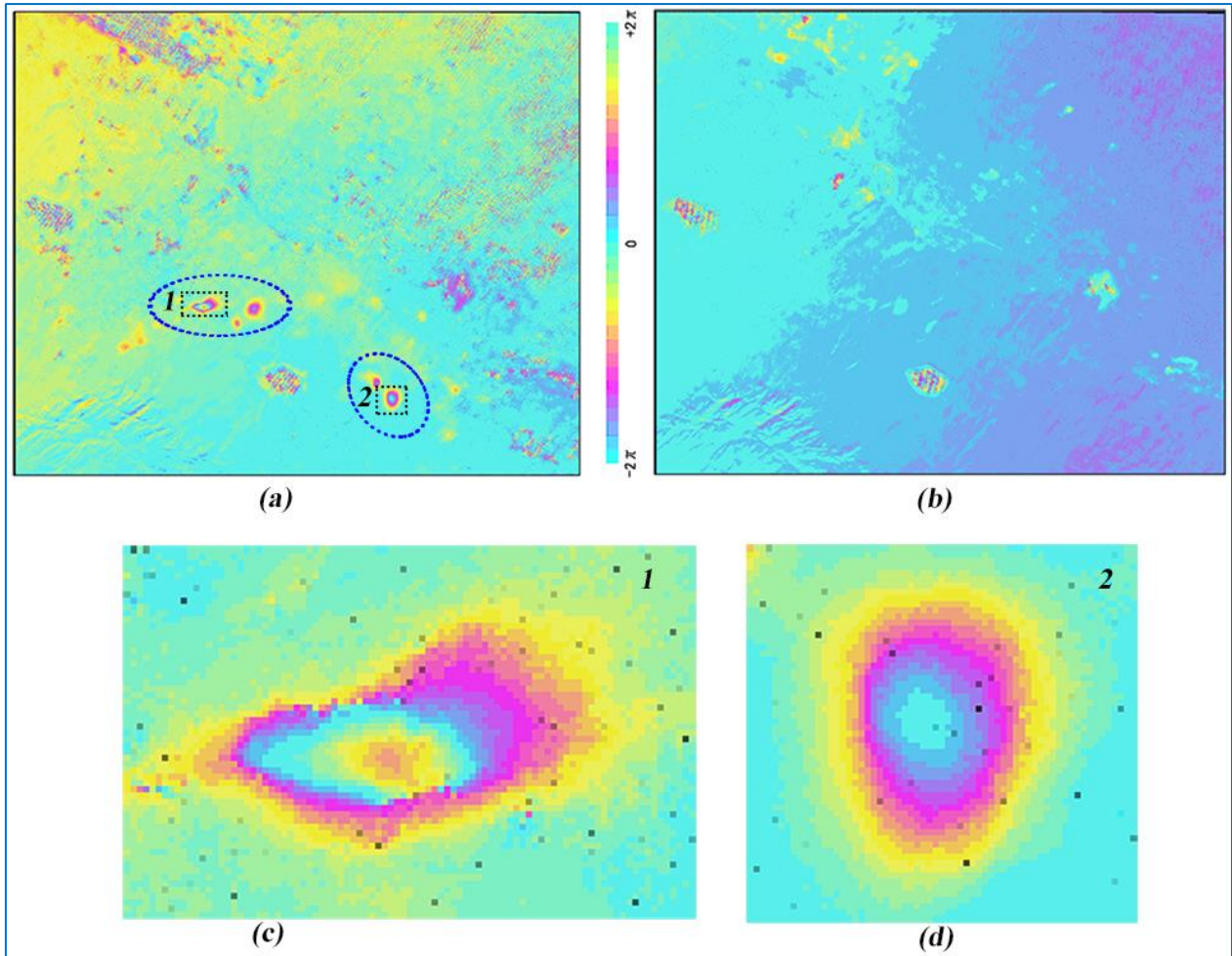


**Figure 3.4.** Differential interferograms generated from the data pair (a) (20 January 2007 and 10 December 2008,  $B_p = 643$  m) and (b) (10 December 2008 and 25 January 2009,  $B_p = 472$  m) after the removal of topographic phase and noise filtering; (c,d) are the close-up view of a typical fringe maps, where the locations are indicated by the black dashed lines in (a).

In general, the sequence of color fringes in the interferogram can be used to determine whether uplift or subsidence has taken place. We chose two close-up views of typical fringe maps (**Figures 4c, d**) from these two deformation sites for further analysis. The ALOS-PALSAR data were in the ascending orbit in which observations were made from the west. The sequence of color fringes in these two figures shows a decrease in range (yellow–purple–blue), which denotes that the ground objective moves closer to the satellite. In this study, we did not consider the horizontal movement, and thus, it corresponded to an uplift. During the process of extracting the ground displacement, we unwrapped the interferogram in order to solve the  $2\pi$  ambiguity, and corrected the satellite orbit inaccuracy and phase offset using the collected external ground control points (GCPs). The final geocoded ground displacement map in the LOS direction is shown in **Figure**



3.5. The figure shows that two sites in the north-eastern part of the city exhibit clear indications of land uplift, and the maximum LOS displacement was approximately 13 cm in the study period.

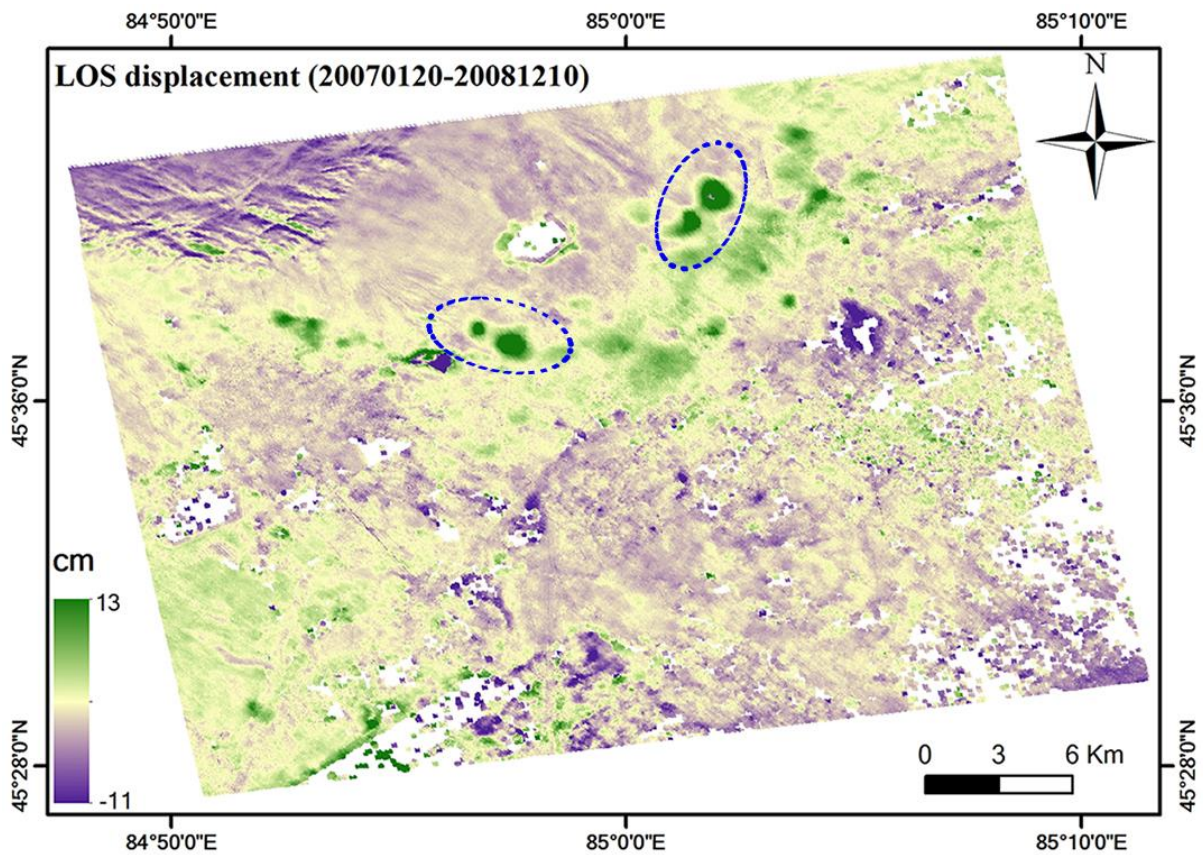


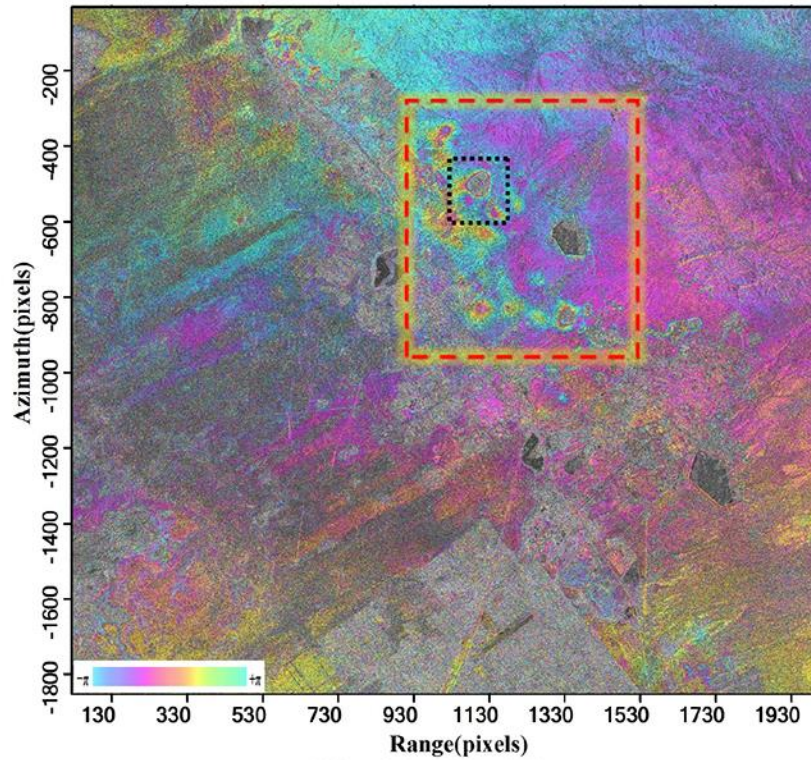
**Figure 3.5.** Geocoded displacement map in the line of sight (LOS) direction obtained by the differential SAR interferometry (D-InSAR) analysis from the ALOS-PALSAR data pair. Positive (negative) values indicates the ground close to (away from) the satellite.

### 3.4.2. Results of PS and SBAS-InSAR Interferometry

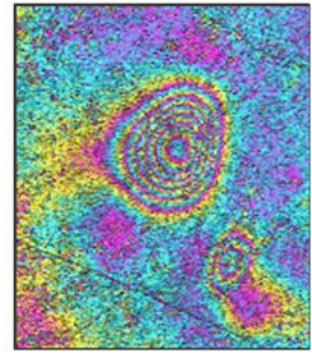
#### 3.4.2.1. Interferometric Phase Change over Time

The interferometric phase is useful for analyzing the ground deformation trends over time in the LOS direction [49]. The time series interferograms generated from each data pair from (a) to (k) are shown in **Figure 3.6**. Generally, we could roughly identify the deformation areas in the large scale by analyzing the fringe density in differential interferograms. In addition, the sequence of color fringes in the interferogram can be a good indicator of whether uplift or subsidence has taken place. **Figure 3.6a** shows a typical interferometric phase image, in which the fringes clearly show the areas with a high deformation rate.

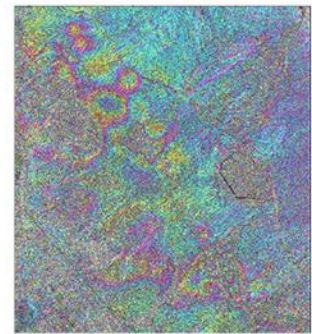
The ENVISAT-ASAR data were in the descending orbit and observations were made from the east. As shown in **Figure 3.6b**, the sequence of color fringes shows a decrease in range (yellow–purple–blue), which denotes that the ground objective moves closer to the satellite. In this study, we did not consider the horizontal movement, and thus, it corresponded to an uplift. To identify and highlight the time series of ground deformation in the period of 30 September 2003 to 15 June 2010, we selected a main deformation area, where the location is highlighted in red dashed lines in **Figure 3.6a**. As shown in the figure, a slight deformation can be observed from the earliest image in September 2003 to September 2006 (**Figure 3.6c–f**), the rate of deformation increases significantly from November 2007 (**Figure 3.6g–k**), and a pattern of rebound, expanding in area and increasing in quantity, can be observed during this period.



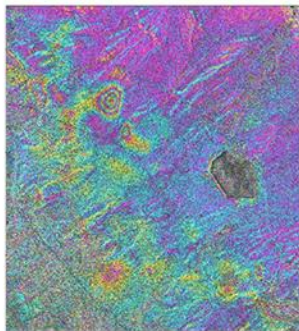
(a) 20061129 & 20080506  $B_p = 43$  m



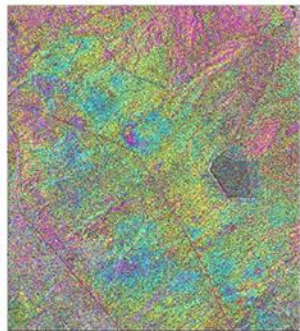
(b) Close up of the typical fringe



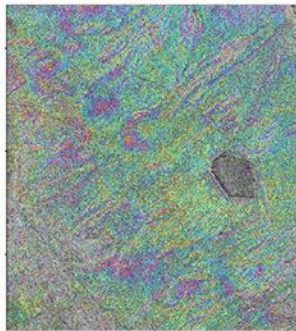
(c) 20030930  $B_p = -228$  m



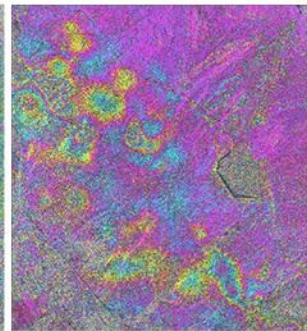
(g) 20071113  $B_p = 288$  m



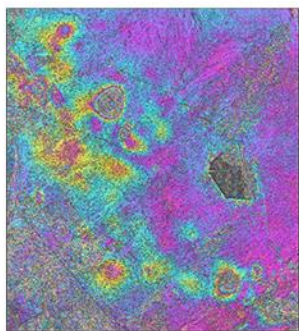
(f) 20060221  $B_p = -154$  m



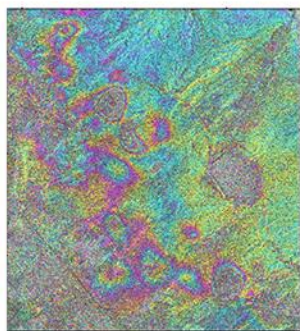
(e) 20051108  $B_p = 625$  m



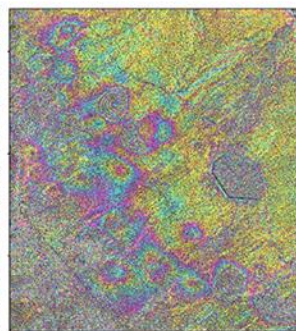
(d) 20041123  $B_p = 29$  m



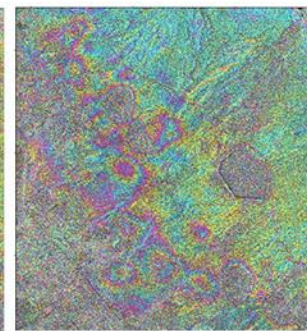
(h) 20080506  $B_p = 43$  m



(i) 20090630  $B_p = 171$  m



(j) 20091013  $B_p = 249$  m



(k) 20100615  $B_p = 243$  m

**Figure 3.6.** (a) The representative interferogram generated from the data pair (29 November 2006 and 6 May 2008); (b) Close-up view of a typical fringe map, where the location is indicated by the black dashed lines in Figure 3.6a. Figure from (c) to (k) correspond to the main deformation area, which is highlighted in a red dashed line in (a), and they show the interferometric phase change in different time periods. The image in 29 November 2006 is the common master image.

### 3.4.2.2. Mean Deformation Velocities and Temporal Evolutions

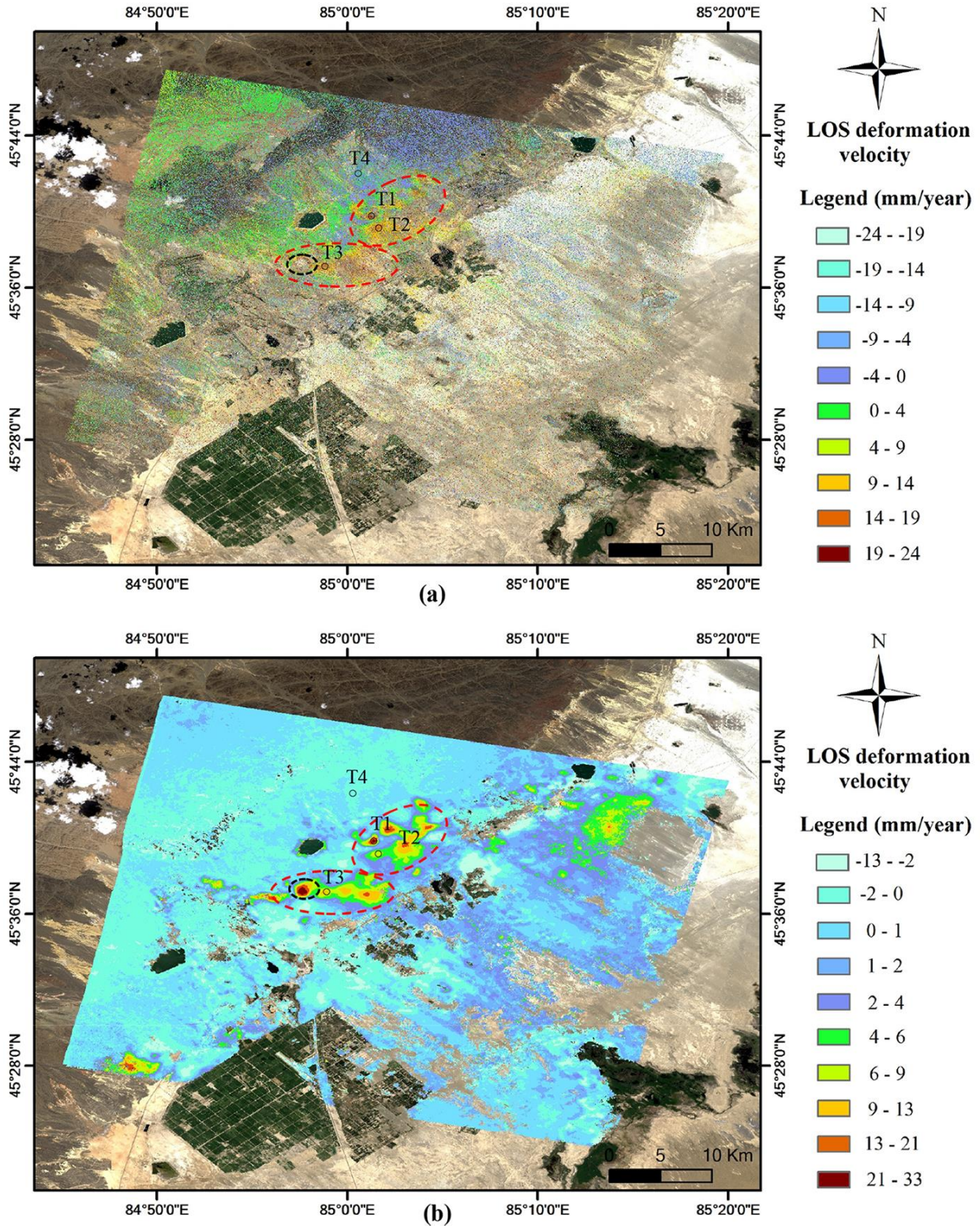


**Figure 3.7.** Mean displacement map of ENVISAT-ASAR data from 2003 to 2010. (a) The mean displacement velocity map of the PS-InSAR method; (b) The mean displacement velocity map of the SBAS-InSAR method. Positive (negative) values indicates the ground close to (away

from) the satellite. The points T1, T2, T3 and T4 are chosen for showing the accumulative time series land deformation pattern.

Analyses of the PS and SBAS-InSAR results from the ENVISAT-ASAR dataset show that significant surface uplift occurred over or near the oilfields over the study period (**Figure 3.7**). The spatial distributions and mean displacement velocity for the period from 30 September 2003 to 15 June 2010 are shown in **Figure 3.7a** (for PS-InSAR), **Figure 3.7b** (for SBAS-InSAR). Temporal decorrelation of bare land and agricultural areas were excluded by the coherence threshold. Major uplifted areas were highlighted by both PS and SBAS-InSAR methods and indicated in red dashed circles in **Figure 3.7a, b**. Dense PS points were detected around the reservoir area, whereas the distributions of PS points were sparse in other areas. The maximum deformation velocity was approximately 24 mm/year. The locations and the mean deformation velocity detected by the SBAS-InSAR technique were much clearer than the PS-InSAR results (**Figure 3.7b**). SBAS-InSAR also revealed a major uplift area that was not detected using the PS-InSAR, as indicated by the black dashed circles in **Figure 3.7a, b**. The estimated maximum deformation velocity was approximately 33 mm/year in the LOS direction.

**Figure 3.8** shows the PS and SBAS-InSAR measured displacements over time, from 30 September 2003 to 15 June 2010, for four specific points located within the major deformation area (**Figure 3.7**). Three typical reference points were selected with the induced deformation as T1–T3 and one stable reference point as T4, which are shown in **Figure 3.7a, b**. **Figure 3.8** illustrates that both PS-InSAR and SBAS-InSAR methods have good agreement in the deformation trend, with the time evolutions of each selected pixel sharing similar characteristics, such as increasing uplift. Despite a notable difference in values for T3, both PS-InSAR and SBAS-InSAR show a trend of consistently increasing deformation. The point T1 shows the largest deformation with the maximum uplift of 151.8 mm in 2010 in the LOS direction. The activity of the wastewater injection of the area may be responsible for the continuing land uplift.

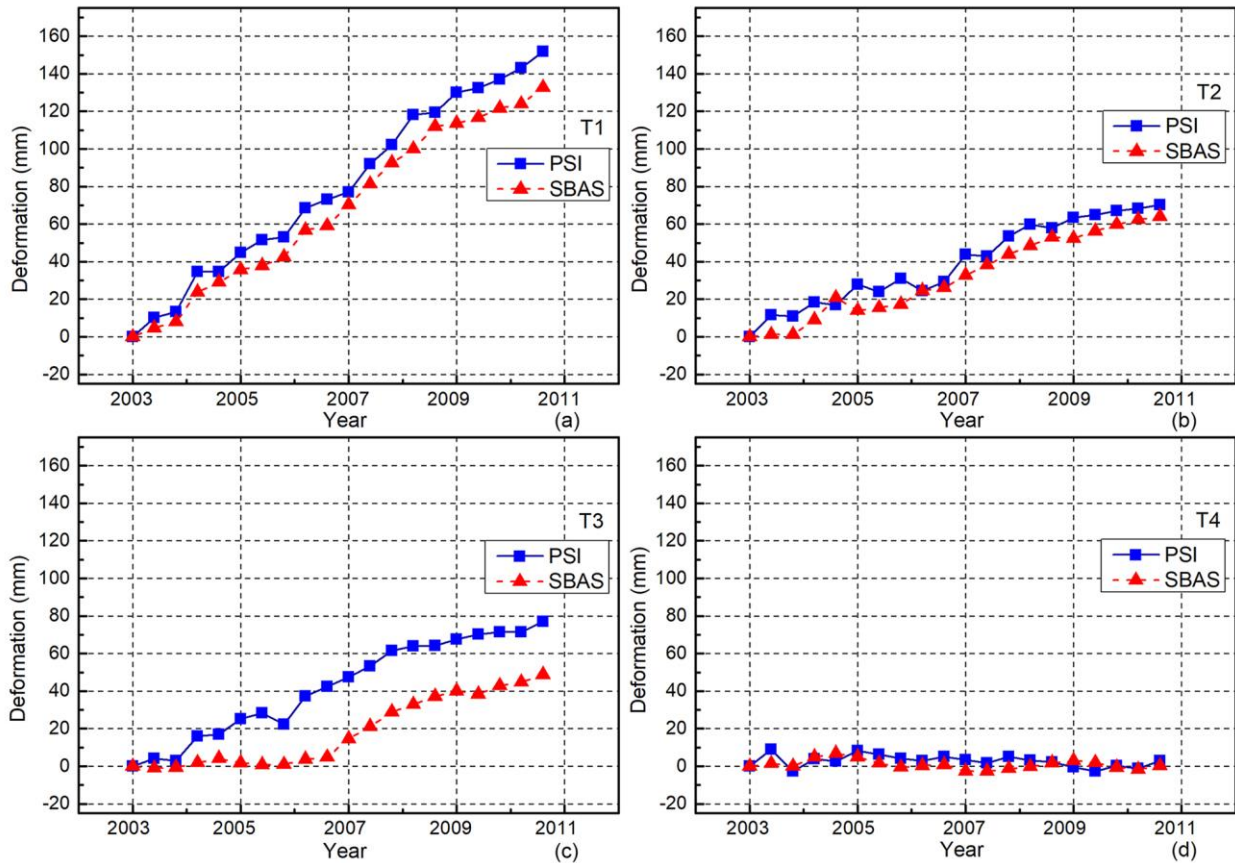


**Figure 3.8.** (a–d) Comparison of time series deformation obtained by the PS-InSAR and SBAS-InSAR methods at the selected locations T1 to T4 (Figure 3.7).

### 3.5. Comparison and Discussion

Quantitative accuracy assessment is essential for evaluating the usability and reliability of InSAR-derived deformation (Tantianuparp *et al.*, 2013). However, except for the one GPS station, no other ground measurements are available, and thus, an alternative approach was used to perform cross-validation among the results from the three InSAR methods.

To compare the deformation results obtained from the D-InSAR, PS and SBAS-InSAR methods, the mean deformation velocity of D-InSAR processing results was calculated by averaging the displacement values. As explained in previous Section 3.4.2.1, the rate of deformation in 2003–2006 is different from that in 2006–2010, and the D-InSAR derived deformation is obtained from the data in 2007–2009. That is, the D-InSAR results are only comparable to the deformation rate in 2006–2010. Therefore, the deformation rate of PS and SBAS-InSAR in 2006–2010 are considered for further comparison. We selected 500 reference

points from the PS-InSAR results in the study area, including both the stable and deformed areas (**Figure 3.9d**). The LOS displacement velocity for these points was plotted compared with the SBAS and D-InSAR results, and the correlation coefficients were calculated. The results show good agreement between the SBAS and D-InSAR methods with a correlation of 0.75, and the RMSE was approximately 4.918 mm/year. However, the results from the D-InSAR and PS-InSAR were not as comparable, with a low correlation of 0.54 and an RMSE of 6.043 mm/year. However, all the three methods could identify the main deformation areas, except for one of the main deformation areas in PS-InSAR indicated in black circles in **Figure 3.7a**. This may be caused by low backscatter in the wide non-urban land use, where the sufficient number of PS points could not be detected in the PS-InSAR processing.

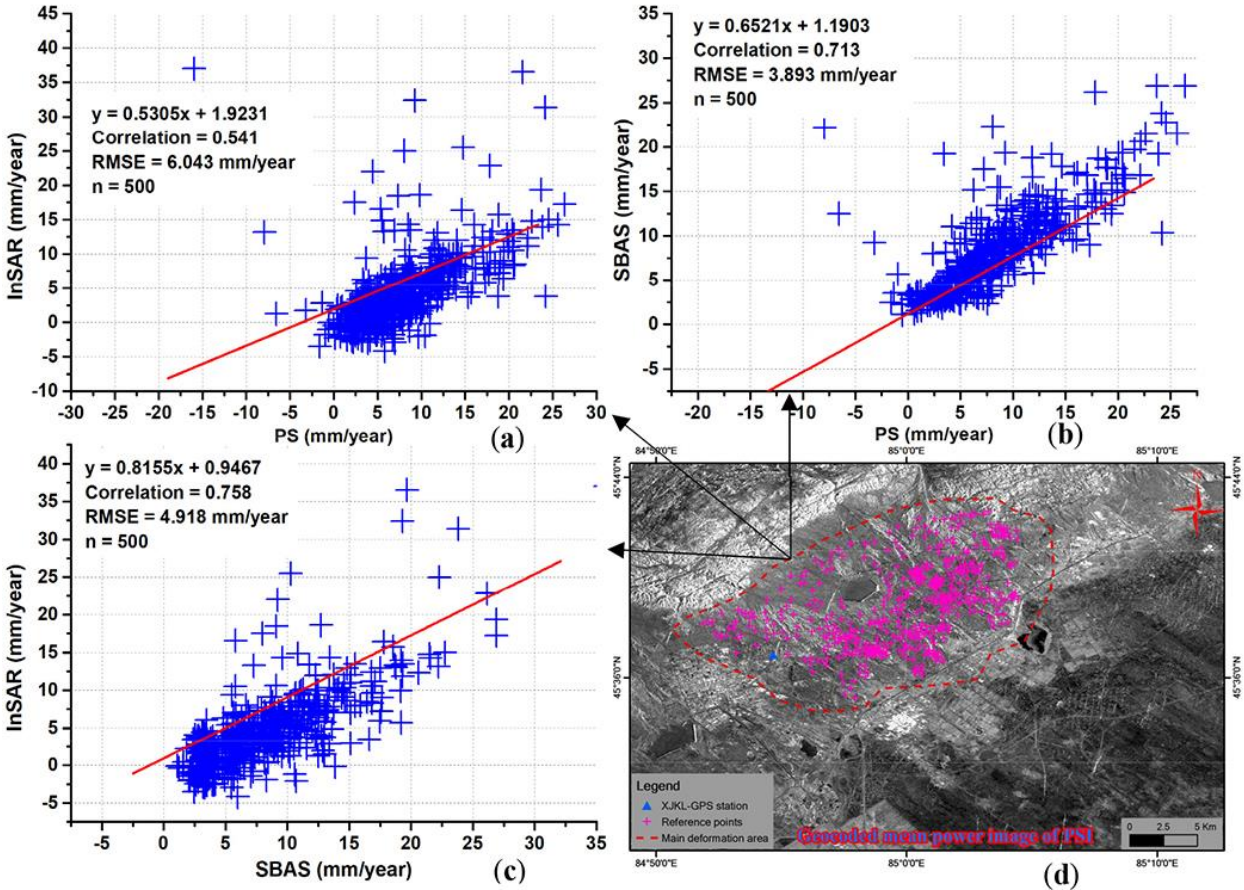


**Figure 3.9.** Comparison of mean deformation velocity among D-InSAR, PS-InSAR and SBAS-InSAR methods (a–c) for the selected locations, shown as pink cross lines, in (d), showing the distribution of the selected 500 reference points. The blue triangle denotes the location of previous GPS station (Ji *et al.*, 2016).

Although the XJKL is the only GPS station located within the study area and is insufficient to measure and represent the entire deformation area, it provides a means of assessing the accuracy of the InSAR data and methods used in this study. The deformation rate at the XJKL continuous GPS station was 9.6 mm/year, while the D-InSAR and SBAS-InSAR derived deformation rates were 1.2 and 7.4 mm/year, respectively. No displacement was found in the PS-InSAR measurement results. In addition, the identified deformation area and the temporal evolution pattern in this study agree well with the results obtained by Ji et al. (Ji *et al.*, 2016). In our study, the maximum deformations from 2003 to 2010 for SBAS and PS-InSAR were approximately 22.7 cm and 17.8 cm, respectively, and the results of D-InSAR was 13 cm for the period 2007 to 2009, which are comparable to the previous research results in which the maximum uplift magnitude was reported as 20 cm over the years 2006 to 2010 (Ji *et al.*, 2016). The comparison result shows slight differences between the two results, which might be caused by the differences in the deformation trend in the different periods, rather than any deficiencies in one method over the other. As shown in **Figure 3.6**, the deformation was evident and more accelerated from 2006 to 2010 than during the previous time of 2003 to 2006.

### **3.6. Conclusion**

To assess the degree of deformation in the oilfields of Karamay, Xinjiang, China, the D-InSAR technique was applied to ALOS-PALSAR data and the PS-InSAR and SBAS-InSAR to the ENVISAT-ASAR dataset. The results showed that all the three methods could provide useful information for identifying the boundaries of deformation and revealed two areas of land uplift near the oilfield. The maximum deformation velocity was estimated to be 33 mm/year. As previous research suggests, the subsurface water injection used to enhance oil recovery is the likely cause of this land uplift. The comparison of results from each of the three methods indicates that the correlation of the SBAS-InSAR and D-InSAR results is higher than that of the PS-InSAR and D-InSAR results. For this study area, the SBAS-InSAR method was found to be more robust than the PS-InSAR method. Future investigation can improve the findings of this study by utilizing GPS base stations in the high deformation areas and monitoring long-time land deformation in combination with more accurate and improved satellite data.



## Chapter 4

# Multi-Sensor InSAR Analysis of Progressive Land Subsidence over the Coastal City of Urayasu, Japan

### 4.1. Introduction

Land subsidence is one of the most serious environmental problems in many urban areas around the world (Pradhan *et al.*, 2014). In particular, coastal areas, which contain young and compressible deposits, are often vulnerable to subsidence caused by either anthropogenic or natural factors (Chaussard *et al.*, 2013; Tessler *et al.*, 2015). This phenomenon is evident in the coastal city of New Orleans, LA in the USA (Jones *et al.*, 2016), Jakarta in Indonesia (Abidin *et al.*, 2011; Ng *et al.*, 2012), Ho Chi Minh in Vietnam (Ho Tong Minh, Van Trung and Le Toan, 2015), Bangkok in Thailand (Aobpaet *et al.*, 2013), Shanghai and Shenzhen in China (Dong *et al.*, 2014; Xu *et al.*, 2016), Venice in Italy (Tosi, Teatini and Strozzi, 2013) and in the western Netherlands (Koster, Erkens and Zwanenburg, 2016). Continuous land subsidence causes remarkable economic losses in the form of building damages leading to high maintenance costs (Raspini *et al.*, 2014). Thus, identifying land deformation trends is a crucial task to maintain the sustainability of coastal urban areas (Normand and Heggy, 2015).

Over the past two decades, land subsidence monitoring has been significantly improved by the use of interferometric synthetic aperture radar (InSAR) techniques (Cianflone *et al.*, 2015). Although the traditional methods (i.e., global positioning system (GPS) and leveling) can also provide precise measurements, they cannot acquire dense ground displacement measurements with a large-scale coverage in a short time and at a low cost (Hsieh *et al.*, 2011). The advanced time-series InSAR techniques, such as persistent scatterers interferometry (PSI) and the small baseline subset (SBAS) technique, can achieve results in better spatial and temporal resolutions with higher precision (Ferretti, Prati and Rocca, 2000, 2001; Berardino *et al.*, 2002; Hooper *et al.*, 2004). Furthermore, the increase in the available synthetic aperture radar (SAR) satellites with different temporal and spatial resolutions has provided a great opportunity for researchers to perform long-term geohazard monitoring by combining observations from those satellites (Armas *et al.*, 2017).

Urayasu City is located in the Tokyo Bay area, where more than 70% of the area was reclaimed from 1964 to 1980 (Tokimatsu *et al.*, 2012; Yasuda *et al.*, 2012). The reclamation was performed using the sand and soil dredged from the seabed off the coast of Urayasu (Nigorikawa and Asaka, 2015). In addition, Urayasu City is located in an earthquake-prone area, which increases the risk of land subsidence due to the combined effects of seismicity and the natural consolidation of soil (Okada *et al.*, 2011; Zhou *et al.*, 2017). On 11 March 2011, a devastating earthquake of moment magnitude Mw 9.0 occurred off the coast of Tohoku, Japan, which caused severe damage to buildings and infrastructures and created large ground settlements of up to 60 cm in the reclaimed areas (Bhattacharya *et al.*, 2011; Tokimatsu and Katsumata, 2012). This catastrophic event has attracted a great deal of attention from researchers and organizations. The Geospatial Information Authority of Japan (GSI) carried out a leveling survey, comparing the results with light detection and ranging (LiDAR) survey data, and concluded that the surface subsidence was not caused only by the soil liquefaction but also by pro-earthquake consolidation (Imakiire and Koarai, 2012). Konagai *et al.* (Konagai *et al.*, 2013) mapped the soil subsidence using LiDAR data taken before and after the earthquake. Pasquali *et al.* (Pasquali *et al.*, 2015) measured the land subsidence during 2006–2010 using both the Environment Satellite Advanced Synthetic Aperture Radar (ENVISAT ASAR) and the Advanced Land Observation Satellite Phased Array L-band Synthetic Aperture Radar ALOS PALSAR data. ElGharbawi and Tamura (ElGharbawi and Tamura, 2015) estimated the liquefaction induced deformation using ALOS PALSAR images spanning from August 2006 to April 2011. Nigorikawa and Asaka (Nigorikawa and Asaka, 2015) conducted a leveling survey from April 2011 to April 2013 and found accelerated land settlement only in the reclaimed land areas rather than in the natural alluvial low land and pointed out the settlement may still be ongoing. However, the previous studies mainly focused on the soil liquefaction-induced subsidence during the earthquake, and the long-term spatiotemporal evolution of land subsidence before and after the earthquake has not yet been clearly identified.

In this study, we used three different SAR datasets, the European Remote Sensing satellites (ERS-1/-2) and ALOS PALSAR & ALOS-2 PALSAR-2 to identify the trends of land subsidence dynamics in Urayasu City over a period of 24 years by using multitemporal InSAR techniques. Moreover, the InSAR results were compared with leveling survey data. The observed results may provide useful information for identifying and understanding the behavior of the slow subsidence phenomenon over a long-time period, which plays an important role in future risk mitigation strategies.

## 4.2. Study area

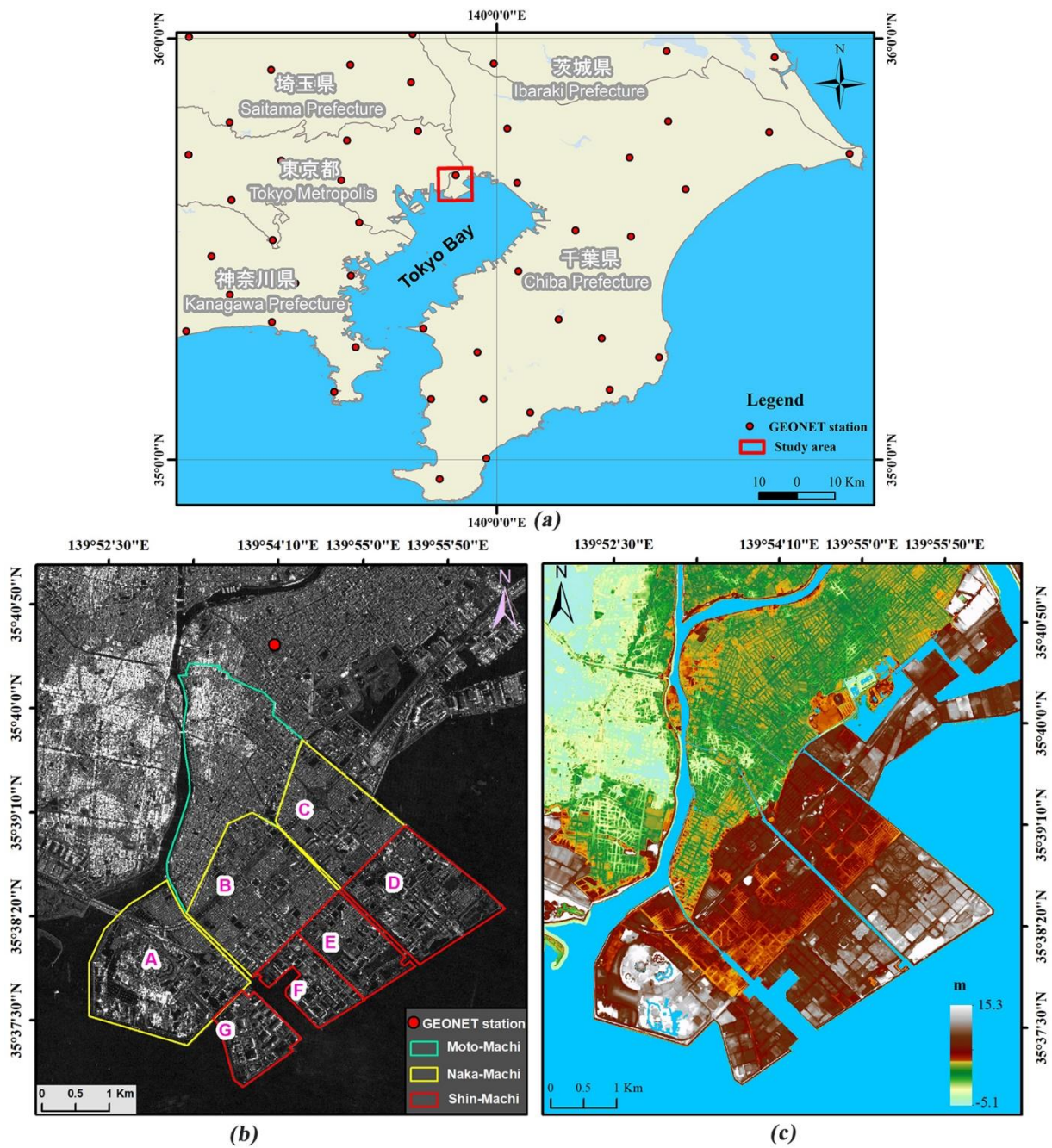


**Figure 4.1.** The map of the study area, Urayasu City, Japan. (a) The geographic location of Urayasu City; (b) the distribution and development history of the reclaimed areas, namely Moto-Machi (old town) outlined in green, Naka-Machi (central town) outlined in yellow and Shin-Machi (new town) outlined in red. A to G represent the reclaimed areas at different times. The background image is a Phased Array L-band Synthetic Aperture Radar onboard the Advanced

Land Observation Satellite (ALOS-2 PALSAR-2) intensity image acquired on 4 December 2014; and (c) the topography of the study area (GSI, 2018b).

Urayasu City is located in the Tokyo Bay area of Chiba Prefecture, from 139°56'22''E to 139°52'20''E and from 35°37'N to 35°40'23''N. The total area is 16.98 km<sup>2</sup>, and the total population was 167,950 in February 2018 (*Urayasu City population statistics*, 2018). As shown in Figure 4.1, Urayasu City is divided into three areas, namely, Moto-Machi (old town), Naka-Machi (central town) and Shin-Machi (new town). Moto-Machi is a naturally formed Holocene lowland, and the other two areas were reclaimed from 1964 to 1980 (Urayasu City, 2009; Tokimatsu *et al.*, 2013). **Figure 4.1b** and **Table 4.1** shows the distribution and other detailed information of those reclaimed areas. The elevation in the old coastline area of Moto-Machi is approximately 0 to 2 m and gradually increases towards the coastal levee, becoming especially high in Sogo Park of Akemi district and the Tokyo Disney resort area (**Figure 4.1c**). The thickness of the alluvial soil layers varies from 20 m in the Moto-Machi area to 60–80 m in the Naka-Machi and Shin-Machi areas, which indicates the complexity of the soft soil distribution in those areas (Tokimatsu *et al.*, 2012; Yasuda *et al.*, 2012).

**Table 4.1.** The detailed history of reclaimed areas and the districts.

Reclaimed Areas	Reclaimed Year	Districts
A	1975	Maihama
B	1968	Higashino, Tomioka, Imagawa, Benten and Tekkadori
C	1971	Kairaku, Mihama and Irifune
D	1978	Akemi and Hinode
E	1980	Takasu
F	1979	Minato
G	1979 and 1981	Chidori

### 4.3. Data Sets and Methods

#### 4.3.1. Data Sets

In this study, the SAR data collected by the ERS-1/-2 and ALOS-1/-2 satellites were used to monitor the long-term deformation pattern of Urayasu City. The ERS-1/-2 data were provided by the European Space Agency (ESA) and the PALSAR & PALSAR-2 data by the Japan Aerospace Exploration Agency (JAXA). A total of 52 C-band ERS-1/-2 single look complex (SLC) scenes

were acquired from the track/frame 489/2889 during the period from May 1993 to February 2006. Note that there is a data gap in 1994 and 1995 due to the limited acquisitions of ERS-1 data; 24 L-band ALOS PALSAR SLC data were acquired from the path/frame 58/2900 during the period from June 2006 to December 2010; 13 L-band ALOS-2 PALSAR-2 SLC data were acquired from the path/frame 18/2900 during the period from December 2014 to November 2017. The detailed acquisition parameters of these three SAR data are given in **Table 4.2**.

A 5-m high-resolution digital elevation model (DEM) provided by the GSI was used as a reference to remove the topographic phase in the multitemporal InSAR processing (GSI, 2018b). The daily GPS data observed by the GPS earth observation network system was used as reference point, and the leveling survey measurement data was used to validate the InSAR derived deformation. The daily GPS data was provided by the GSI of Japan. The leveling survey measurements have been conducted by the Chiba Prefecture on an annual basis, and the results are publicly available at their official website (Chiba Prefecture, 2017a). The archived leveling survey data before 2008 was obtained from the Chiba Prefectural Archives.

**Table 4.2.** Acquisition parameters of the ERS-1/-2, ALOS PALSAR and ALOS-2 PALSAR-2 data sets.

SAR <sup>1</sup> Sensor	ERS-1/-2 <sup>2</sup>	ALOS PALSAR	ALOS-2 PALSAR-2
Orbit direction	Descending	Descending	Descending
Operation mode	SAR/IM <sup>3</sup>	FBS/FBD <sup>4</sup>	Strip map (SM) <sup>1</sup>
Band (wavelength)	C-band (5.6 cm)	L-band (23 cm)	L-band (23 cm)
Resolution	20 m	10/20 m	3 m
Revisit cycle	35 days	46 days	14 days
Look angle	23°	34.3°	35.4°
Incidence angle	23.3°	38.7°	39.7°
Swath	100 km	70 km	50 km
Number of images	52	24	13
Temporal coverage	May 1993 to February 2006	June 2006 to December 2010	December 2014 to November 2017

<sup>1</sup> synthetic aperture radar; <sup>2</sup> European Remote Sensing satellites; <sup>3</sup>IM: image mode; <sup>4</sup> FBS: fine beam single; FBD: fine beam double.

### 4.3.2 Methodology

The multitemporal InSAR methodologies involve the use of multiple SAR datasets to overcome the limitations of conventional InSAR (e.g., spatial and temporal decorrelations and atmospheric disturbance) and measure the land surface displacements with high precision (Hooper, 2008; Grzovic and Ghulam, 2015; Qu *et al.*, 2015). In this study, the PSI and the SBAS were applied to the archived (i.e., ERS-1/-2 and ALOS PALSAR) and recent (i.e., ALOS-2 PALSAR-

2) SAR data. The PSI method utilizes a time-series of radar images to identify high coherent points, the so-called persistent scatterers (PS) (Ferretti, Prati and Rocca, 2000, 2001; Hooper *et al.*, 2004); the SBAS method uses distributed scatterers from all available SAR images with corresponding small baselines in order to reduce the spatial decorrelation and obtain the time-series displacements (Berardino *et al.*, 2002). The reason for using both techniques relies on the fact that the PSI applicability is limited to temporally uniform rates of displacement, while the SBAS has the ability to capture strong nonlinearities in the study area (Hooper *et al.*, 2012). The PSI has a high sensitivity to slow displacements but suffers severe limitations in the capability to measure “fast” deformation phenomena, and the PS density is usually low in vegetated, forested and low-reflectivity areas (e.g. very smooth surfaces) (Crosetto *et al.*, 2016), while the SBAS performs better in nonurban vegetated areas, and also in areas with high deformation rates (Gourmelen, Amelung and Lanari, 2010; Chaussard *et al.*, 2014).

As shown in **Figure 4.2**, the ERS-1/-2 and PALSAR data were processed using both the PSI and SBAS methods. Due to the limited number of PALSAR-2 acquisitions, we used only the SBAS method. The SARscape® Modules (5.4) for ENVI (5.4) software suite (HARRIS Geospatial Solutions, Broomfield, CO, USA) was employed to perform the interferometric analyses. For the ERS-1/-2 data, we used the latest precise orbit products provided by the ESA to correct the orbit inaccuracies (ESA, no date) and generate a total of 424 interferograms, including 36 for PSI processing and 388 for SBAS processing pairs (**Figure 4.2a** and **b**). The PSI pairs were generated with respect to the master image from 24 January 2000. The normal baselines range from 22 m to 557 m. A custom atmospheric filtering was performed with a low pass spatial filter with a  $1.2 \text{ km} \times 1.2 \text{ km}$  window and a temporal high pass filter at 365 days. The mean coherence threshold of 0.56 was used to identify the PS candidates. To obtain more accurate displacement measurements, the GPS base station was used as a reference point in the geocoding process (**Figure 4.1b**). The SBAS pairs were generated with respect to the multi-master images and by setting spatial and temporal threshold criteria. The threshold criteria for the absolute mean of the normal baselines was 210 m and that for the absolute mean of the temporal baselines was 937 days. Moreover, the image acquired on 2 August 1999 formed the largest number of interferometric pairs, when used as a master scene. For that reason, it was chosen as a reference (i.e., super master image). Therefore, all the slave scenes are co-registered to this reference geometry (**Figure 4.2b**). To increase the signal-to-noise ratio of the interferograms, a multi-looking factor of one in range and five in azimuth was used, producing a ground resolution of about 20 m. The topographic phases in both the PSI and SBAS interferograms were removed

using the 5-m DEM data. After that, we visually checked the intermediate products (i.e., flattened and filtered (wrapped) interferograms and the unwrapped phases) to detect possible errors, which were caused by strong orbit inaccuracy, non-coherent pairs, atmospheric artefacts, residual topography etc., and 23 interferometric pairs were discarded from further processing. For refinement and re-flattening, we selected 45 reference points where the unwrapped phase value was close to zero and the flat areas were identified from the unwrapped interferograms and the topographic map. The linear inversion model was used to estimate the residual height and the displacement velocity for both the PSI and SBAS processing (Berardino *et al.*, 2002).

For the PALSAR data, we used both fine beam single (FBS) polarization and fine beam double (FBD) polarization images, with an horizontal transmit and horizontal receive (HH) polarization mode, and generated a total of 150 interferograms, including 21 for PSI processing and 129 for SBAS processing pairs (**Figure 4.2c** and **4.2d**). The PSI pairs were generated with respect to the master image of 5 August 2009. The normal baselines range from 237 m to 3084 m. The same atmospheric filter which was used for the ERS-1/-2 PSI processing was also used to remove the atmospheric phase components. The mean coherence threshold of 0.75 was used to identify the PS candidates. The same GPS base station used for the ERS-1/-2 PSI processing was used as a reference point in the geocoding process. The SBAS pairs were generated with respect to the multi-master images and by setting spatial and temporal threshold criteria. The threshold criteria for the absolute mean of the normal baselines was 1084 m and that for the absolute mean of the temporal baselines was 453 days. The image acquired on 20 March 2009 was chosen as a super master image (**Figure 4.2d**). A multi-looking factor of one in range and five in azimuth was used, producing a ground resolution of about 15 m. The topographic phase in both the PSI and SBAS interferograms was removed using the same DEM used for the ERS data. Four interferometric pairs were removed due to the unwrapping errors. The same reference points used in ERS-1/-2 SBAS processing were also used for the refinement and re-flattening. The same linear inversion model was used for both the PSI and SBAS processing. In **Figure 4.2**, (a) is the time–position plot of PSI interferograms generated by the ERS-1/-2 data, with 24 January 2000 as the master image; (b) time–baseline plot of SBAS interferograms generated by the ERS-1/-2 data, with 2 August 1999 as the super master image; (c) time–position plot of PSI interferograms generated by the ALOS PALSAR data, with 5 August 2009 as the master image; (d) time–position Delaunay 3D plot of SBAS interferograms generated by the ALOS PALSAR data, with March 20, 2009 as the super master image; (e) time–position Delaunay 3D plot of SBAS interferograms generated by the ALOS-2 PALSAR-2 data, with 4 December 2014 as the super master image; and (f) the

histogram of the average coherence for the three satellite datasets. These connections in (d) and (e) are a subset of the whole main network and represent such interferograms that will be unwrapped in a 3D way.

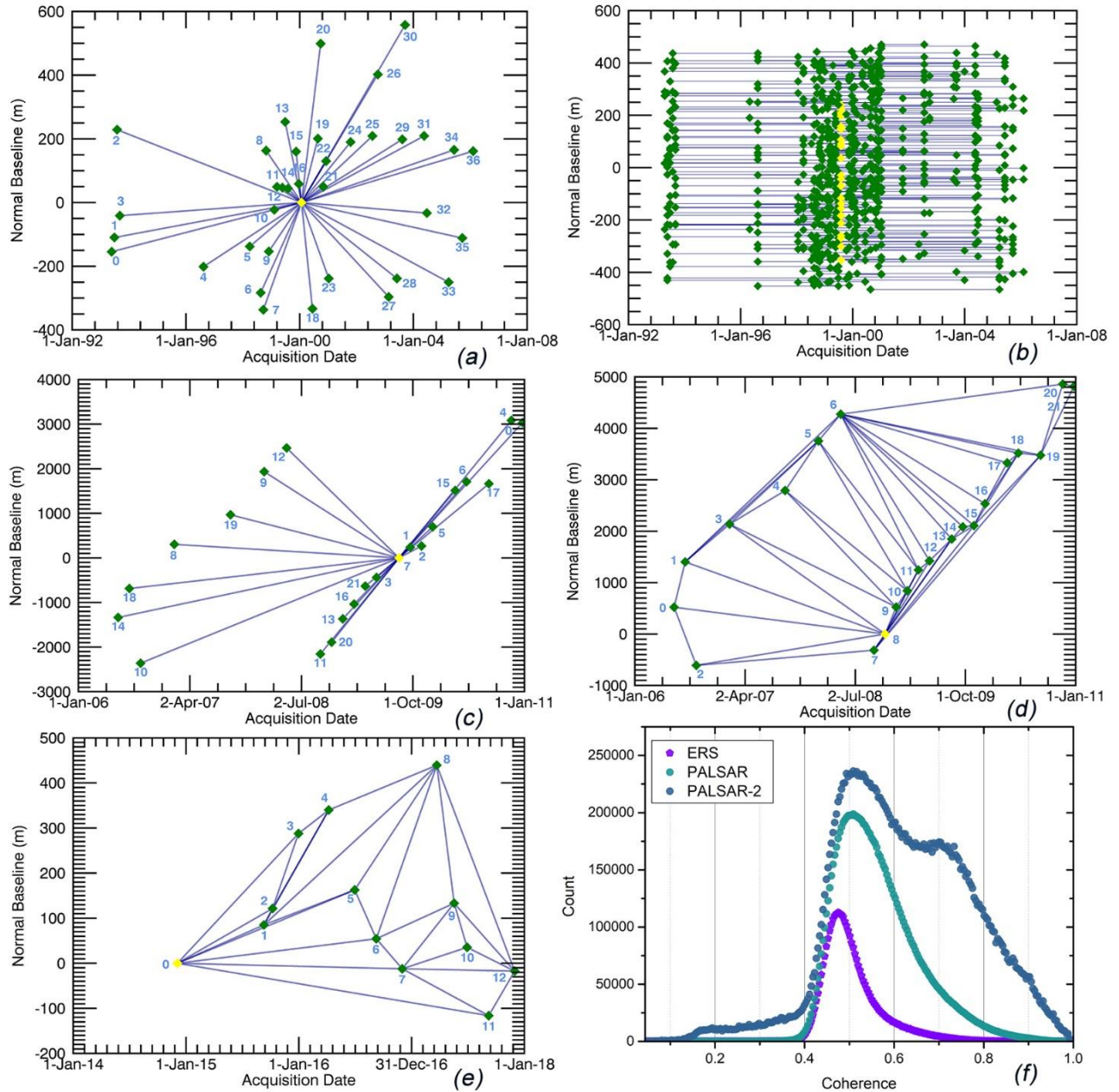


**Figure 4.2.** The temporal and spatial baseline distributions of the SAR interferograms from the ERS-1/-2, ALOS PALSAR and ALOS-2 PALSAR-2 data sets (a–e), where each acquisition is represented by a diamond associated to an ID number; the green diamonds represent the valid acquisitions and the yellow diamonds represent the selected master image of persistent scatterers interferometry (PSI) and super master image of the small baseline subset (SBAS).



The histogram of the average coherence for the PALSAR-2 data shows the relatively good coherence of PALSAR-2 when compared with the ERS-1/-2 and PALSAR data (**Figure 4.2f**). For the PALSAR-2 data, we generated 78 interferograms for SBAS processing (**Figure 4.2e**), with respect to the multi-master images. The threshold criteria for the absolute mean of the normal baselines was 182 m and that for the absolute mean of the temporal baselines was 386 days. The image acquired on 4 December 2014 was chosen as a super master image. A multi-looking factor of six in range and seven in azimuth was used, producing a ground resolution of about 15 m. The topographic phase was removed using the same DEM used for the PALSAR data processing. To smooth the differential phase, the Goldstein filter was applied (Goldstein and Werner, 1998). The minimum cost flow (MCF) network and Delaunay 3D method were employed to unwrap the differential interferograms (Costantini, 1998; Hooper and Zebker, 2007) with an unwrapping coherence threshold of 0.35. The same reference points used in PALSAR SBAS processing was also used for the refinement and re-flattening. The linear inversion model was used in the processing. All the final displacement measurements were measured in the satellite line of sight (LOS) direction and were geocoded in the WGS84 reference ellipsoid with a 25-m ground resolution.

## **4.4. Results**

### **4.4.1. Time-Series Analysis of the ERS-1/-2 Data from May 1993 to February 2006**

The mean velocity (mm/year) maps of the final geocoded displacements generated from the ERS-1/-2 data are shown in **Figure 4.3a** (for PSI) and **4.3b** (for SBAS). The color cycle from green to purple indicates the positive to negative velocities in the LOS direction. The negative values indicate that the surface is moving away from the satellite (i.e., subsidence) while the positive values indicate the opposite direction of movement (i.e., uplift). As shown in **Figure 4.3a** and **4.3b**, the major subsidence areas were highlighted by both InSAR measurements, which were located on the borders of the Naka-Machi and Shin-Machi areas. The results derived from the SBAS method show higher densities of the obtained points than those of the PSI. In the study area of over 860,256 pixels, 54,458 measurement points were obtained by the PSI method, and 89,251 points by the SBAS method. The presence of vegetation in Urayasu City, namely the palm trees in the streets and parks might cause this difference. The histograms of the estimated displacement velocities by the PSI and SBAS for the study area are shown in **Figure 4.4a** and **4.4b**, respectively. The average displacement rate and the standard deviation for the PSI were -1.0 and 4.9 mm/year, while those for the SBAS were -0.95 and 1.9 mm/year, respectively. In general, the ERS-1/-2

results show that approximately 85% of the PS points indicate displacement rates between -4 mm/year and 2 mm/year (**Figure 4.4**).

**Figure 4.5** shows the measured displacement histories for eight representative points, which are shown in **Figure 4.3**. For both the PSI and SBAS measurements, the patterns of subsidence for each point show similar characteristics, such as an increase in subsidence rates. However, point P1 located in Moto-Machi shows very low subsidence rates (-0.1 and -0.9 mm/year for PSI and SBAS, respectively) compared to those in other areas. This suggests that the Moto-Machi area had relatively stable ground conditions during the ERS-1/-2 monitoring period. It is worth mentioning that the PSI's estimated displacement velocity is almost two times more than the SBAS results; this may be caused by the different reference points selected in the two methods. We also calculated the correlation coefficient between PSI and SBAS results over those selected points using the Pearson correlation coefficient (Lawrence, I., 1989; Aimaity *et al.*, 2017). Most of those points showed relatively good correlation, while the P1 and P3 showed low correlation. However, the points P1 (-0.1mm/year vs -0.8mm/year) and P3 (-0.7 mm/year vs -2.3 mm/year) both show a small displacement velocity. To provide a quantitative comparison of the estimated time series for those selected points, we calculated the velocity difference between the two methods. The smallest velocity difference was 0.7 mm/year (P1), while the largest velocity difference was 12.6 mm/year (P7). The average velocity difference for all points between the two methods was 4.6 mm/year.

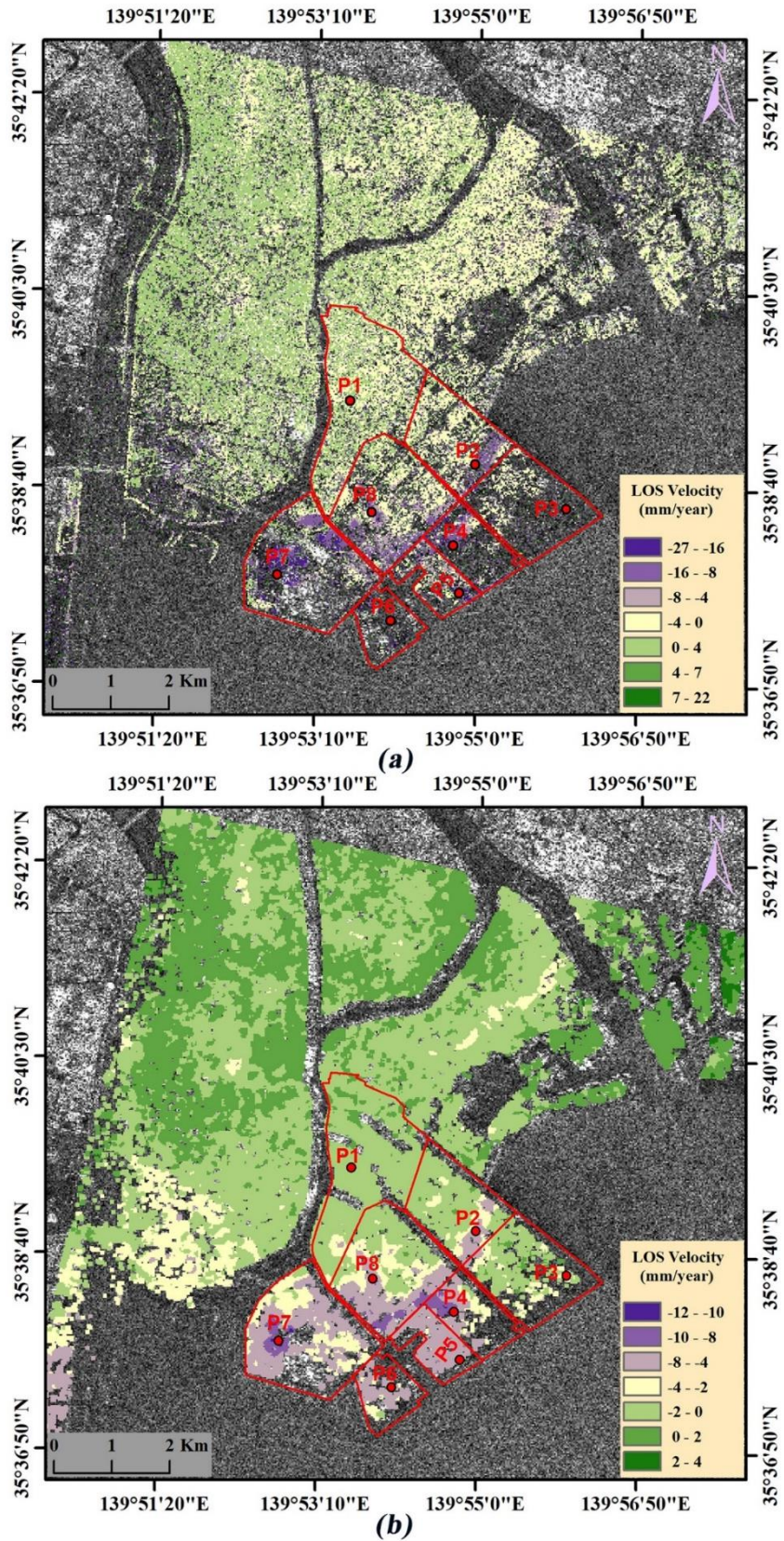


**Figure 4.3.** Line of sight (LOS) displacement velocity in Urayasu City from 1993 to 2006 for the ERS-1/-2 data: (a) Estimated mean displacement velocity using the PSI method; (b) estimated

mean displacement velocity using the SBAS method. The background image is an ERS-2 intensity image acquired on May 24, 1999. The red points P1 to P8 are the selected points to show the time-series LOS displacements estimated by the PSI and SBAS measurements in (a) and (b), respectively.

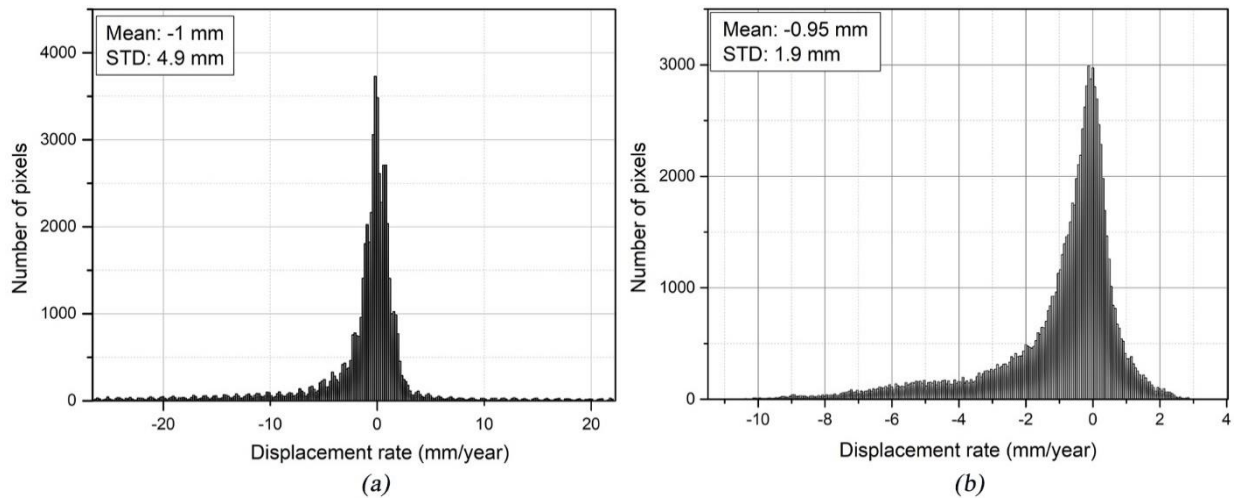


**Figure 4.4.** Histogram distribution for the ERS-1/-2-derived displacement rates from May 1993 to February 2006: (a) the corresponding histogram of the PSI measurements from the ERS-1/-2 data; and (b) the corresponding histogram of the SBAS measurements from the ERS-1/-2 data.

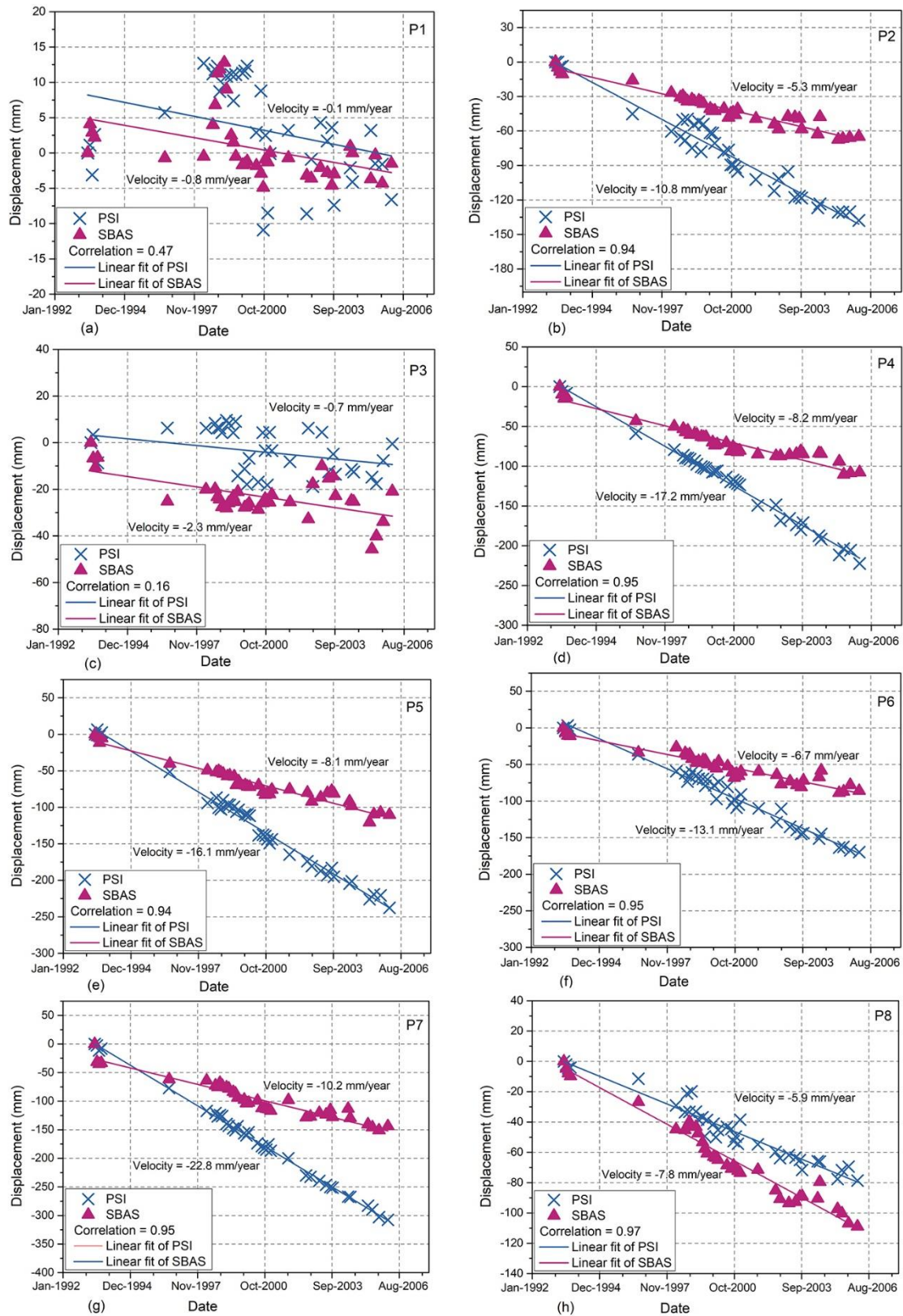


**Figure 4.5.** Time-series LOS displacement plots of the PSI and SBAS measurements from the ERS-1/2 data (a-h) for the selected points P1 to P8, which are indicated by red points in **Figure 3**.

#### 4.4.2. Time-Series Analysis of the PALSAR Data from June 2006 to December 2010

The mean velocity (mm/year) maps of the displacements for the period from June 2006 to December 2010 is shown in **Figure 4.6a** for PSI and **4.6b** for SBAS. The same color cycle from green to purple was used for those results. As shown in **Figure 4.6a** and **4.6b**, the density of the measured points by the PSI is coarser than those by the SBAS, due to the existence of vegetation in the study area. In the study area of over 695,387 pixels, 50,441 measurement points were obtained by the PSI method, and 78,044 points by the SBAS method. The histograms of the estimated displacement velocity by the PSI and SBAS for the study area are shown in **Figure 4.7a** and **4.7b**, respectively. The average displacement rate and the standard deviation for the PSI were -1.3 and 3.9 mm/year, whereas those for the SBAS were -1.7 and 3.3 mm/year, respectively. Overall, the PALSAR results show that approximately 85% of the PS points indicate displacement rates between -6 mm/year and 3 mm/year (**Figure 4.7**).

During the PALSAR monitoring period, most of the previously detected subsidence areas were also detected in this period, but the spatial distributions of subsidence are reduced (e.g., the areas such as points P2, P4, P5 and P8 located in **Figure 4.6a** and **4.6b**). This indicates that most of those areas were experiencing continuous subsidence over the study period, but the magnitude was beginning to decrease. This is evident at the points P2 and P4 (Naka-Machi) and P8 (Shin-Machi) that showed a decrease in displacement velocity compared to the ERS-1/-2 monitoring period. In addition, the leveling data at the points U-8, U-10, U-11, U-13 and U-14 also reveal that the subsidence rate has begun to decrease from 2003 (Chiba Prefecture, 2017a). However, significant subsidence was identified in the coastal levee areas (i.e., the Maihama (A), Akemi and Hinode (D), Takasu (E), Minato (F) and Chidori (G) districts), which was not identified by the ERS-1/-2 data (**Figure 4.6**). In general, the PALSAR (L-band) has a longer wavelength than the ERS-1/-2 (C-band), which has less decorrelation over vegetated terrain and has better coherence (Rosen *et al.*, 1996). Thus, the results of the PALSAR data offer a higher density of PS pixels. Therefore, we can assume that these areas may have been experiencing subsidence during the ERS-1/-2 monitoring period and may have been excluded from further processing due to the low coherence exhibited in these areas in the ERS-1/-2 data. Another reason for those differences is that the subsidence in the coastal levee may have started during the PALSAR monitoring period.

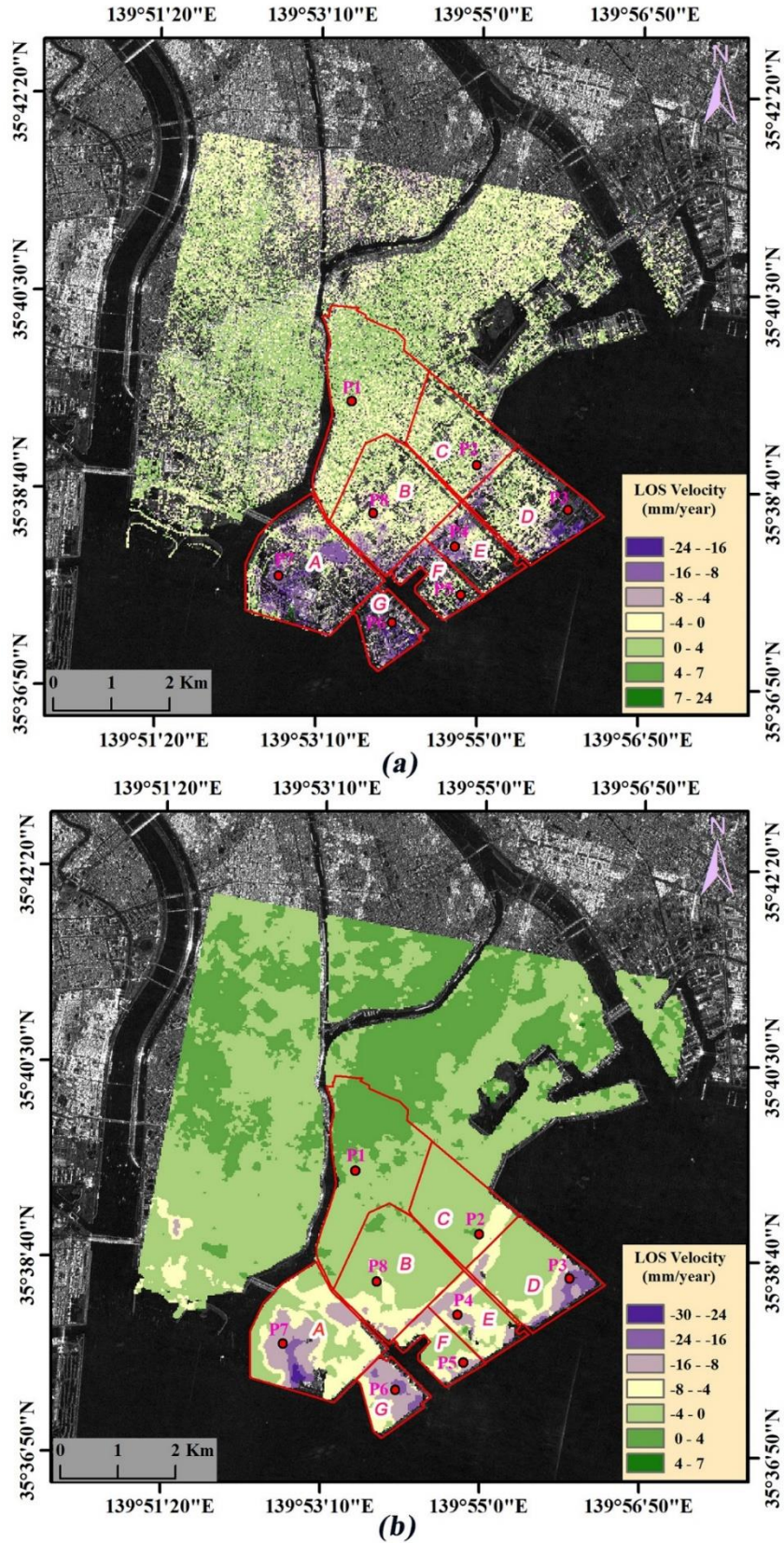


**Figure 4.6.** Mean LOS displacement velocity in Urayasu City from 2006 to 2010 for the PALSAR data: (a) estimated mean displacement velocity using the PSI method; (b) estimated

mean displacement velocity using the SBAS method. The background image is a PALSAR-2 intensity image acquired on 04 December 2014. The red points P1 to P8 are the selected points to show the time-series LOS displacements estimated by the PSI and SBAS measurements in (a) and (b), respectively. A-G represent the reclaimed areas and districts which described in **table 4.1**.

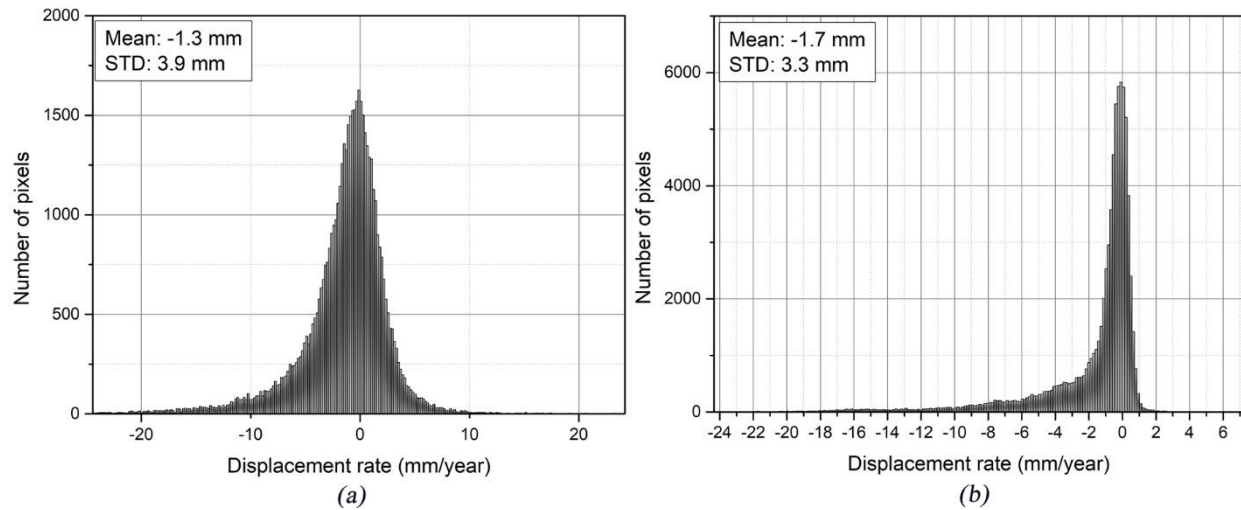


**Figure 4.7.** Histogram distribution for the PALSAR-derived results from June 2006 to December 2010. (a) The corresponding histogram of the PSI measurements from the PALSAR data; and (b) the corresponding histogram of the SBAS measurements from the PALSAR data.

**Figure 4.8a** to **4.8h** shows the measured displacement time-series for eight representative points, which are shown in **Figure 4.6a** and **4.6b** (the same points in **Figure 4.3a** and **4.3b**). From **Figures 4.8a** to **4.8h**, we can see that the time-series LOS deformations derived by both the PSI and SBAS processing showed good agreement in the subsidence trend. The estimated deformation rates by the PSI and SBAS measurements on points P1, P2, P4, P7 and P8 showed a velocity difference of less than 3 mm/year, while the points P3, P5 and P6 showed the largest velocity difference of over 5 mm/year. The average velocity difference for all points between the two methods was 2.9 mm/year. In general, similar to the ERS-1/-2 monitoring period, the Moto-Machi area also showed very low subsidence rates in the PALSAR monitoring period. This may be related to the fact that, in most parts of the Moto-Machi area, the urban infrastructures and houses are built over the naturally formed Holocene lowland that has stable ground conditions over time.



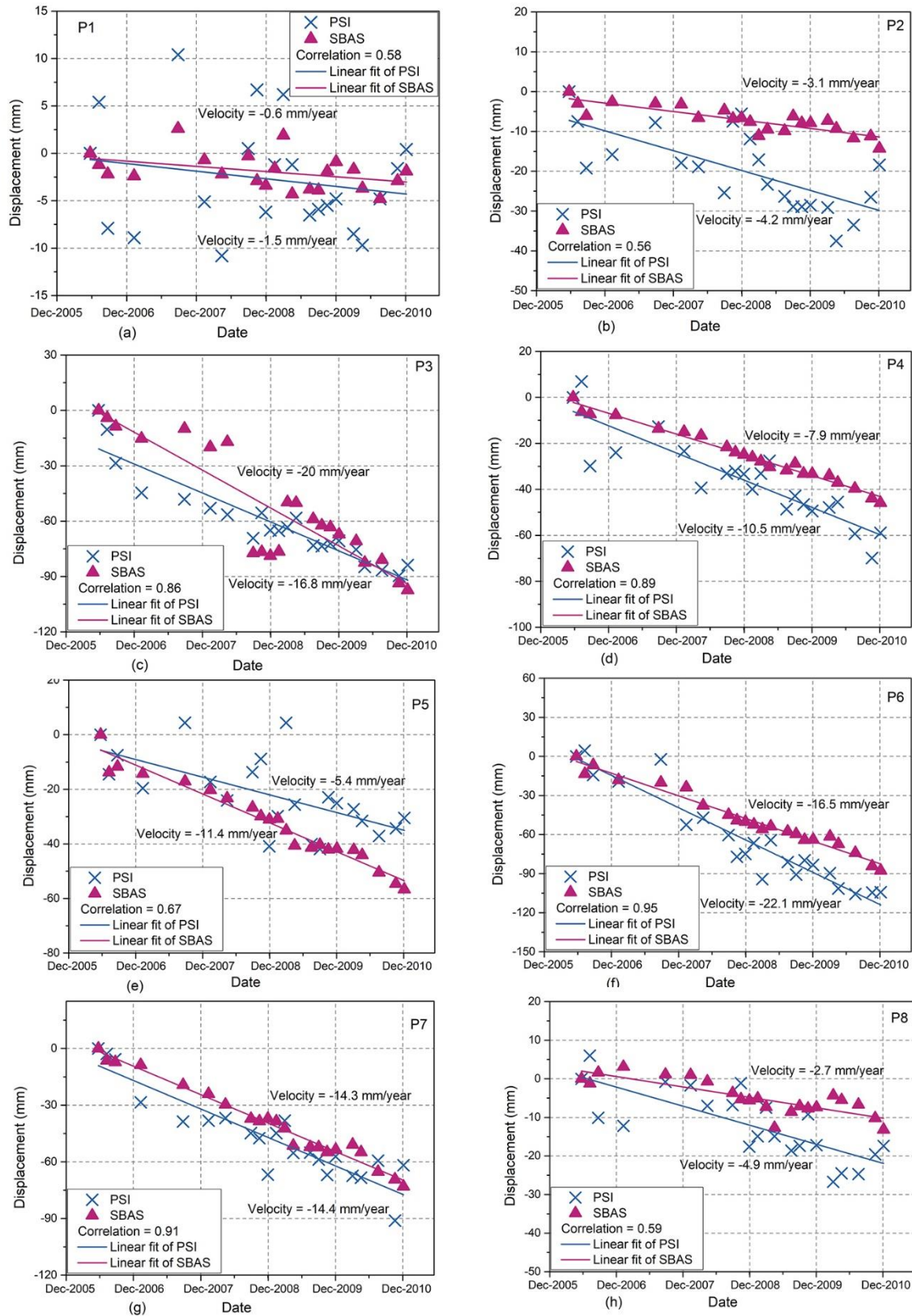


**Figure 4.8** Time-series LOS displacement plots of the PSI and SBAS measurements (a–h) for points P1 to P8, which are indicated as red points in **Figure 4.6a** and **4.6b**, respectively.

#### 4.4.3. Time-Series Analysis of the PALSAR-2 Data from December 2014 to November 2017

The mean velocity (mm/year) maps of the displacements for the period from December 2014 to November 2017 are shown in **Figure 4.9**. The same color cycle from green to purple was used for the result. In the study area of over 690,336 pixels, 76,500 measurement points were obtained by the SBAS method. The histogram of the SBAS-derived displacement velocity for the study area is shown in **Figure 4.10**. The average displacement rate and the standard deviation are  $-0.5$  mm/year and  $1.9$  mm/year, which are lower than those obtained with the ERS-1/-2 and PALSAR data. In general, the PALSAR-2 results show that approximately 85% of the PS points indicate displacement rates between  $-3$  mm/year and  $1$  mm/year (**Figure 4.10**). To show the variations in the LOS displacement velocities at different locations over the three observation periods, six profiles across several locations in Urayasu City were selected (**Figure 4.9**). We can see from **Figure 4.11** that these selected profiles show different displacement dispersion patterns, such as profiles P1–P1' and P5–P5' which show a dispersion of approximately  $-0.5$  mm/year to  $-2.6$  mm/year. Along profile P4–P4', the subsidence rate increased from  $0.1$  to  $21$  mm/year within the distance of  $0.6$  km. The profiles in **Figure 4.11**(b, c, d and f) reveal that the PALSAR-estimated subsidence rate has a larger value than those from the ERS-1/-2 and PALSAR-2. Contrary to the ERS-1/-2 and PALSAR-estimated displacement velocity, the PALSAR-2 results show an uplift within the distance of  $300$  to  $900$  m in the profile P1–P1' across the Moto-Machi area (**Figure 4.11a**). Moreover, both PALSAR and PALSAR-2 estimated displacement rates show a significantly decrease along P4–P4' (**Figure 4.11d**).

During the PALSAR-2 monitoring period, because of the high spatial resolution and shorter revisiting time compared to the ERS-1/-2 and PALSAR data, a subsidence estimation with better spatial coverage and precision was achieved. **Figure 4.9** shows that the three areas that have subsided during the previous monitoring periods have also showed land subsidence in this PALSAR-2 monitoring period (i.e., the border areas between Naka-Machi and Shin-Machi; the areas close to the levee of Hinode and Akemi (D); the Maihama area (A)). This may further imply that these areas were experiencing continuous subsidence during the entire monitoring period. Considering the existence of non-linear subsidence, the actual subsidence may not be a linear motion overtime, and the results by PSI and SBAS simply reflect the subsidence phenomena. However, the spatial extent and the magnitude of subsidence over Urayasu City is shrinking. The Moto-Machi area is in a relatively stable ground condition over the whole monitoring period, and the areas close to the borders of Moto-Machi and Naka-Machi began to stabilize over time. A

further detailed discussion about the evolutions and the causes of land subsidence in Urayasu City are given in section 5.4.

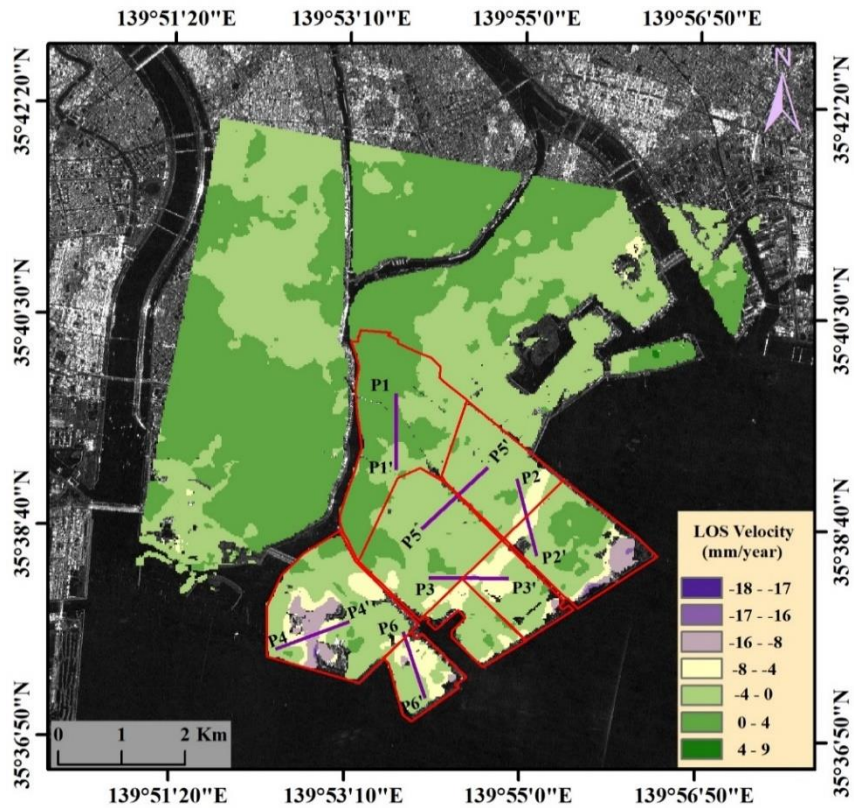


**Figure 4.9** Mean LOS displacement velocity in Urayasu City from 2014 to 2017 for the PALSAR-2 data. The background image is a PALSAR-2 intensity image acquired on 4 December 2014. P1–P1’ to P6–P6’ are the selected profiles to show the displacement velocities at different sites.

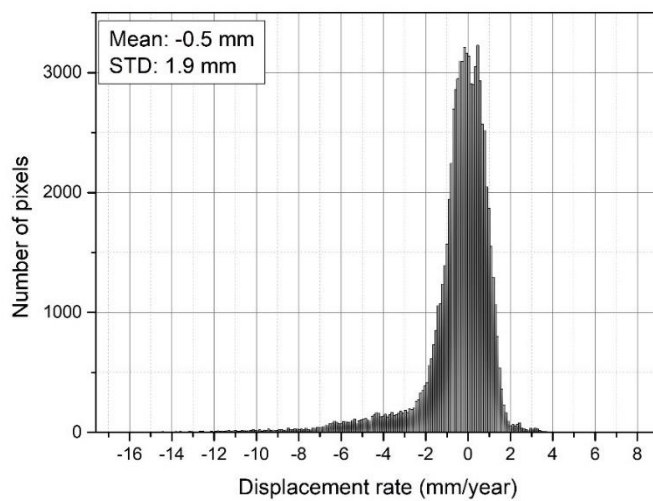


**Figure 4.10.** The corresponding histogram of the SBAS measurements from the PALSAR-2 data

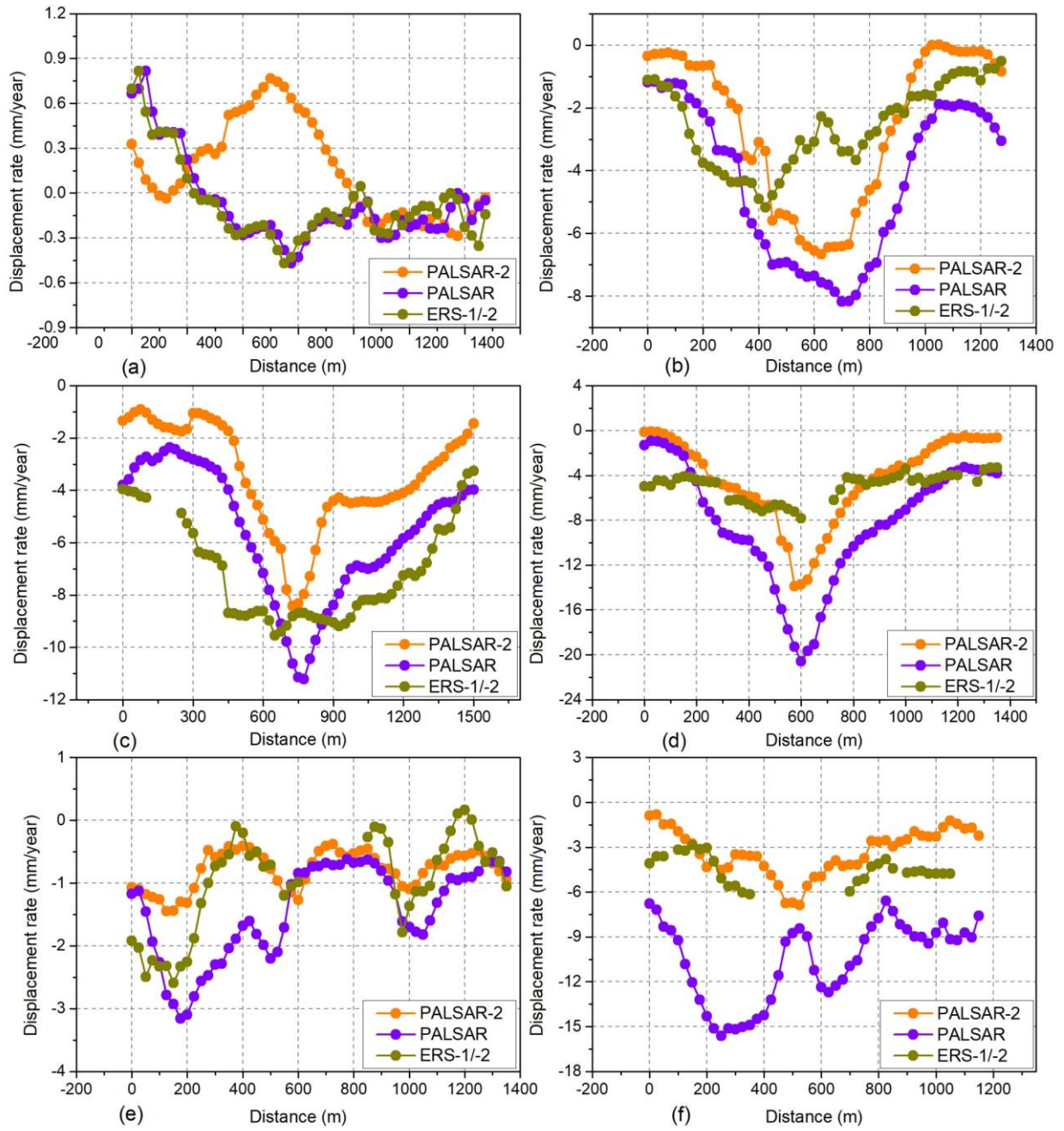


**Figure 4.11.** Mean LOS displacement velocities for the three observation periods (a–f) along the six profiles whose positions are indicated as purple lines in **Figure 4.9**.

## 4.5. Discussion

#### 4.5.1. Comparison of the InSAR-Derived Results with the Leveling Data

To assess the accuracy of the InSAR-derived results over the three observation periods, a quantitative comparison of the time-series displacements with the leveling survey data provided by the Chiba Prefecture at 22 measurement points was performed. To locate each leveling point, we referenced the online version of the Chiba information map and the illustration figures of each leveling point provided (Chiba Prefecture, 2018). For the InSAR measurement points, especially those in incoherent areas, the pixels that lay within 100 m of the corresponding leveling points were assigned, and the average velocity of these pixels was calculated. We selected the leveling data in the same overlapping periods as the three InSAR measurement periods. We assumed the horizontal deformation was negligible, and the LOS displacement velocity was converted into the vertical displacement velocity by dividing the cosine of the sensor incidence angle (Pepe and Calò, 2017).

**Figure 4.12** shows the spatial distribution of the leveling points and the comparison between the leveling and InSAR-derived linear subsidence rate. Note that the number of leveling points are different among the different InSAR observation periods; 17 leveling points were used for the comparison of the ERS-1/-2 and PALSAR observation periods, while 21 leveling points were used for the PALSAR-2 observation period, which is due to five new leveling points being established after the 2011 Tohoku Earthquake and the leveling point U-12A being missing in 2016. We also used different plot scales (20 mm/year vs 12 mm/year) and (2/4 mm vs 1/2 mm for error lines), due to the smaller errors shown in PALSAR data using the SBAS method (Figure 4.12d). The comparison results show that the results from the ERS-1/-2 data using the SBAS method have the largest root mean square errors (RMSEs) of 4.4 mm/year, while the results from PALSAR and PALSAR-2 data using the SBAS method have the smallest RMSEs of 0.9 and 2.2 mm/year, respectively. For the ERS-1/-2 and PALSAR data, more than 12 out of the 17 measurement points showed a residual value of less than 4 mm/year (**Figure 4.12a–d**); for the PALSAR-2 data, and 14 out of the 21 measurement points showed a residual value of less than 2 mm/year (Figure 4.12e). As shown in **Figure 4.12a, 4.12b** and **4.12e**, the results from the ERS-1/-2 and PALSAR-2 data using the PSI and SBAS method showed the largest discrepancies at several leveling points. This may have been caused by the low coherence of ERS-1/-2 datasets and the contribution of phase noise. The fewer PALSAR-2 image pairs and the sudden elevation changes in the ground, i.e., the leveling point U-17 subsided by the influence of construction work during 2015–2016 (Chiba Prefecture, 2017a), may also affect the comparison result. Nevertheless, according to these

comparisons, the InSAR-derived results agree relatively well with the result of the leveling measurements and suggest the reliability of the InSAR-measured subsidence rate.

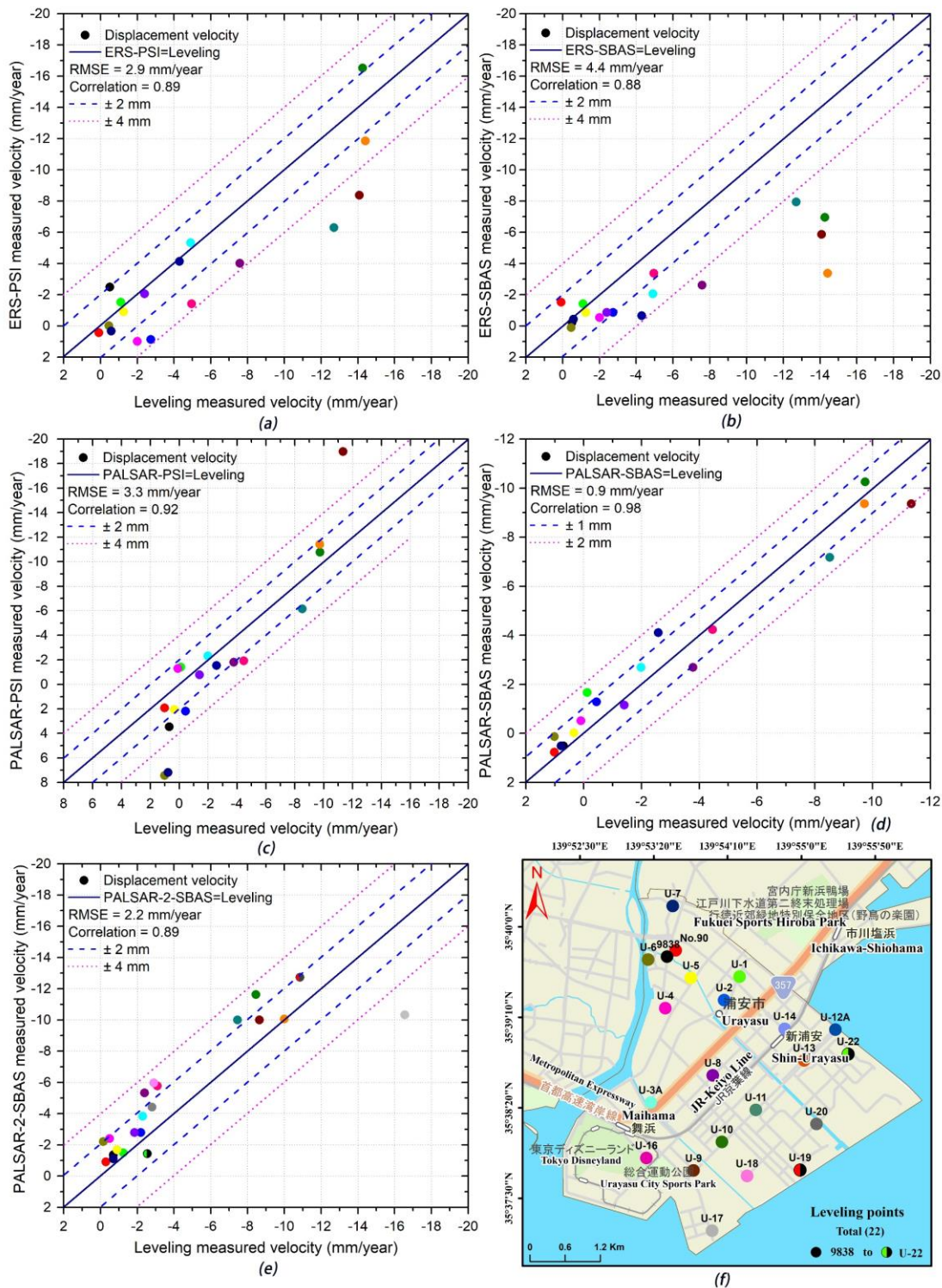


**Figure 4.12.** Comparison between InSAR-derived linear subsidence velocity and leveling measured linear subsidence velocity during the three InSAR observation periods: (a) and (b) ERS-

1/-2 derived linear subsidence rate (May 1993 to February 2006) and leveling-derived linear subsidence rate (January 1993 to January 2006); (c) and (d) PALSAR-derived linear subsidence rate (June 2006 to December 2010) and leveling-derived linear subsidence rate (January 2006 to January 2011); (e) PALSAR-2-derived linear subsidence rate (December 2014 to November 2017) and leveling-derived linear subsidence rate (January 2015 to January 2017); and (f) spatial distribution of leveling points in Urayasu City.

#### **4.5.2. Spatial and Temporal Patterns of Land Subsidence**

To further reveal the land subsidence patterns in different districts over the three observation periods, we generated the spatial distribution map of difference of land subsidence rates (**Figure 4.13**) using the ArcGIS 10.3 (Esri, Redlands, California, USA) spatial analyst tool. As the incidence angles of those sensors are different, before comparison, the LOS displacement velocity was converted into the vertical displacement velocity by dividing the cosine of the sensor incidence angle (Pepe and Calò, 2017). It can be seen from Figure 4.13a that the areas in the central town (i.e., Maihama (A), Tekkadori, Benten, Imagawa (B) and Irifune (C)) and new town (i.e., Takasu (E), Minato (F) and Chidori (G)) show slight to moderate subsidence with a 2–13 mm/year rate during the ERS-1/-2 observation period. From Figure 4.13b, we can see that the subsidence rate in some of the districts of the central town (e.g., Benten, Tekkadori and Imagawa (B)) has decreased up to 12 mm/year; while the areas in the new town showed increasing subsidence up to 28 mm/year, especially in Hinode (D) and Chidori (G). The comparison of PALSAR-2 and PALSAR estimated subsidence rate show that, the previous subsiding areas were experiencing a reduced subsiding rate, except some localized subsidence in the new town (**Figure 4.13c**). The comparison of PALSAR-2 and ERS-1/-2 estimated subsidence rate show that, the subsidence in both of the central town and new town has significantly decreased, except for areas in Maihama (A), Irifune (C), Hinode and Akemi (D) (**Figure 4.13d**). In general, most of those areas in the central town are residential and commercial amusement land, while the new town are parks and industrial land. The subsidence in parks can only be caused by the natural soil consolidation, while in the residential, commercial and industrial areas, the subsidence may be caused from the integrated effect of numerous natural and anthropogenic processes.

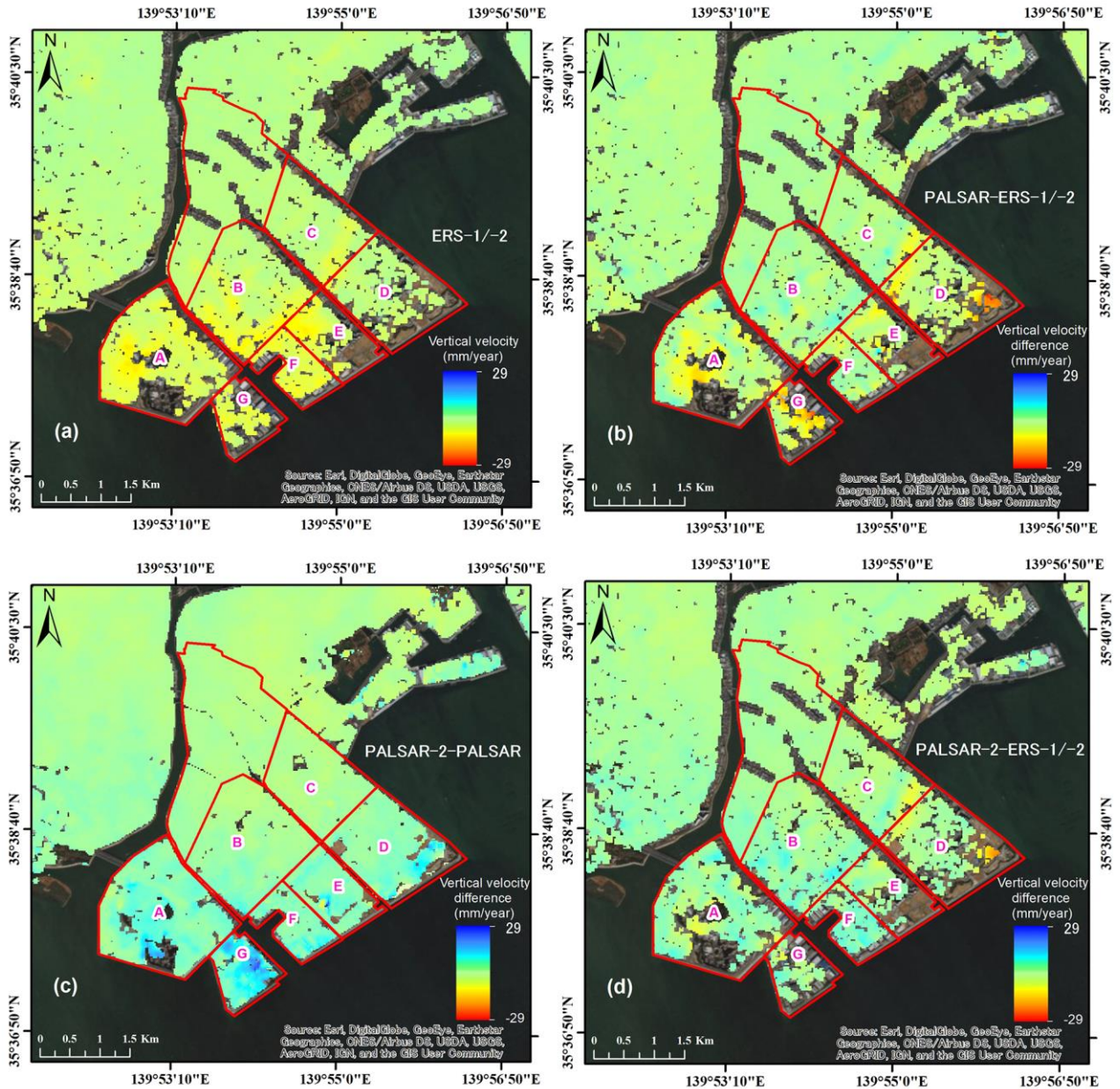


**Figure 4.13** The spatial distribution map of difference of land subsidence rates during the three observation periods: (a) ERS-1/-2 derived subsidence rate using the SBAS method; (b) difference between ERS-1/-2 and PALSAR derived subsidence rates (subtracting ERS-1/-2 from PALSAR); (c) difference between PALSAR and PALSAR-2 derived subsidence rates (subtracting PALSAR from PALSAR-2); (d) difference between ERS-1/-2 and PALSAR-2 derived subsidence rates (subtracting ERS-1/-2 from PALSAR-2).



### **4.5.3. The Use of Different SAR Sensors in Land Subsidence Monitoring**

The number of satellite data sources is currently increasing steadily. These datasets from the previous SAR sensors such as ESA archive (ERS-1/-2, ENVISAT) as well as the new generation of C, X and L-band SAR images provided by the RADARSAT-2, Sentinel-1A, ALOS-2, TerraSAR-X, Tandem-X and the COSMO-SkyMed constellation, etc. have enabled us to compute the time series of the occurred and on-going surface displacements from regional scale to individual buildings. In particular, the exploitation of the free and open access data archives collected by the Sentinel-1A system permit us to conduct continuous land deformation analysis over large areas.

In this study, three different SAR datasets, the ERS-1/-2, ALOS PALSAR and ALOS-2 PALSAR-2, were used to monitor the long-term land subsidence in Urayasu City. The C-band has a shorter wavelength and hence better displacement sensitivity, and the L-band has longer wavelength and lower frequency showing more extensive coverage over natural areas and less temporal decorrelation. The data acquired by these satellites cover long periods of time and enabled us to perform long-term deformation monitoring of the study area. However, those different sensors have different imaging parameters, e.g., spatial and temporal resolution, incidence angle, and wavelength, which show different characteristics in terms of their maximum detection gradient, degree of decorrelation, capability of noise rejection, etc. The different imaging parameters and the use of an uneven number of images among different sensors cause some difficulties in comparing their performance and the quality control of multi-sensor InSAR results. Moreover, the low resolution and the longer revisit time of ERS-1/-2 and PALSAR has prevented us from observing short-term land deformations caused by the anthropogenic activities. Furthermore, data gaps between the PALSAR and PALSAR-2 caused some difficulties in analyzing InSAR results.

### **4.5.4. Land Subsidence and Possible Causes**

The origin of land subsidence in coastal areas can be summarized into two categories: either caused by natural causes (e.g., natural compaction/consolidation of soil or tectonic movements, such as earthquakes) or anthropogenic activities (e.g., oil, gas and ground water exploitation). In some cases, the pattern of land subsidence might be even more complicated when it is caused by the combined effects of multiple factors at different scales. In Urayasu City, since most of the

areas are land-filled, the natural consolidation of soil is postulated to be the primary driver of land subsidence. To further analyze the relation between subsidence and soil geology, we compared the InSAR-derived subsidence areas with the geologic map showing the depth of the upper surface of the solid geological stratum in Urayasu City (**Figure 4.14a**) and found a remarkable spatial correlation between the geologic map of the soil properties and the subsiding areas. In most of the reclaimed zones, the upper layer of soil filled with hill sand and dredged sandy soil (FS) with a standard penetration test (SPT) N-value of 2–8; an alluvial sand layer (AS) with SPT N-value of 10–20 underlies the filled layer; a very soft alluvial clay (AC) is deposited under the AS layer with a low SPT N-value of 0–5; a diluvial (Pleistocene) dense sand layer (DS) with SPT N-value of 50 or greater is deposited below the AC layer (**Figure 4.14b**) (Yasuda *et al.*, 2012; Nigorikawa and Asaka, 2015). Along the line A–A', the thickness of AC layer increases significantly between the Naka-Machi and Shin-Machi area, and it continues towards the sea (**Figure 4.14b**). As the consolidation of soil occurs in soft clay deposits, the thick AC layers in Naka-Machi and Shin-Machi area are most probably responsible for the continuing subsidence in Urayasu City.

As shown in **Figure 4.14a**, the depth of the bottom of the alluvial layers increases from 20 m in Moto-Machi to about 40 m in Shin-Machi, with several narrow-buried valleys of up to 70 m in depth. The buried-valleys, which are about 60 m deep, exist directly below the Minato, Chidori, Tekkadori, Imagawa, Akemi and Irifune areas, causing complicated changes in the thickness of the soft ground in those areas, while the depth increases up to 80 m in Maihama where the largest subsidence occurred. This further suggests that the areas undergoing large subsidence correspond to those having thick layers of soft soil over a stiff basement. The Moto-Machi area, with soil deposits consisting of sandy soils with an alluvial origin, was quite stable over the observation period, while the Naka-Machi and Shin-Machi areas, with thick layers of fine-grained soft soil overlying a stiff basement, had significant land subsidence over the study period. However, considering the complexity of the land use and the anthropogenic activities in different districts of Urayasu City, the subsidence may not be solely caused by the natural consolidation, but also from the integrated effects of numerous natural and anthropogenic processes.

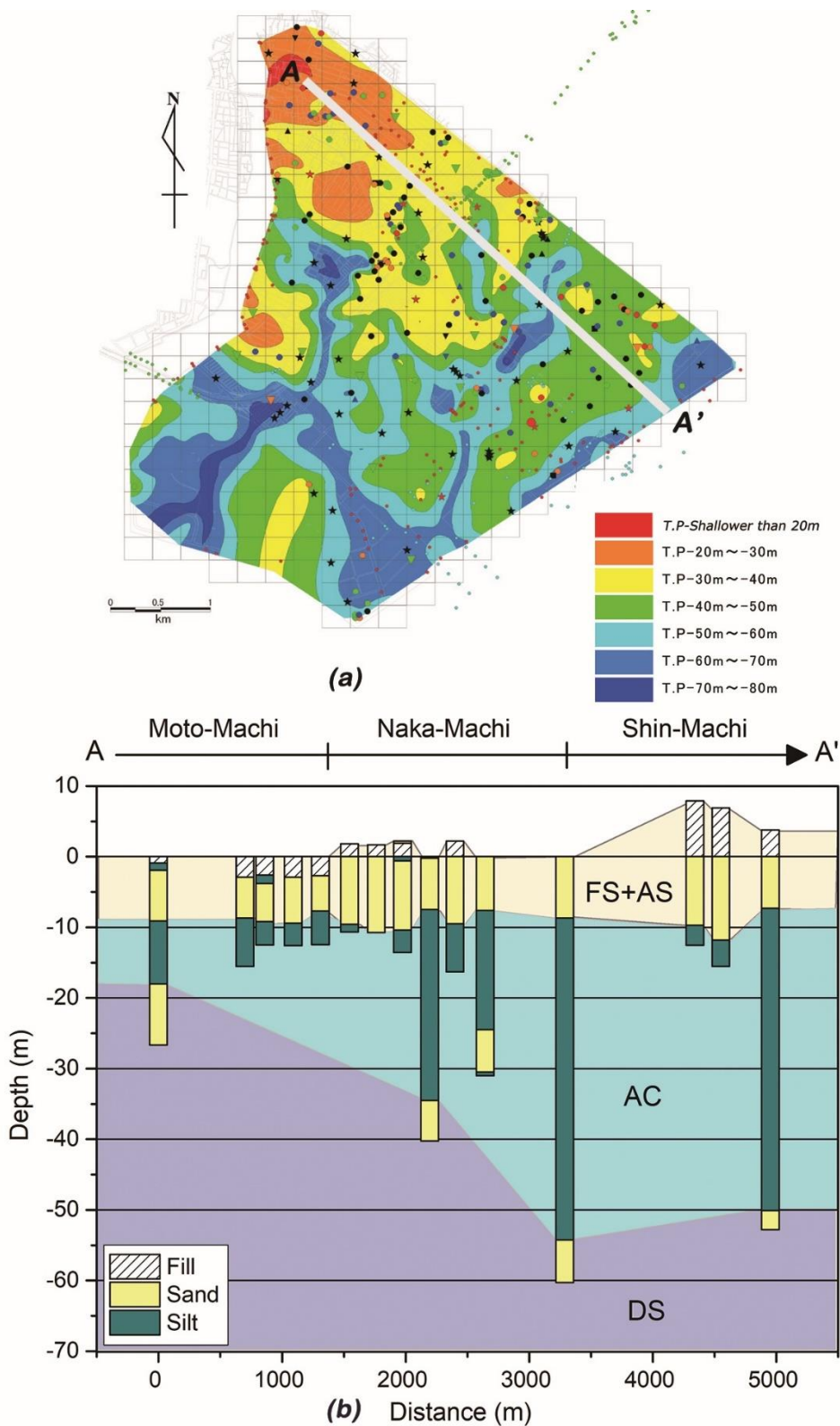


**Figure 4.14** Depth of the upper surface of the solid geological stratum (a) in Urayasu City (adapted from the public report by the technical committee of Urayasu City (*Regional disaster prevention project of Urayasu City - earthquake disaster*, 2011)). The points refer to the locations of borehole sites; (b) soil cross sections along the A–A' line. FS + AS refer to filled sandy soil

and alluvial sand layers, and AC and DS refer to the alluvial clay layer and diluvial dense sandy layer, respectively. The borehole investigation data were obtained from the Chiba Prefecture (Chiba Prefecture, 2016a).

The additional load of buildings and structures is also considered to be one of the causes of land subsidence in urban areas (Chen *et al.*, 2018). In Urayasu City, since the establishment of Urayasu town in 1909 in the old town (Moto-Machi)—a naturally formed Holocene lowland—the natural soil consolidation might be gradually reduced and stopped. Besides this, the density of buildings in the old town are lower than the central town. Many houses, commercial buildings and public facilities were built in the central town during the first phase of the project, ending in 1975. Meanwhile, many high-rise buildings, universities, hotels and storehouses were built in the new town during the second phase of the project, ending in 1980 (Tokimatsu *et al.*, 2012). The additional load during and after the building construction, especially the high-rise buildings, could transfer a high loading to the ground and may eventually lead to substantial land subsidence. However, these buildings use a pile foundation to satisfy bearing capacity and deformation and may not show significant subsidence while the surrounding areas are subsiding. **Figure 4.15** shows the InSAR-derived subsidence velocity (2006–2010) and the locations of high-rise buildings. Most of those buildings show stability, whereas their surroundings show land subsidence. However, further investigations are expected to determine the relationship between land subsidence and the building density/high rise buildings.

The Maihama district in the central town, where Tokyo Disneyland is located, showed significant subsidence throughout the whole InSAR observation period. However, in this area, the pattern of land subsidence may be even more complicated due to the continuous construction and renovation/redevelopment of the fantasy-land and other anthropogenic activities. The SAR images with a low resolution and longer revisiting time, and the linear inversion model used in the InSAR processing, may hinder the effective monitoring of short-term movements such as those induced by human activities and may cause some biased results. Therefore, more high-resolution SAR data with a short revisiting time and further investigation is required to understand the intricacies of the relationship between land subsidence, natural consolidation and load of buildings.

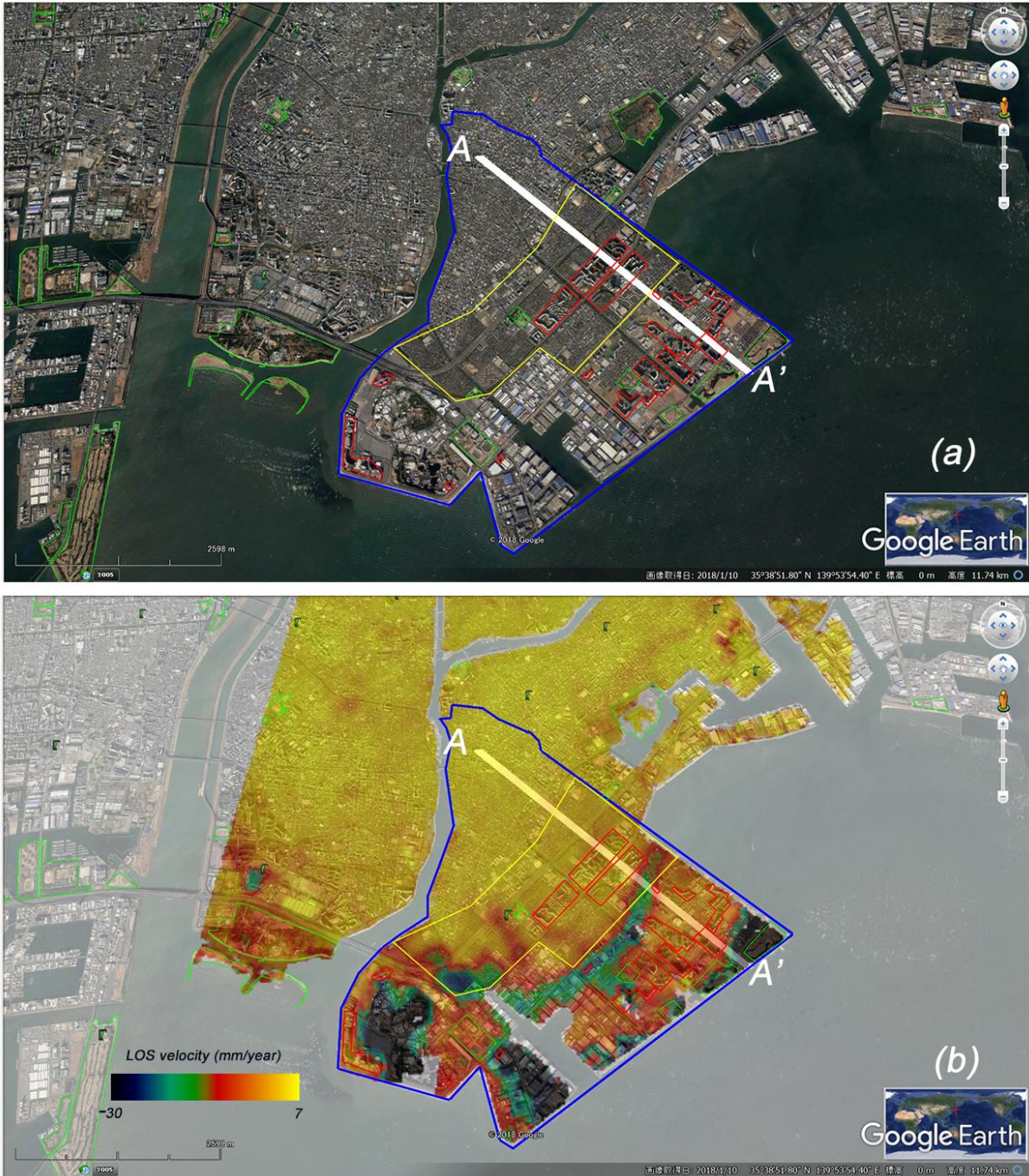


**Figure 4.15** Subsidence rate map (2006–2010) generated with ALOS PALSAR data overlaid on a Google Earth image. The green polygons indicate the park area, red polygons indicate the location of high-rise buildings, the yellow polygon shows the highly populated residential area. The blue polygon indicates the border of Urayasu City and corresponds to the location of **Figure 4.14a**, and the A–A’ line corresponds to the soil cross-section in **Figure 4.14a** and **4.14b**.

Ground water exploitation is one of the major causes of land subsidence in many coastal cities, such as in Jakarta (Abidin *et al.*, 2011), Bangkok (Aobpaet *et al.*, 2013) and Shanghai (Chai *et al.*, 2004). Nevertheless, this may not be the cause of land subsidence in Urayasu City; this is because the ground water exploitation was gradually reduced and stopped in 1993 (Chiba Prefecture, 2017b), and the city receives water from a water purification plant which uses the main water sources of the Tone river and Edogawa river (Chiba Prefecture, 2016b). Moreover, since April 1992, Chiba Prefecture has been implementing restriction rules on groundwater use for the highly susceptible areas of land subsidence, including Urayasu City (Chiba prefecture, 2015). Thus, the ground water exploitation has insignificant impacts on land subsidence in Urayasu City.

As an earthquake-prone country, earthquakes happen frequently in Japan. Earthquakes have significant influences on coastal areas, especially on reclaimed land. In the 2011 Tohoku earthquake, houses and infrastructures were severely damaged due to soil liquefaction in Urayasu City (Tokimatsu *et al.*, 2012). In addition, long-term ground settlement was also observed after the earthquake, and the degree of subsidence was different in areas where reclaimed soils were improved or not (Nigorikawa and Asaka, 2015). In the areas where the soil was not improved, the subsidence may have been accelerated by the earthquake. The InSAR observation results derived from the PALSAR-2 data showed significant continuing land subsidence near the levee areas (mostly parks and vacant lands), which may have been accelerated by the effects of the earthquake. However, most areas showed a decrease of land subsidence, this may be related to the fact that the PALSAR-2 observations (December 2014 to November 2017) were collected almost 4 years after the Tohoku earthquake, and considering the soil aging effect and soil improvement, the land settlement in most of those areas caused by the natural soil consolidation and the earthquake might gradually decrease. It is worth mentioning that after the earthquake, the Urayasu government started to test several countermeasure methods, such as lowering the ground water level and grid wall soil improvement. Finally, Urayasu has adopted the grid wall soil improvements as a countermeasure to prevent future risks (Ishii *et al.*, 2017). This project may also have played a positive role in alleviating the land subsidence in Urayasu City.

## **4.6. Conclusion**

In this study, to monitor the long-term spatial patterns of land subsidence in Urayasu City, we used three sets of different SAR data and advanced InSAR techniques. The obtained InSAR

results during the three observation periods from 1993–2010 and 2014 to 2017 show continuing subsidence occurring in several reclaimed areas of Urayasu City. The maximum subsidence rate from 1993 to 2006 was approximately 27 mm/year, from 2006 to 2010 it was 30 mm/year, and from 2014 to 2017 it was about 18 mm/year. The results were verified by comparing them with the leveling survey data. The comparison shows that the obtained InSAR results agree well with the leveling measurements, with a correlation value of over 0.8. The natural consolidation of soil in the reclaimed areas can be considered as a primary driver of land subsidence in Urayasu City, while the integrated effects of numerous natural and anthropogenic processes are also not negligible. Considering the soil aging effect, water-use restriction rules and soil improvement work performed by the government and land owners might also have played a positive role in alleviating the land subsidence and related disasters. However, further investigation is required to understand the intricacies of the relationship between the land subsidence and anthropogenic activities. The outcome of this research further proves the suitability and effectiveness of InSAR measurements in the land subsidence monitoring of coastal urban areas.

## Chapter 5

# Earthquake-induced landslide mapping using PALSAR-2 data

### 5.1. Introduction

Earthquake is one of the most dangerous natural disaster events around the world, and most of the earthquakes are occurring in mountain areas. In general, the moderate to a severe earthquake could trigger landslides in the mountainous region (Roback *et al.*, 2018). These landslides may cause injuries and loss of human life, damage to infrastructures, and lead to enormous economic losses. Therefore, quickly identifying and mapping of the landslide has great importance in emergency response and restoration activities after landslides (Plank, 2014).

Nowadays, owing to its capability of wide-area observation, relatively low cost and rapid advances in remote sensing satellite observations have enabled us to effectively detect, and monitor landslides at an individual and regional scale. Optical (e.g., QuickBird, GeoEye-1, and WorldView-2), and synthetic aperture radar (SAR) data (e.g., TerraSAR -X, and COSMO-SkyMed) are the commonly used Satellite sensors for detecting and analyzing slow to a rapid moving landslides (Masumi *et al.*, 2013; Tofani *et al.*, 2013; Casagli *et al.*, 2017). When cloud-free optical imagery is unavailable, and the coverage of ground-based observations are limited, the SAR data can be an optimal solution owing to its capability of day-and-night and all-weather imaging (Plank *et al.*, 2016; Burrows *et al.*, 2019). The number of SAR sensor is currently increasing steadily. These datasets from the previous SAR sensors (e.g., ERS-1/-2, ENVISAT and PALSAR) and the new generation of C, X and L-band SAR images provided by the RADARSAT-2, Sentinel-1A, ALOS-2, TerraSAR-X, Tandem-X and the COSMO-SkyMed constellation, etc. have enabled us to compute the historical and current landslides with high precision (Strozzi *et al.*, 2013; Bardi *et al.*, 2014; Dong *et al.*, 2018).

On 6 September 2018, a powerful earthquake of moment magnitude Mw 6.7 occurred off the Iburi Subprefecture in southern Hokkaido, Japan. The earthquake took place just one day after the typhoon Jebi (No. 21 in Japan) left torrential rains in the region (Yamagishi and Yamazaki, 2018).



After the earthquake, up to 6000 landslides occurred near the epicenter-Atsuma town, due to the heavy rains soaked subsurface deposits of volcanic soil in the region, turning them into a geologic grease layer (Normile, 2018; Yamagishi and Yamazaki, 2018). As an emergency response coordination, the Geospatial Information Authority of Japan (GSI) took aerial photographs on the same day and after the Earthquake (6, 8 and 11 September 2018) (GSI, 2018a). Several days later, on 12 September 2018, the GSI mapped the landslide area using those aerial photographs and published their results on their website (GSI, 2018a). Shao et al. produced a landslide susceptibility map of the area by applying the logistic regression (LR) and the support vector machine (SVM) to the high-resolution Planet images (optical) (Shao *et al.*, 2019).

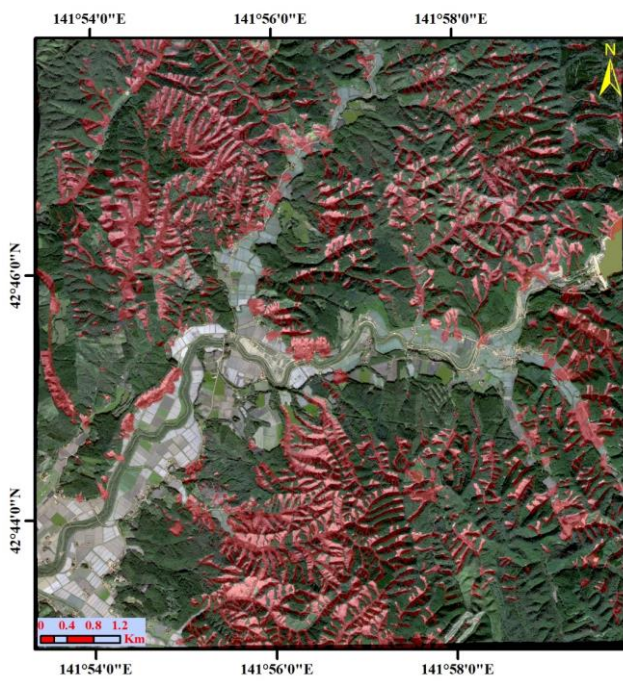
In this study, we present a rule-based method to identify and map the Earthquake-induced landslide in Hokkaido, taking advantage of ALOS-2 PALSAR-2 SAR images taken before and after the event. Moreover, the high-resolution optical image- WorldView-2 and Geo-Eye-1, truth data (GSI, 2018a), and field survey data were used for reference and validation purpose.

## 5.2. Study area

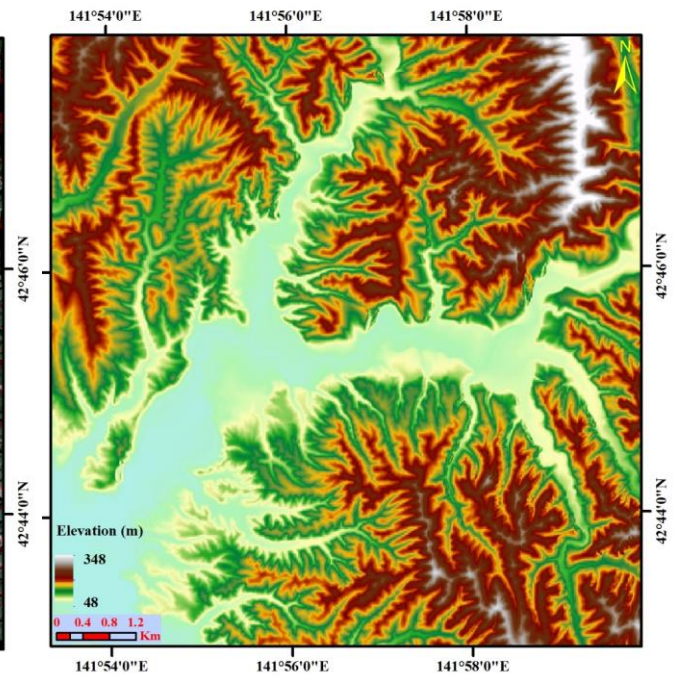
An earthquake with magnitude off Mw6.7 struck the Iburi Subprefecture in southern Hokkaido, Japan. The epicenter of the 2018 Hokkaido Eastern Iburi earthquake is at 42.72° North, and 142.0° East, and the maximum intensity of 7 registered at Atsuma town. After considering the availability of ALOS-2 PALSAR-2 data, its coverage and reference optical data, we chose an area near the Atsuma town spanning from 42.43°North to 42.48°North of latitude and from 141.52.5° East to 141.60° East of longitude as a study area (**Figure 5.1a**). From **Figure 5.1c**, we can see that the elevation of the study area is range from 48-348m, and most landslides are occurred between high to moderate elevations up to 348m (GSI, 2018b). The **Figure 5.2** shows the land use land cover (LULC) map of the study area, the deciduous broadleaf forest (DBF), deciduous needleleaf forest (DNF), rice paddy and grassland are the dominant land use classes.



a



b



c

**Figure 5.1** The map of the study area, Hokkaido, Japan. (a) the geographic location of the study area; (b) identified landslide areas by the GSI, Japan (GSI, 2018a); (c) the topography of the study area (GSI, 2018b).

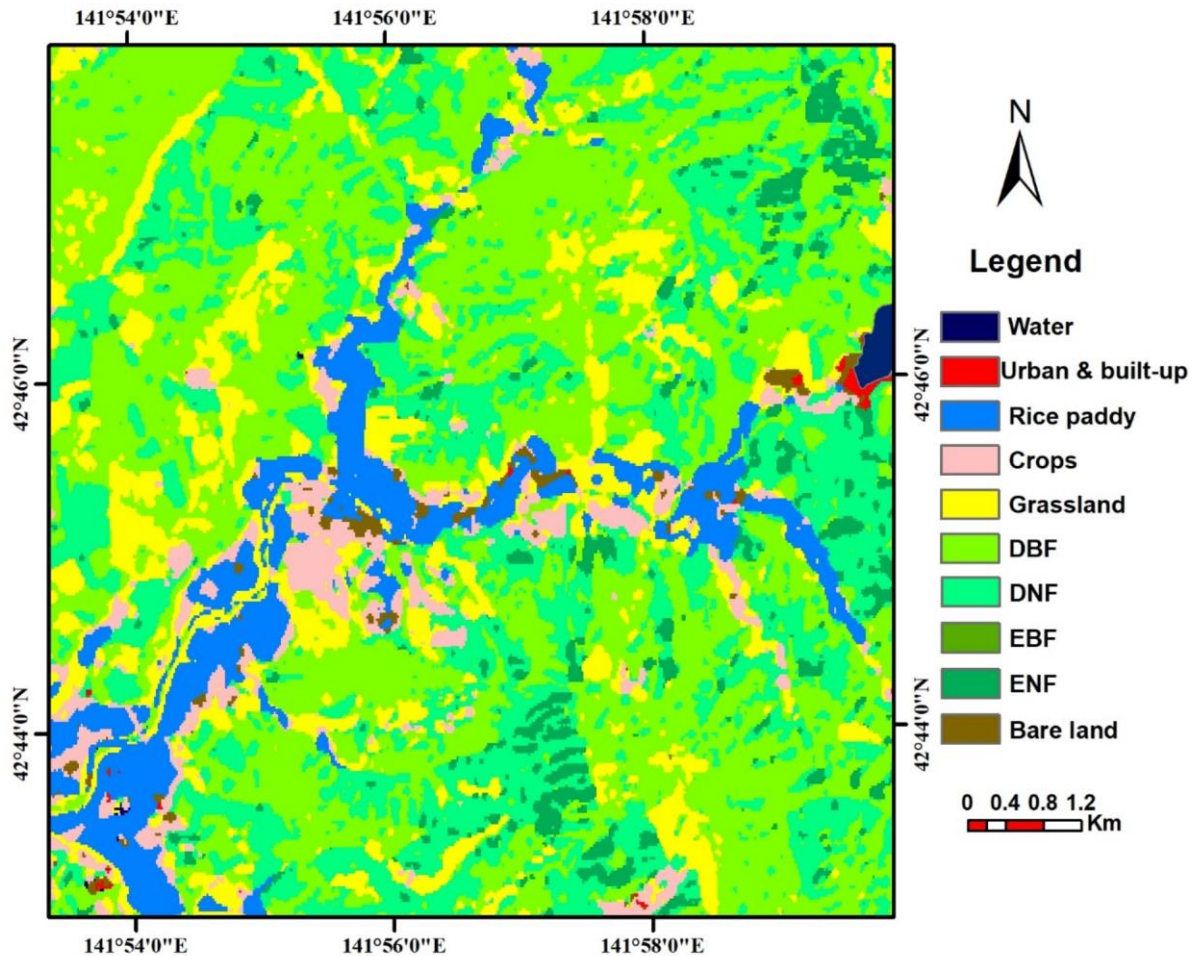


**Figure 5.2** The Land Use and Land Cover Map of the study area. The data provided by JAXA and available at [https://www.eorc.jaxa.jp/ALOS/en/lulc/lulc\\_index.htm](https://www.eorc.jaxa.jp/ALOS/en/lulc/lulc_index.htm)

### 5.3. Data sets and preprocessing

#### 5.3.1. SAR and optical satellite data

In this study, the L-band PALSAR-2 satellite data sets covering the region of interest (**Figure 5.1**) were provided by the Japan Aerospace Exploration Agency (JAXA). The interferometric coherence was computed from single look complex (SLC) PALSAR-2 data taken on 14 June 2018, 23 August 2018, and 06 September 2018 (Descending), and on 09 August 2018, 23 August 2018, and 06 September 2018 (Ascending). Both Descending and Ascending data is in Stripmap (SM1) mode and HH polarization with a high resolution of 3 m. A 10-m high-resolution digital elevation model (DEM) provided by the GSI was used to co-register the InSAR pairs (GSI, 2018b).

We also collected two high-resolution optical images, WorldView-2 and GeoEye-1 acquired on 24 October 2017 and 20 October 2018 with a resolution of 2m (**Figure 5.3**). The optical image was used for the visual comparison of the landslide classification. To remove the effects, such as the image perspective (tilt) and relief (terrain) effect, we orthorectified the image using the same 10-m DEM data used for the SAR data.

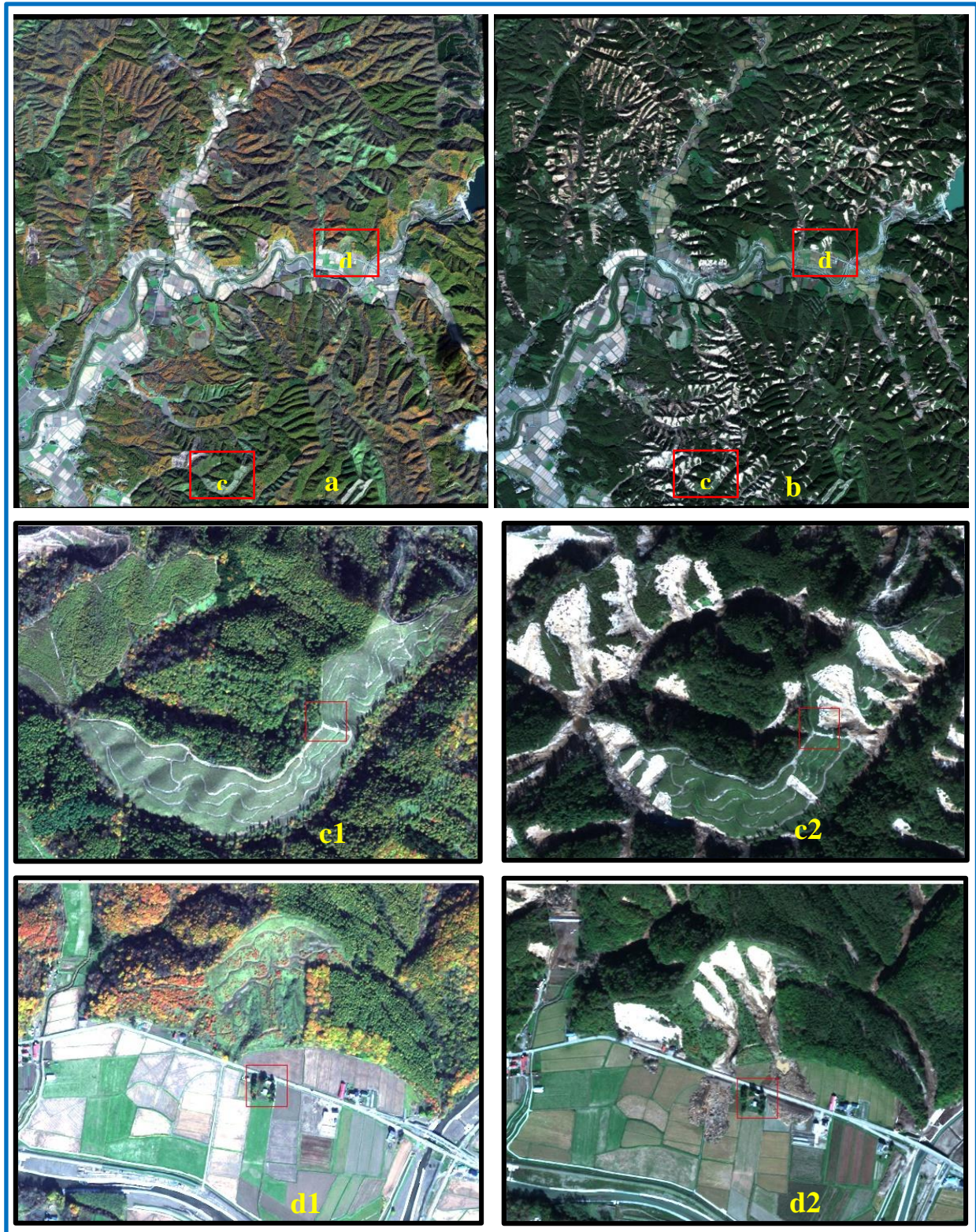


**Figure 5.3** The orthorectified image of WorldView-2 (left)-24 October 2017(a) and GeoEye-1(right) 20 October 2018 (b); c1, d1 and c2, b2 are the enlarged view of a and b, respectively.

### 5.3.2. Truth data and field survey

In this study, we used the landslide distribution map produced by the GSI, Japan (GSI, 2018a) as a truth data. The landslide was visually interpreted using high-resolution aerial photos taken on September 6, 8 and 11, 2018 (**Figure 5.1 b**). The data is available on the website of GSI, Japan: <http://www.gsi.go.jp/BOUSAI/H30-hokkaidoiburi-east-earthquake-index.html#1>.

After four weeks off the earthquake, a field survey was carried out on October 3~4, 2018 around the Atsuma town, Abira town and Mukawa town. **Figure 5.4** shows the field survey route and some pictures taken during the survey.

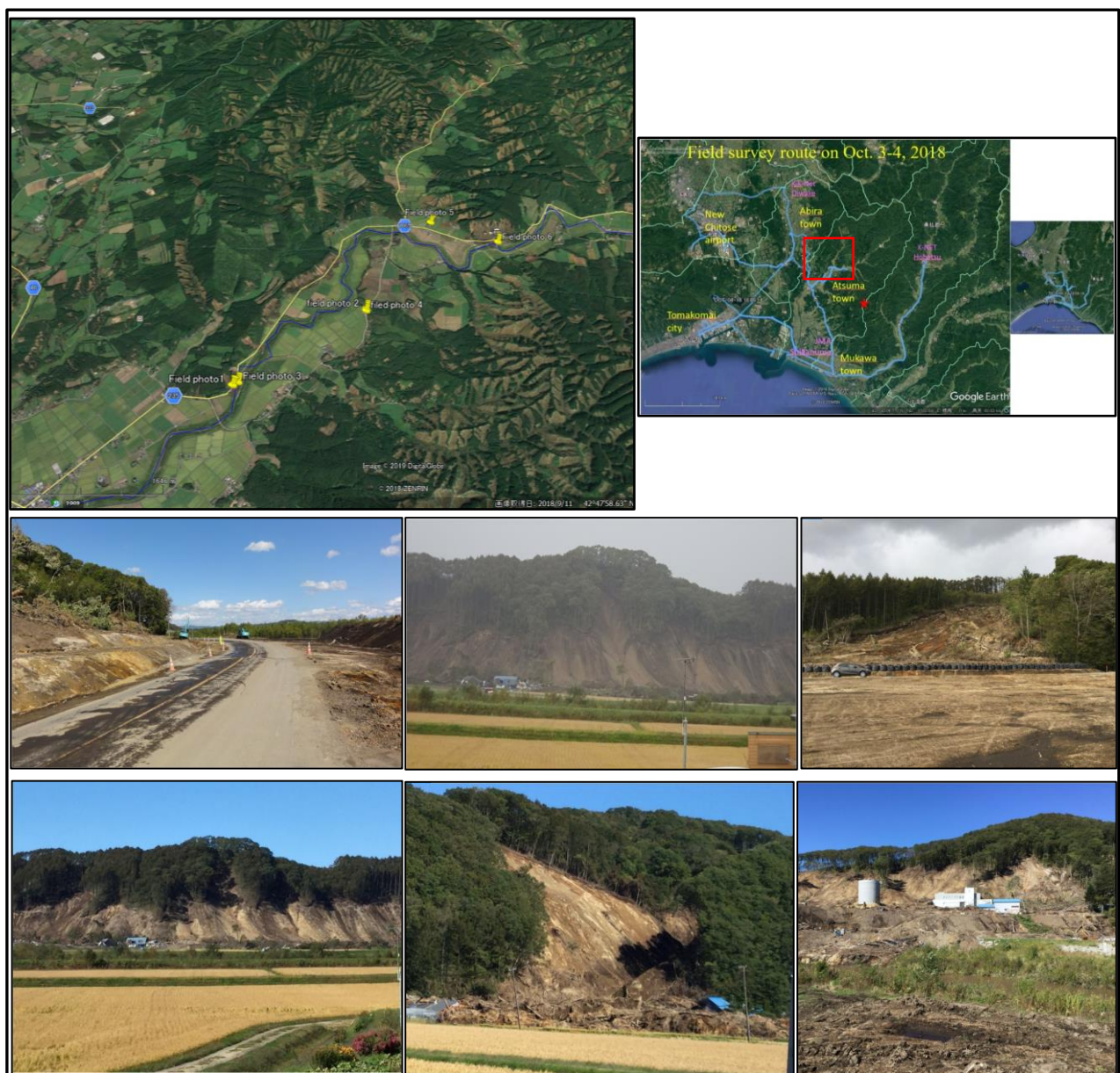


**Figure 5.4** The field survey route and some of the collected photographs near the Atsuma town.

## 5.4. Methodology

### 5.4.1. Synthetic Aperture Radar: Interferometry and coherence

A Radar interferogram can be calculated using two SAR images acquired by the same satellite over the same region at different times (Bamler and Hartl, 1998). Generally, an interferometric map (e.g., **Figure 5.5 b** and **d**) shows the difference in phase between two SAR images. The sequence of color fringes in the interferogram can be used to determine the change in distance between the satellite and the object (close or away). For ALOS-2 PALSAR-2, each color fringe shows a phase change of two images and equal to a half wavelength of PALSAR-2 (11.6 cm).

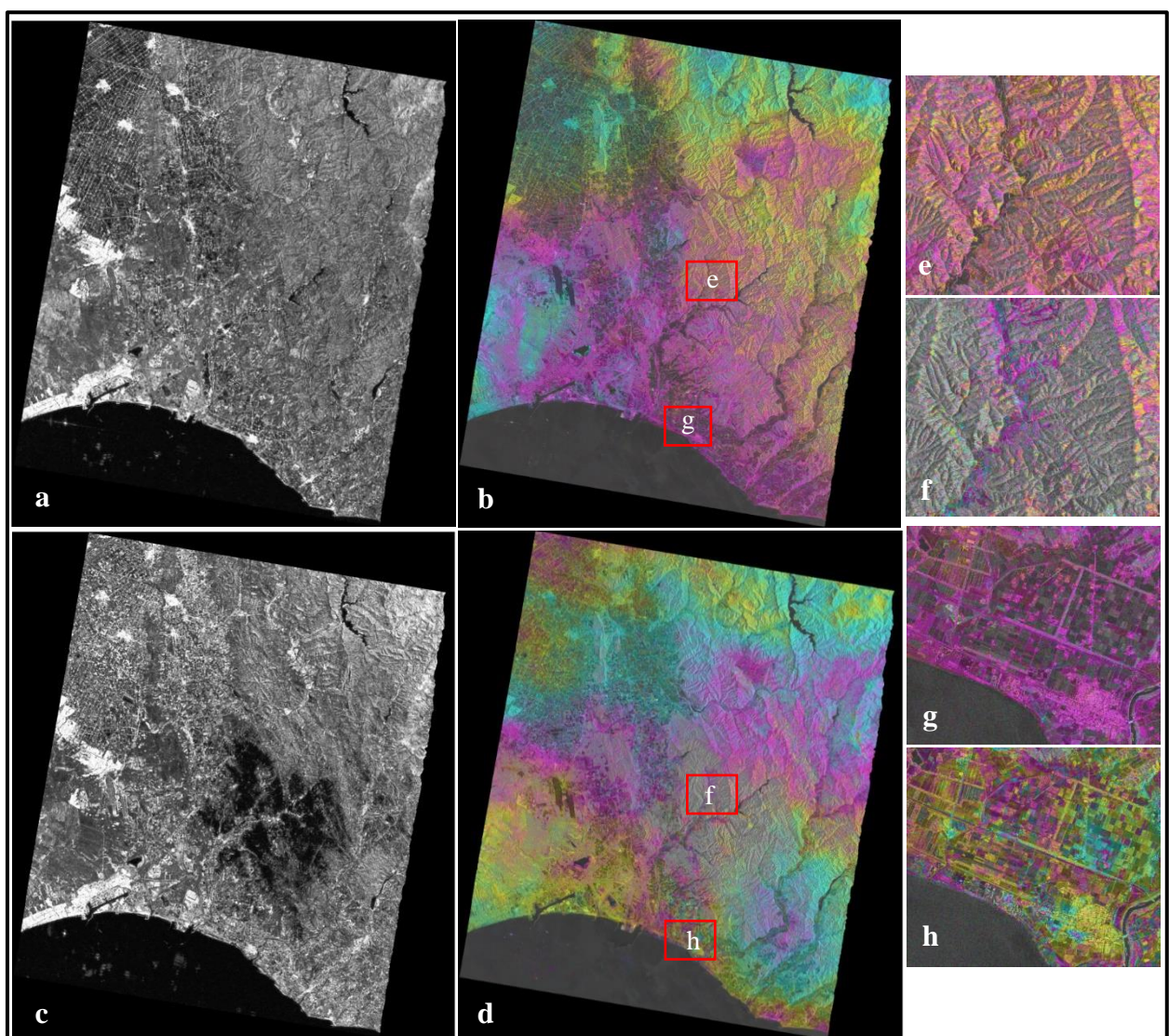


**Figure 5.5.** ALOS-2 interferogram from pre-and co-event image pairs (Descending). (a) and (b) are the coherence and interferogram of pre-event image pairs (20180823-20180614); (c) and (d)

are the coherence and interferogram of co-event image pairs (20180823-20180906); (e-h) are the enlarged view of the pre- and co-event interferograms.

The coherence ( $\gamma$ ) is the interferometric correlation of complex signals between two SAR data, which can be calculated as:

$$\gamma = \frac{\sum C_1 C_2}{\sqrt{\sum |C_1|^2} \sqrt{\sum |C_2|^2}} \quad (1)$$

Where  $C$  is a complex number with phase ( $\phi$ ) and amplitude ( $A$ ) (Ferretti *et al.*, 2007). Coherence is a normalized metric, and the values range from 0 to 1. It can be a good indicator of the quality of the interferogram, and a high coherence value is associated with a ‘good quality’ interferogram. Furthermore, coherence is sensitive to changes to either the phase or amplitude of a pixel. Hence, ground surface change due to Earthquake, landslide or flooding, etc. will alter the scattering properties of each pixel of SAR images will result in low coherence (Zebker and Villasenor, 1992). As shown in **Figure 5.5** (c, d), the coherence was significantly decreased in the area where landslides occurred. Therefore, the SAR coherence was used as a starting point in this study.

#### 5.4.2. SAR coherence and intensity difference

SAR has the capability for obtaining both amplitude and phase backscattering echoes from the targets, the SAR products such as SAR amplitude and InSAR coherence are can be complementary to each other for landslide mapping in highly vegetated regions (Konishi and Suga, 2018). **Figure 5.6** shows both descending and ascending SAR coherence and intensity, and the corresponding landslide features on these images. The Interferometric coherence map for both ascending and descending PALSAR-2 data is generated by employing the SARscape® Modules (5.4) for ENVI (5.4) software. For the original descending PALSAR-2 data, the SLC image on August 23, 2018, was selected as a master image, June 14, 2018, and September 6, 2018, as a slave image, and generated two interferometric coherence image pairs. For the original ascending PALSAR-2 data, the SLC image on August 23, 2018, was selected as a master image, August 9, 2018, and September 6, 2018, as a slave image, and generated two interferometric coherence image pairs. Both descending and descending coherence images were multi-looked by a factor of eight in azimuth and seven in range, giving a pixel size of approximately 15 m. A multi-temporal ANLD filtering with a  $3 \times 3$ -pixel window was applied to the multi-looked coherence images and were geocoded in the WGS84 reference ellipsoid. For the descending and ascending intensity images, the same multi-look, co-registration, and filtering process were performed and geocoded





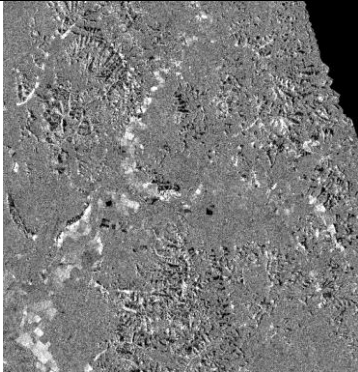
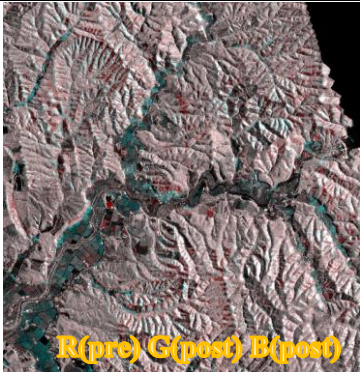
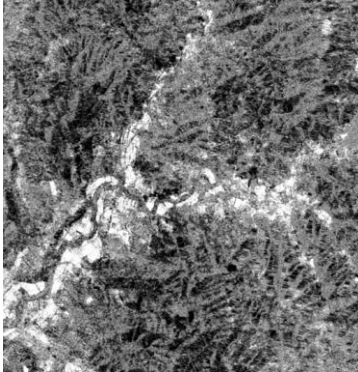
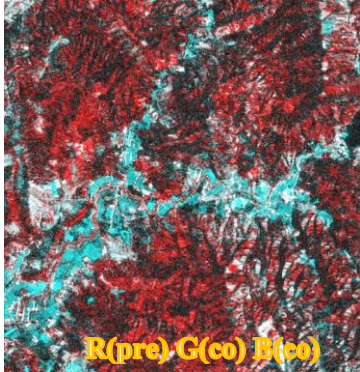
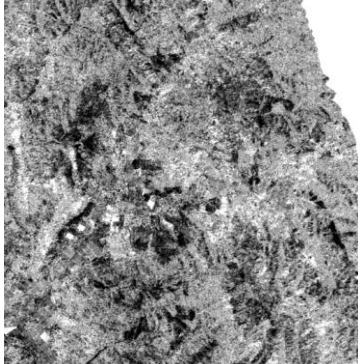
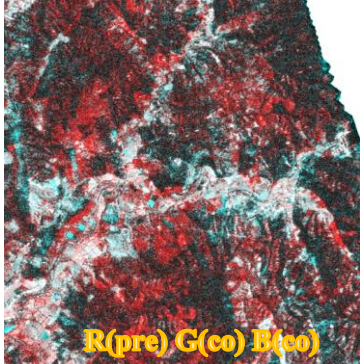
in the same reference ellipsoid. The geocoded intensity images were calibrated to normalized backscattering coefficients (sigma-naught) using the equation:

$$\sigma^0 = 10 \log_{10}\langle DN^2 \rangle + CF_1 \quad (2)$$

Where  $\sigma^0$  is the backscattering coefficient (Sigma naught) [unit: dB], DN: digital number of SAR amplitude images,  $CF_1$  is the calibration factor [- 83 dB].

Speckle noise reduction is a crucial step for SAR applications. For the final geocoded products, we applied the same Enhanced Lee filter with  $5 \times 5$  window size for both coherence and intensity images. And, calculated the difference between pre- and co-event coherence (**Figure 5.6**) and pre- and post-event intensity images (**Figure 5.6**).

The SAR amplitude and phase are sensitive to the earth's surface properties, such as changes in height and roughness and moisture content. As shown in **Figure 5.2**, almost 95% of the study area is covered by vegetation. Generally, when the landslide occurs, landslides replace the vegetated areas with bare soil or rock and alter the scattering properties of each pixel in SAR images spanning the landslide event, and leading to low temporal coherence (landslide pixels are expected to have low coherence.) (**Figure 5.6**). Therefore, interferometric coherence can be used to map landslides (Burrows *et al.*, 2019). However, interferometric coherence is affected by temporal and spatial baselines. Since the study area is heavily vegetated, the low coherence may also be caused by the seasonal change or moisture of the vegetation, which may lead to many false positives in the landslide classification. This is evident in **Figure 5.6** ascending coherence difference that the cropland and grassland areas are also showed low coherence as landslides. The SAR intensity is sensitive to the roughness and slope of the ground surface, and less affected by the temporal and spatial baselines. **Figure 5.6** shows the pre- and post-event intensity difference and color composite image. Generally, landslides will change the vegetation of the ground surface and topography, which alters the intensity of the backscattered wave. The removal of trees leads to the decrease in intensity images, and the accumulated debris leads to the increase in intensity (**Figure 5.6**). Therefore, the intensity difference could provide useful information for landslide identification (Konishi and Suga, 2018).

	Mode	Difference	Color composite (RGB)
Intensity	Descending		
	Ascending		
Coherence	Descending		
	Ascending		

**Figure 5.6** The SAR intensity and coherence difference and color composite map of the study area. The intensity difference was calculated by subtracting the pre-event from post-event SAR intensity image; descending and ascending coherence difference was calculated by subtracting pre-event from co-event InSAR coherence.

Landslide detection using SAR coherence and intensity images are affected by foreshortening, layover, and shadowing, due to the radar is measuring the distance to features in slant-range. Those factors will reduce landslide classification accuracy by adding commission and omission errors. While the SAR data from different orbits (i.e., descending and ascending) can be a good complementary to each other if such data are available. Therefore, we have examined the applicability of coherence and intensity on both descending and ascending orbits. The comparison results are described in section 5.6.1.

### 5.4.3. Statistical method

The statistical method refers to the use of the statistical parameters of the mean ( $\mu$ ) and the standard deviation ( $\sigma$ ) to calculate the threshold by  $\mu \pm n\sigma$  (**Figure 5.7**). In this method, the density function of the continuous change image is almost equal to the density function of the unmodified pixels, and in the determination of the threshold statistically fixed (A. D’Addabbo, 2004),  $n$  is an empirical parameter set by the user that can be adjusted (Vázquez-Jiménez *et al.*, 2018).

As shown in **Figure 5.6**, the intensity difference of ascending and descending data shows both increase and decrease in landslides. Therefore, the optimal threshold for the intensity was decided based on the criteria,  $\mu + n\sigma < \text{Landslide} < \mu - n\sigma$ . The  $n$  is the threshold coefficient value and can be adjusted according to the histogram. For the coherence difference, most landslides show significant decrease in coherence, while the cropland and grass show an increase in coherence **Figure 5.6**. Therefore, only the left threshold criteria,  $\text{Landslide} < \mu - n\sigma$  was used.

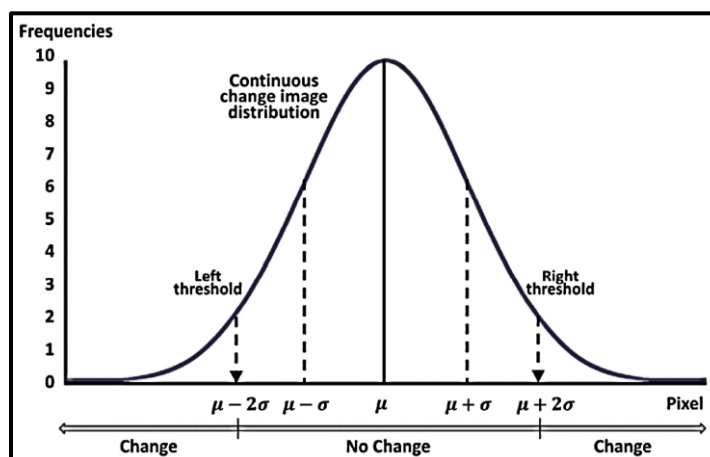


**Figure 5.7** Scheme of the definition of thresholds by the statistical method in a normal distribution. (adapted from (Vázquez-Jiménez *et al.*, 2018))

### 5.4.4. Decision tree method

The decision tree (DT) classification technique was adopted to map landslide by using pre- and co-event coherence images. The decision tree classifier is a type of multistage classifier that can be applied to a single image or a stack of images. Because of its simplicity, flexibility, and computational efficiency, it has been widely used in many studies ((Elnaggar *et al.*, 2009; Aimaiti, Kasimu and Jing, 2016)). The decision tree scheme is built based on inputs from pre- and co-event coherence, pre- and post-event intensity images, DEM, and Slope.

## 5.6. Results

### 5.6.1. Landslide classification using descending and ascending SAR images

The intensity and InSAR coherence are providing useful information on landslide and can be used to extract landslides. However, their performances in identifying the landslide might be different to some extent. Thus, we have tried six different combinations to extract landslides, (1) using only the coherence difference in descending mode PALSAR-2 images; (2) using only the intensity difference in descending mode PALSAR-2 images; (3) using both coherence and intensity difference in descending mode PALSAR-2 images; (4) using coherence difference in descending and ascending mode PALSAR-2 images; (5) using intensity difference in descending and ascending mode PALSAR-2 images; (6) using both coherence and intensity difference in descending and ascending mode PALSAR-2 images.

In case 1, we have only used the coherence difference in descending mode PALSAR-2 images (pre-event:20180823-20180614 and co-event:20180823-20180906). Through the analysis of the nature of landslide, the topography of the study area, the decision tree classifier for the extraction of the landslide was established (**Figure 5.8**). At first, the DEM and slope were resampled to the same ground resolution as the SAR coherence (15 m), and the data sets were layer stacked. The optimal threshold values of coherence difference image were determined by the statistical method (based on calculated mean and standard deviation values of coherence); a natural break classification method was used to classify the slope using ArcGIS. In the first step, the input image pixels were divided into two groups: landslide and non-landslide by coherence difference ( $\mu=-0.12$ ,  $n=0.5$ , and  $\sigma=0.131$ ) threshold of -0.19. In the second step, the pixels filtered through the above criteria were then divided into landslide and non-landslide by Slope threshold of 3.5 (degree). In the third step, the remaining pixels classified as landslide were divided into landslide and non-landslide by DEM threshold values of 83 (m). Finally, to remove the isolated noisy pixels,

the classified image was segmented (Number of neighbors 8 and a population minimum of 30) into regions of connected pixels that are contained in the same class. The final classified image is shown in **Figure 5.9**.

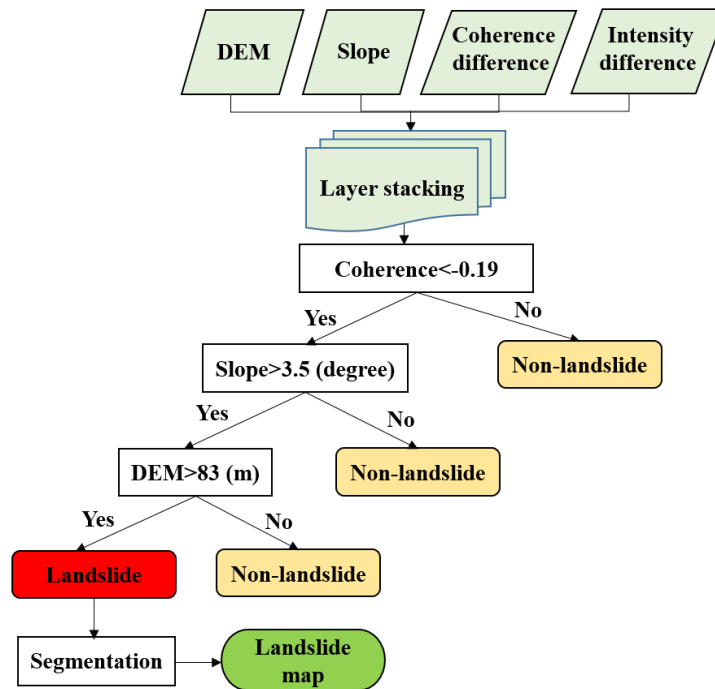


**Figure 5.8** The scheme of the decision tree-based landslide mapping.

Note: Coherence and intensity difference refer the both descending and ascending coherence and intensity.

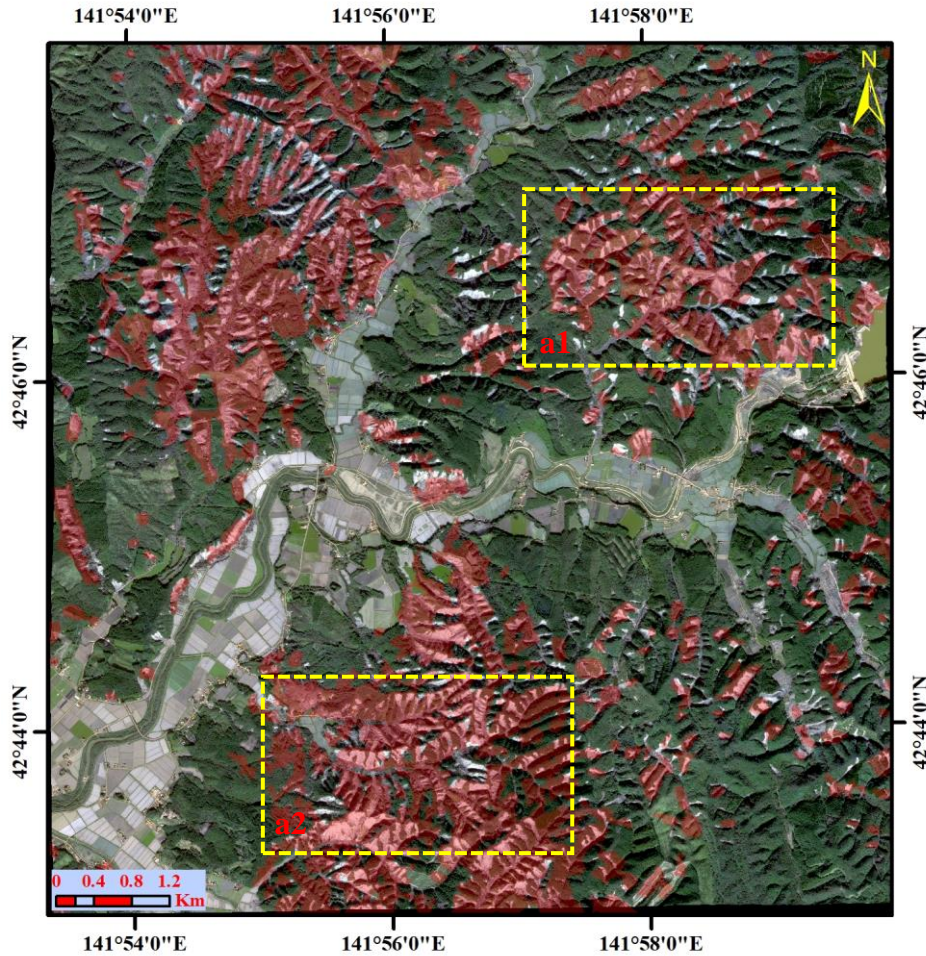


**Figure 5.9** The landslide classification map using only the descending SAR coherence. The background image is a high-resolution GeoEye-1 image taken on 20 October 2018.

For assessing the accuracy of the classification result, we have compared the result with the high-resolution optical images (WorldView-2 and GeoEye-1). As shown in **Figure 5.10c1** and **c2**, most of the landslide area were detected well by the proposed method. However, some small and medium scale landslides indicated in yellow circle and rectangle were omitted as non-landslide (**Figure 5.10c1**). Moreover, in **Figure 5.10c2**, a quite large landslide was also misclassified as non-landslide. This may be related to the SAR image geometry, and we used descending track PALSAR-2 image (west-facing sensor), the slopes facing away from the sensor (steep, west-facing slopes) were not well imaged. Moreover, the quality of the coherence (e.g., geometrical, temporal decorrelations, and atmospheric noise) may also hinder the full use of InSAR coherence.

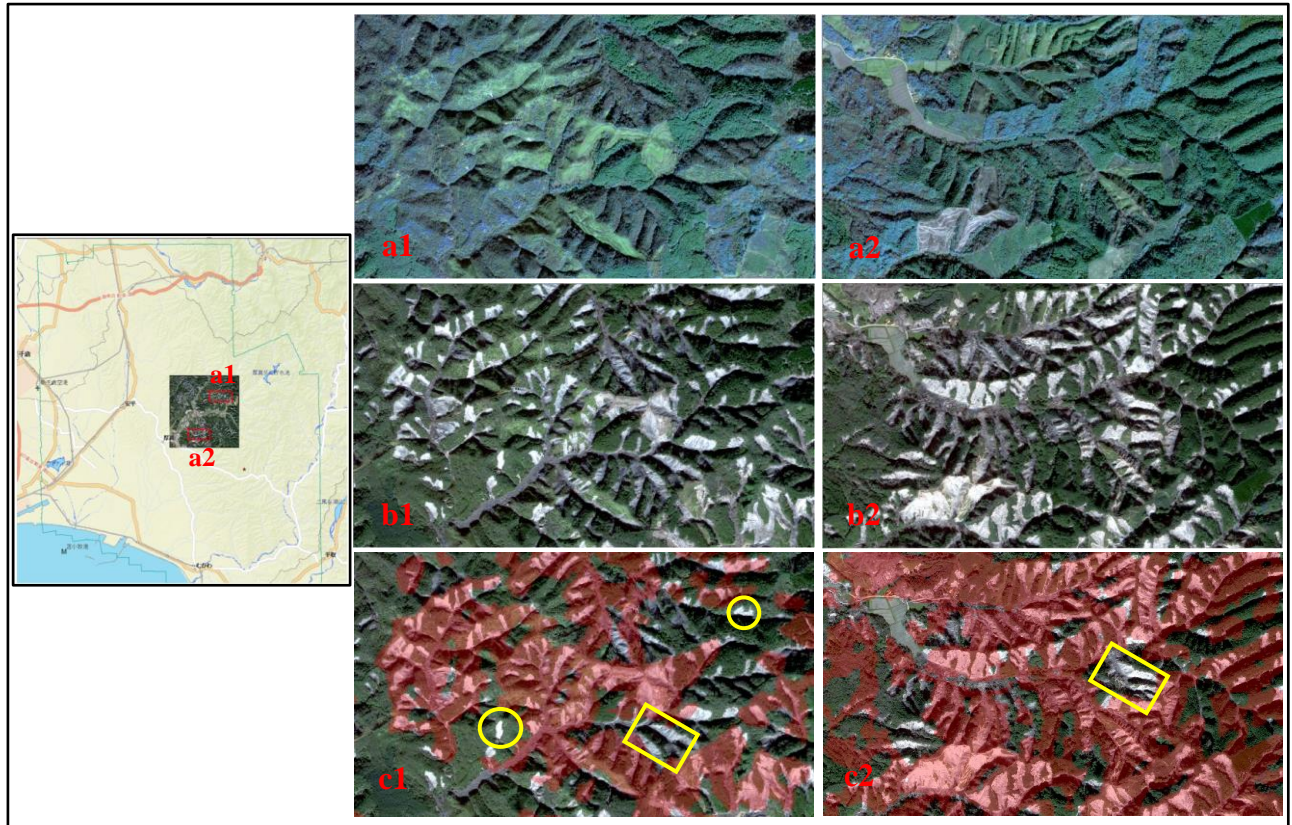


**Figure 5.10** The comparison of the classification results with the pre- and post-event high-resolution optical images. (a1 and a2) are the WorldView-2 image taken on 24 October 2017; (b1 and b2) are the GeoEye-1 image taken on 20 October 2018; (c1 and c2) are the identified landslides overlaid on the optical image.

In case 2, to examine the performance of SAR intensity in landslide mapping. We used the pre-event (2018089) and post-event (20180906) PALSAR-2 intensity images in descending mode and calculated their difference by subtracting the pre-event intensity from post-event intensity image. The same decision tree classification procedure was used with the intensity threshold criteria of  $-2.13 > \text{Intensity} > 1.91$  ( $\mu = -0.781$ ,  $\sigma = 2.695$ , left threshold ( $n = 0.5$ ), and right threshold ( $n = 1$ )). And then, the same threshold criteria of Slope and DEM was also used in this step to remove the flat areas which have classified as a landslide. The classification results were segmented to remove small speckles classified as a landslide. The final classification result is shown in **Figure 5.11**. From **Figure 5.11**, we can see that the intensity-based classification has shown a quite satisfactory result, especially the area in red rectangle has successfully classified as landslide, which has not been identified by the InSAR coherence-based method. However, many landslides are not fully identified by this method.

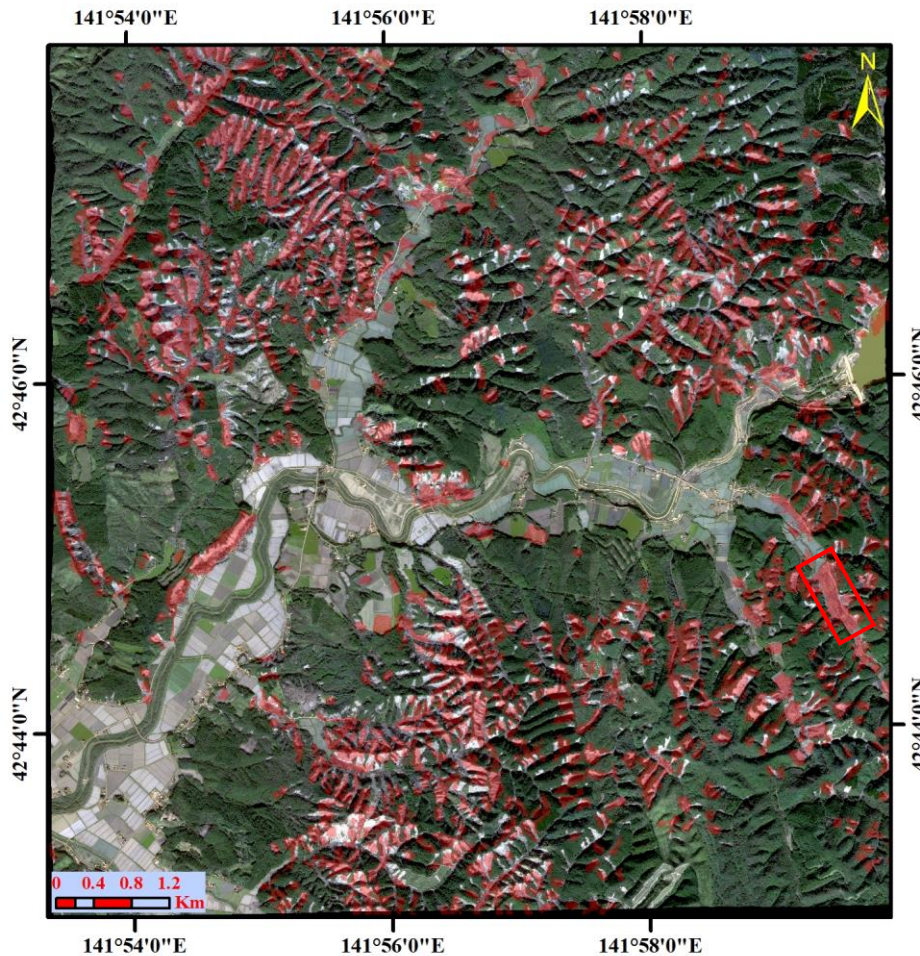


**Figure 5.11** The landslide classification map using only the descending SAR intensity. The background image is a high-resolution GeoEye-1 image taken on 20 October 2018.

In case 3, to improve the landslide classification results, we have combined the PASLAR-2 coherence and intensity difference images in descending mode. The same decision tree classification procedure was used, while the intensity difference threshold criteria ( $-2.13 > \text{Intensity} > 1.91$ ) was added to the coherence difference threshold ( $< -0.19$ ) criteria in the main node. And then, the same threshold criteria of Slope and DEM was also used in this step to remove the flat areas which have classified as a landslide. The same segmentation criteria was used to remove small speckles classified as landslides. The final classification result is shown in **Figure 5.12**. From **Figure 5.12**, we can see that, by combining the coherence and intensity difference, the possibilities of identifying landslides increased greatly. While the commission error (false landslide) was also increased (e.g., grassland and cropland classified as a landslide).



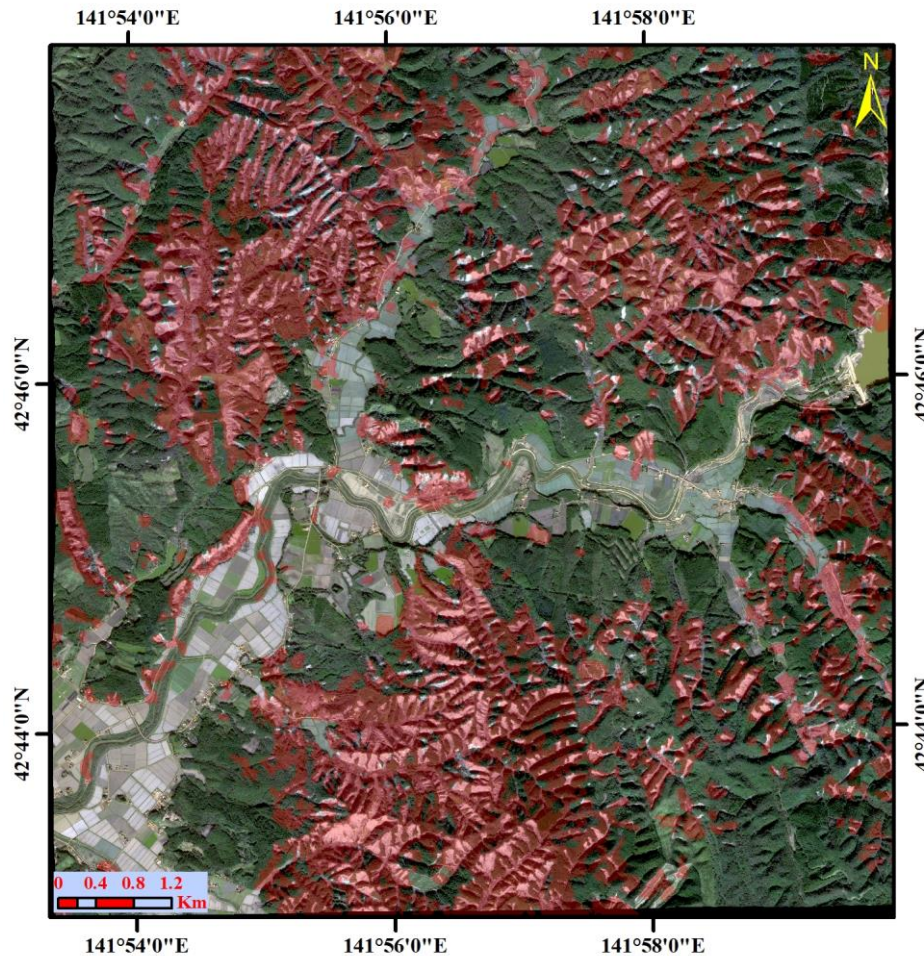


**Figure 5.12** The landslide classification map using both coherence and intensity difference in descending SAR images. The background image is a high-resolution GeoEye-1 image taken on 20 October 2018.

In case 4 and 5, we have attempted to combine both PALSAR-2 coherence and intensity difference images in descending and ascending mode, respectively. In case 4, for the combination of PALSAR-2 ascending and descending coherence, the same decision tree classification procedure used for the descending coherence was also used, the coherence difference threshold criteria (ascending  $< -0.18$  ( $\mu = -0.117$ ,  $\sigma = 0.122$ ,  $n = 0.5$ ) or descending  $< -0.19$ ) was added in the main node. In case 5, for the combination of PALSAR-2 ascending and descending intensity, the intensity difference threshold criteria ( $-2.13 > \text{descending intensity} > 1.91$  or  $-1.64 > \text{ascending intensity} > 2.83$  ( $\mu = 0.593$ ,  $\sigma = 2.232$ ,  $n = 1$ )) was added in the main node. And then, the same threshold criteria of Slope and DEM was also used to exclude the flat areas which have classified as a landslide. The same segmentation criteria was also used to remove small speckles classified as landslides. The final classification result is shown in **Figure 5.13** and **Figure 5.14**, respectively.

From these figures, we can see that, by adding the ascending coherence and intensity images to the descending, the possibilities of correctly identified landslides are increased. The descending and ascending coherence combination tends to overestimate the landslide. While the descending and ascending intensity combination shows a better result than the coherence and show less commission error (e.g., cropland and grassland classified as a landslide). However, a quantitative analyze is needed for their performance evaluation.



**Figure 5.13** The landslide classification map using coherence difference in both descending and ascending SAR images. The background image is a high-resolution GeoEye-1 image taken on 20 October 2018.

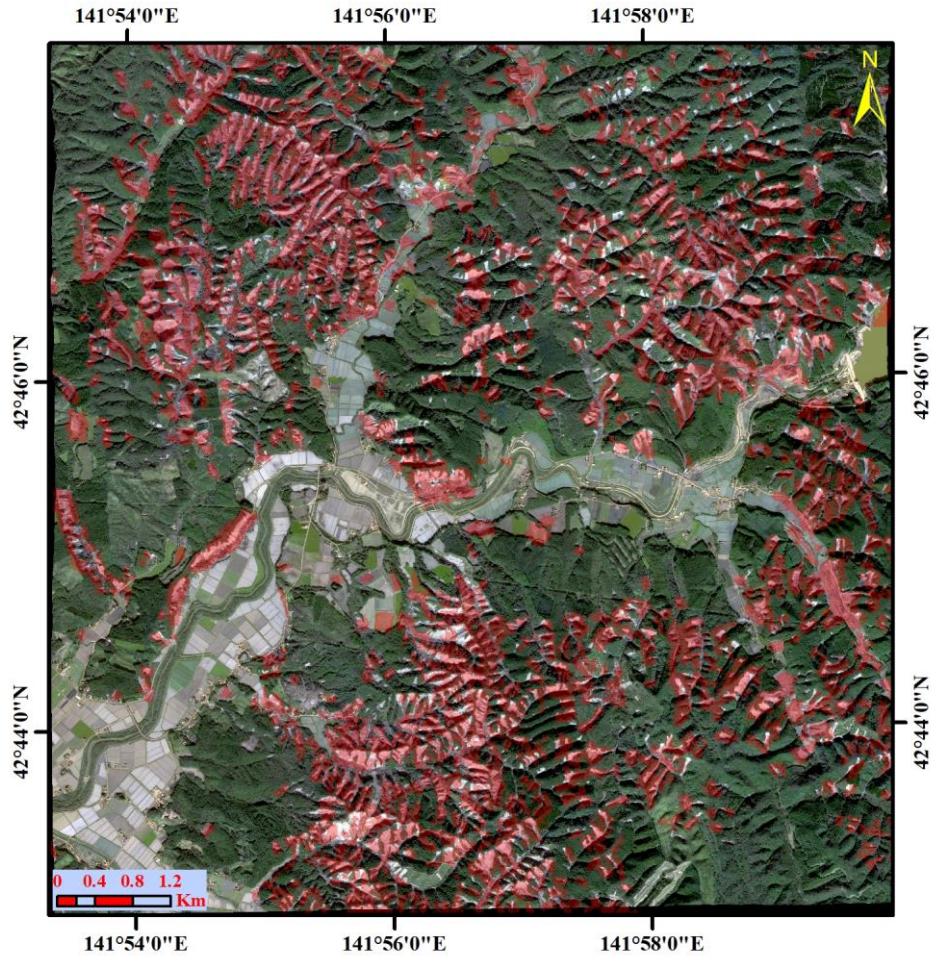


**Figure 5.14** The landslide classification map using intensity difference in both descending and ascending SAR images. The background image is a high-resolution GeoEye-1 image taken on 20 October 2018.

In case 6, we have combined both coherence and intensity difference in descending and ascending PASLAR-2 images. The combination was based on the threshold criteria used for the intensity and coherence difference in the previous steps. The same segmentation criteria was also used to remove small speckles classified as landslides. The final classification result is shown in **Figure 5.15**. We can see that almost all the landslides are identified by this method. However, as shown in the yellow rectangle in **Figure 5.15**, the possibilities of non-landslide areas classified as landslide were also increased. The vegetation changes between the two SAR acquisitions may have resulted in significant modification of the ground surface and therefore its scattering properties of phase and amplitude in both ascending and descending images. Therefore, further consideration must be taken to reduce the uncertainties caused by vegetation change.

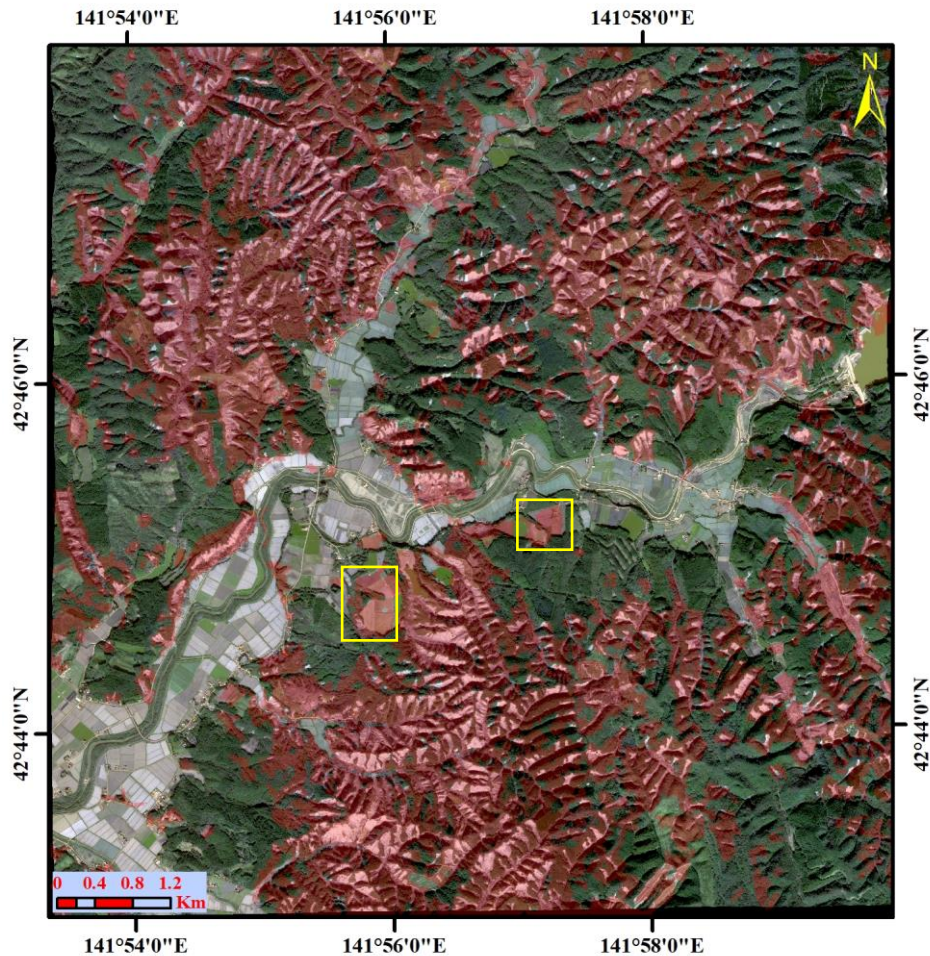


**Figure 5.15** The landslide classification map using coherence and intensity difference in both descending and ascending SAR images. The background image is a high-resolution GeoEye-1 image taken on 20 October 2018.

### 5.6.2. Quantitative analysis of the landslide classification accuracy

To evaluate the performance of six different combinations in landslide mapping, we compare the detected landslides with the polygon data of landslides released by GSI of Japan (GSI, 2018a). Before comparison, we have converted the classification results in raster to the same vector file as GSI (shapefile). And use the intersect tool in Analysis tool box in ArcGIS 10.3.1 software, we calculated the correctly classified landslides by comparing with the landslides released by GSI. Then, we computed the class statistics and confusion metrics for the six different combinations, as shown in **Table 5.1~5.6**.

**Table 5.1.** The accuracy assessment result of the landslide classification (case 1).

Note: UA and PA refer to the user's and producer's accuracy.

		Truth data			
Classification results		Landslides (Km <sup>2</sup> )	Others (Km <sup>2</sup> )	Total (Km <sup>2</sup> )	UA (%)
	Landslides	10.39	12.34	22.72	45.72
	Others	8.20	52.49	60.70	86.49
	Total	18.59	64.83	83.42	
	PA (%)	55.87	80.97		
Overall accuracy		75.38%	Kappa Coefficient		0.34

**Table 5.2.** The accuracy assessment result of the landslide classification (case 2).

		Truth data			
Classification results		Landslides (Km <sup>2</sup> )	Others (Km <sup>2</sup> )	Total (Km <sup>2</sup> )	UA (%)
	Landslides	8.71	7.16	15.87	54.89
	Others	9.88	57.67	67.55	85.37
	Total	18.59	64.83	83.42	
	PA (%)	46.86	88.96		
Overall accuracy		79.57%	Kappa Coefficient		0.38

**Table 5.3.** The accuracy assessment result of the landslide classification (case 3).

		Truth data			
Classification results		Landslides (Km <sup>2</sup> )	Others (Km <sup>2</sup> )	Total (Km <sup>2</sup> )	UA (%)
	Landslides	14.05	16.46	30.51	46.06
	Others	4.54	48.38	52.91	91.42
	Total	18.59	64.83	83.42	
	PA (%)	75.58	74.55		
Overall accuracy		74.83%	Kappa Coefficient		0.41

**Table 5.4.** The accuracy assessment result of the landslide classification (case 4).

		Truth data			
Classification results		Landslides (Km <sup>2</sup> )	Others (Km <sup>2</sup> )	Total (Km <sup>2</sup> )	UA (%)
	Landslides	12.62	16.99	29.61	42.61
	Others	5.97	47.84	53.81	88.89
	Total	18.59	64.83	83.42	
	PA (%)	67.86	73.79		
Overall accuracy		72.47%	Kappa Coefficient		0.34

**Table 5.5.** The accuracy assessment result of the landslide classification (case 5).

		Truth data			
Classification results		Landslides (Km <sup>2</sup> )	Others (Km <sup>2</sup> )	Total (Km <sup>2</sup> )	UA (%)
	Landslides	11.50	9.50	21	54.77
	Others	7.09	55.33	62.42	88.65
	Total	18.59	64.83	83.42	
	PA (%)	61.87	85.35		
Overall accuracy		80.12%	Kappa Coefficient		0.45

**Table 5.6.** The accuracy assessment result of the landslide classification (case 6).

		Truth data			
Classification results		Landslides (Km <sup>2</sup> )	Others (Km <sup>2</sup> )	Total (Km <sup>2</sup> )	UA (%)
	Landslides	16.01	20.98	36.99	43.28
	Others	2.58	43.85	46.43	93.6
	Total	18.59	64.83	83.42	
	PA (%)	86.12	67.64		
Overall accuracy		71.75%	Kappa Coefficient		0.39

**Table 5.1** shows the accuracy assessment result of the landslide classification using only the

descending SAR coherence (case 1). We can see that, estimated landslide area was 10.39 km<sup>2</sup> (55.9%), and the overall accuracy and Kappa coefficient were 75.38% and 0.34, respectively; The descending SAR intensity-based classification has identified less landslide (8.71 km<sup>2</sup>) but with small commission error than the coherence-based classification **Table 5.2** (case 2). The overall accuracy and Kappa coefficient were 79.47% and 0.38, respectively; The descending SAR coherence and intensity-based landslide classification (case 3) showed an increase in landslide identification (14.05 km<sup>2</sup>). However, the commission error was also increased and showed a lower overall accuracy (74.83%) than the single use of coherence and intensity (**Table 5.3**). The descending and ascending coherence-based classification lead more commission errors to landslides, which 16.99 km<sup>2</sup> out of 29.61 km<sup>2</sup> are wrongly classified as landslide (case 4). The overall accuracy and kappa coefficient were 72.47% and 0.34, respectively (**Table 5.4**). The descending and ascending intensity-based classification showed a better result than the coherence (case 5), the classified landslide was 11.5 km<sup>2</sup> (62%), and the overall accuracy and Kappa coefficient were 80.12% and 0.45, respectively (**Table 5.5**). The from the combined use of both descending and ascending intensity and coherence (case 6) have increased the possibilities of landslide identification, and correctly classified landslides were 16.01 km<sup>2</sup> (86.6%) out of total landslides (18.59 km<sup>2</sup>). However, the commission error was also increased accordingly, and up to 20.98 km<sup>2</sup> areas were misclassified as a landslide. The overall accuracy and kappa coefficient were 71.75% and 0.39, respectively (**Table 5.6**).

The quantitative comparison results show that the descending and ascending intensity-based classification has the best overall accuracy and kappa coefficient and less commission error. As the coherence is low in vegetation area and the geometrical and temporal decorrelations may also hinder the applicability of InSAR coherence, showed more commission error and lead lower overall accuracy in landslide classification.

## 5.7. Conclusion

In this study, to identify and map the landslides induced by the 2018 Hokkaido Eastern Iburu earthquake, we used six ALOS-2 PALSAR-2 data in descending and ascending mode taken before and after the earthquake. Six different combinations using the coherence and intensity difference were implemented in a rule-based decision tree classification scheme. The decision tree classification was established based on the calculated pre and co-event InSAR coherence

difference, pre and post-event intensity difference, DEM, and slope. Moreover, the accuracy of the classification results was compared with high-resolution optical images and truth data provided by GSI, Japan. The results showed that SAR coherence and intensity have great potentials in quickly identifying and mapping the earthquake-induced landslide. The detected landslides have a good match with the reference optical images. The quantitative comparison results showed that the descending and ascending intensity-based landslide classification has the best accuracy compared to other methods. Considering the complexity of the vegetated mountain terrain, and since the SAR sensors are side-looking and not all the aspects of the mountain are measured. Therefore, combined use of both ascending and descending sensors can be complementary to each other.



## Chapter 6

### General conclusions

This research aimed to investigate the features and feasibility of different radar images in the extraction of ground deformations. The traditional and advanced InSAR methods and GPS observations are also implemented to improve the accuracy of estimated ground deformations. The InSAR coherence and intensity-based classifications for the earthquake-induced landslides have also carried out using ALOS-2 PALSAR-2 data. The general conclusions for the three most relevant chapters can be summarized as follows.

In chapter 3, I investigated the measuring capability of different microwave bands (C and L-band) in small-scale ground deformation monitoring. A case study was conducted in a typical oilfield, in Karamay, China using ALOS-PALSAR and ENVISAT-ASAR data. The experimental results showed that the spatial patterns of the land uplift and their magnitudes between ALOS-PALSAR and ENVISAT-ASAR results agreed well with a correlation of 0.76. While the comparison with the GPS showed that, the measurement precision of C-band (5.6 cm) and L-band (23.6 cm) was 2.2 mm and 8.4 mm, respectively. This further suggests the shorter wavelength is more sensitive to slow ground deformations than longer wavelength.

In chapter 4, I applied the advanced InSAR techniques to monitor the long-term spatial patterns of land subsidence in the coastal city of Urayasu City using ERS-1/-2, ALOS-PALSAR, and ALOS-2PALSAR-2 data. The obtained InSAR results during the three observation periods from 1993–2006 and 2006-2010 and 2014 to 2017 show continuing subsidence occurring in several reclaimed areas of Urayasu City. The maximum subsidence rate from 1993 to 2006 was approximately 27 mm/year, from 2006 to 2010 it was 30 mm/year, and from 2014 to 2017 it was about 18 mm/year. The results from PALSAR-2 data showed better coherence than the PALSAR and ERS-1/-2, because of its higher resolution. The quantitative comparison with the leveling data showed that the results from ERS-1/-2 have the largest RMSE of 4.4 mm/year, while the RMSE for PALSAR and PALSAR-2 data was 0.9 and 2.2 mm/year, respectively. This may have been caused by the low resolution and coherence (in vegetated areas near the seaside) of ERS-1/-2 data.

Nevertheless, the InSAR-derived results agree relatively well with the result of the leveling measurements and suggest the reliability of the InSAR-measured subsidence rate.

In chapter 5, the SAR intensity and coherence from both ascending and descending orbits were used to identify and map landslides induced by the 2018 Hokkaido Eastern Iwate earthquake. We have used six different combination methods to identify landslide areas. A rule-based decision tree classification was used to implement six different combinations. The decision tree classification was established based on the calculated pre and co-event InSAR coherence and intensity images, DEM, and slope. Moreover, the landslide classification results were compared with the high-resolution optical images and truth data. The detected landslides have a good match with the reference images. The quantitative accuracy assessment results showed that the descending and ascending SAR intensity-based classification results have the best accuracy than other methods. In general, the InSAR coherence and intensity has great potentials in quickly identifying and mapping earthquake-induced landslides.

## References

- A. D'Addabbo, G. S. (2004) 'Three different unsupervised methods for change detection: an application', in *IEEE International IEEE International IEEE International Geoscience and Remote Sensing Symposium, 2004. IGARSS '04. Proceedings*. IEEE, pp. 1980–1983. doi: 10.1109/IGARSS.2004.1370735.
- Abidin, H. Z. *et al.* (2011) 'Land subsidence of Jakarta (Indonesia) and its relation with urban development', *Natural Hazards*, 59(3), pp. 1753–1771. doi: 10.1007/s11069-011-9866-9.
- Ahmad Abir, I. *et al.* (2015) 'Active tectonics of western Potwar Plateau–Salt Range, northern Pakistan from InSAR observations and seismic imaging', *Remote Sensing of Environment*. Elsevier, 168, pp. 265–275. doi: 10.1016/J.RSE.2015.07.011.
- Aimaiti, Y. *et al.* (2017) 'Monitoring of Land-Surface Deformation in the Karamay Oilfield, Xinjiang, China, Using SAR Interferometry', *Applied Sciences*, 7(8), p. 772. doi: 10.3390/app7080772.
- Aimaiti, Y., Kasimu, A. and Jing, G. (2016) 'Urban landscape extraction and analysis based on optical and microwave ALOS satellite data', *Earth Science Informatics*. doi: 10.1007/s12145-016-0264-4.
- Aobpaet, A. *et al.* (2013) 'InSAR time-series analysis of land subsidence in Bangkok, Thailand', *International Journal of Remote Sensing*, 34(8), pp. 2969–2982. doi: 10.1080/01431161.2012.756596.
- Armas, I. *et al.* (2017) 'Long-term ground deformation patterns of Bucharest using multi-temporal InSAR and multivariate dynamic analyses: A possible transpressional system?', *Scientific Reports*, 7. doi: 10.1038/srep43762.
- Bamler, R. and Hartl, P. (1998) 'Synthetic aperture radar interferometry', *Inverse Problems*. IOP Publishing, 14(4), pp. R1–R54. doi: 10.1088/0266-5611/14/4/001.
- Bardi, F. *et al.* (2014) 'Integration between ground based and satellite SAR data in landslide mapping: The San Fratello case study', *Geomorphology*. Elsevier, 223, pp. 45–60. doi: 10.1016/J.GEOMORPH.2014.06.025.
- Bayuaji, L., Sumantyo, J. T. S. and Kuze, H. (2010) 'ALOS PALSAR D-InSAR for land subsidence mapping in Jakarta, Indonesia', *Canadian Journal of Remote Sensing*. doi: 10.5589/m10-023.
- Berardino, P. *et al.* (2002) 'A new algorithm for surface deformation monitoring based on small baseline differential SAR interferograms', *IEEE Transactions on Geoscience and Remote Sensing*, 40(11), pp. 2375–2383. doi: 10.1109/TGRS.2002.803792.
- Bhattacharya, S. *et al.* (2011) 'Liquefaction of soil in the Tokyo Bay area from the 2011 Tohoku (Japan) earthquake', *Soil Dynamics and Earthquake Engineering*, 31(11), pp. 1618–1628. doi: 10.1016/j.soildyn.2011.06.006.
- Blanco-Sánchez, P. *et al.* (2008) 'The coherent pixels technique (CPT): An advanced DInSAR technique for nonlinear deformation monitoring', in *Pure and Applied Geophysics*. doi: 10.1007/s00024-008-0352-6.

- Burrows, K. *et al.* (2019) 'A New Method for Large-Scale Landslide Classification from Satellite Radar', *Remote Sensing*. Multidisciplinary Digital Publishing Institute, 11(3), p. 237. doi: 10.3390/rs11030237.
- Calò, F. *et al.* (2012) 'Assessing the activity of a large landslide in southern Italy by ground-monitoring and SAR interferometric techniques', *International Journal of Remote Sensing*. doi: 10.1080/01431161.2011.630331.
- Calò, F. *et al.* (2014) 'Enhanced landslide investigations through advanced DInSAR techniques: The Ivancich case study, Assisi, Italy', *Remote Sensing of Environment*. Elsevier, 142, pp. 69–82. doi: 10.1016/J.RSE.2013.11.003.
- Casagli, N. *et al.* (2017) 'Spaceborne, UAV and ground-based remote sensing techniques for landslide mapping, monitoring and early warning', *Geoenvironmental Disasters*. SpringerOpen, 4(1), p. 9. doi: 10.1186/s40677-017-0073-1.
- Chai, J.-C. *et al.* (2004) 'Land subsidence due to groundwater drawdown in Shanghai', *Géotechnique*, 54(2), pp. 143–147. doi: 10.1680/geot.54.2.143.36332.
- Chatterjee, A. *et al.* (2013) 'Background error covariance estimation for atmospheric CO<sub>2</sub> data assimilation', *Journal of Geophysical Research: Atmospheres*. John Wiley & Sons, Ltd, 118(17), pp. 10,140-10,154. doi: 10.1002/jgrd.50654.
- Chaussard, E. *et al.* (2013) 'Sinking cities in Indonesia: ALOS PALSAR detects rapid subsidence due to groundwater and gas extraction', *Remote Sensing of Environment*. Elsevier, 128, pp. 150–161. doi: 10.1016/J.RSE.2012.10.015.
- Chaussard, E. *et al.* (2014) 'Land subsidence in central Mexico detected by ALOS InSAR time-series', *Remote Sensing of Environment*, 140, pp. 94–106. doi: 10.1016/j.rse.2013.08.038.
- Chaussard, E., Amelung, F. and Aoki, Y. (2013) 'Characterization of open and closed volcanic systems in Indonesia and Mexico using InSAR time series', *Journal of Geophysical Research: Solid Earth*. John Wiley & Sons, Ltd, 118(8), pp. 3957–3969. doi: 10.1002/jgrb.50288.
- Chen, G. *et al.* (2018) 'Detection of land subsidence associated with land creation and rapid urbanization in the Chinese Loess Plateau using time series InSAR: A case study of Lanzhou New District', *Remote Sensing*, 10(2). doi: 10.3390/rs10020270.
- Chiba prefecture (2015) *Land subsidence survey report on 2014*. Available at: <https://www.pref.chiba.lg.jp/suiho/press/2015/h26-jibanchinka.html> (Accessed: 19 March 2018).
- Chiba Prefecture (2016a) *Chiba Prefecture geological environment Information bank*. Available at: <https://www.pref.chiba.lg.jp/suiho/chishitsu.html> (Accessed: 7 July 2018).
- Chiba Prefecture (2016b) *Chiba prefecture water source information*. Available at: <https://www.pref.chiba.lg.jp/suidou/souki/2nd-page/suigen.html> (Accessed: 19 March 2018).
- Chiba Prefecture (2017a) *Chiba Prefecture leveling survey results*. Available at: <http://www.pref.chiba.lg.jp/suiho/jibanchinka/torikumi/seikaomote.html> (Accessed: 16 March 2018).

- Chiba Prefecture (2017b) *Survey results of ground water use in Chiba Prefecture*. Available at: <https://www.pref.chiba.lg.jp/suiho/jibanchinka/torikumi/yousuiryou.html> (Accessed: 13 April 2018).
- Chiba Prefecture (2018) *Chiba Information Map*. Available at: <http://map.pref.chiba.lg.jp/pref-chiba/Portal> (Accessed: 16 March 2018).
- Cianflone, G. *et al.* (2015) 'InSAR time series analysis of natural and anthropogenic coastal plain subsidence: The case of sibili (Southern Italy)', *Remote Sensing*, 7(12), pp. 16004–16023. doi: 10.3390/rs71215812.
- Costantini, M. (1998) 'A novel phase unwrapping method based on network programming', *Geoscience and Remote Sensing, IEEE Transactions on*, 36(3), pp. 813–821. doi: 10.1109/36.673674.
- Costantini, M. *et al.* (2008) 'A New Method for Identification and Analysis of Persistent Scatterers in Series of SAR Images', in *IGARSS 2008 - 2008 IEEE International Geoscience and Remote Sensing Symposium*. IEEE, pp. II-449-II-452. doi: 10.1109/IGARSS.2008.4779025.
- Crosetto, M. *et al.* (2008) 'Generation of Advanced ERS and Envisat Interferometric SAR Products Using the Stable Point Network Technique', *Photogrammetric Engineering & Remote Sensing*, 74(4), pp. 443–450. doi: 10.14358/PERS.74.4.443.
- Crosetto, M. *et al.* (2016) 'Persistent Scatterer Interferometry: A review', *ISPRS Journal of Photogrammetry and Remote Sensing*, pp. 78–89. doi: 10.1016/j.isprsjprs.2015.10.011.
- Dong, J. *et al.* (2018) 'Measuring precursory movements of the recent Xinmo landslide in Mao County, China with Sentinel-1 and ALOS-2 PALSAR-2 datasets', *Landslides*. Springer Berlin Heidelberg, 15(1), pp. 135–144. doi: 10.1007/s10346-017-0914-8.
- Dong, S. *et al.* (2014) 'Time-series analysis of subsidence associated with rapid urbanization in Shanghai, China measured with SBAS InSAR method', *Environmental Earth Sciences*, 72(3), pp. 677–691. doi: 10.1007/s12665-013-2990-y.
- Du, Z. *et al.* (2016) 'Subsidence Monitoring over the Southern Coalfield, Australia Using both L-Band and C-Band SAR Time Series Analysis', *Remote Sensing*. Multidisciplinary Digital Publishing Institute, 8(7), p. 543. doi: 10.3390/rs8070543.
- ElGharbawi, T. and Tamura, M. (2015) 'Estimating deformation due to soil liquefaction in Urayasu city, Japan using permanent scatterers', *ISPRS Journal of Photogrammetry and Remote Sensing*, 109, pp. 152–164. doi: 10.1016/j.isprsjprs.2015.09.002.
- Elnaggar, A. *et al.* (2009) 'Application of Remote-sensing Data and Decision-Tree Analysis to Mapping Salt-Affected Soils over Large Areas', *Remote Sensing*. Molecular Diversity Preservation International, 2(1), pp. 151–165. doi: 10.3390/rs2010151.
- ESA (no date) *PRARE Precise Orbit Product (ERS.ORB.POD)*. Available at: <https://earth.esa.int/web/guest/-/prare-precise-orbit-product> (Accessed: 18 May 2018).

- Ferretti, A. *et al.* (2007) *InSAR Principles: Guidelines for SAR Interferometry Processing and Interpretation*. Edited by Karen Fletcher. ESA Publications: Noordwijk, Netherlands. Available at: [https://www.esa.int/esapub/tm/tm19/TM-19\\_ptA.pdf](https://www.esa.int/esapub/tm/tm19/TM-19_ptA.pdf) (Accessed: 19 May 2019).
- Ferretti, A. *et al.* (2011) 'A new algorithm for processing interferometric data-stacks: SqueeSAR', in *IEEE Transactions on Geoscience and Remote Sensing*. doi: 10.1109/TGRS.2011.2124465.
- Ferretti, A., Prati, C. and Rocca, F. (2000) 'Nonlinear Subsidence Rate Estimation Using Permanent Scatterers in Differential SAR Interferometry', *IEEE Transactions on Geoscience and Remote Sensing*, 38(5), pp. 2202–2212. doi: 10.1109/36.868878.
- Ferretti, A., Prati, C. and Rocca, F. (2001) 'Permanent scatterers in SAR interferometry', *IEEE Transactions on Geoscience and Remote Sensing*, 39(1), pp. 8–20. doi: 10.1109/36.898661.
- Gabriel, A. K., Goldstein, R. M. and Zebker, H. A. (1989) 'Mapping small elevation changes over large areas: Differential radar interferometry', *Journal of Geophysical Research*. John Wiley & Sons, Ltd, 94(B7), p. 9183. doi: 10.1029/JB094iB07p09183.
- Ganas, A. *et al.* (2016) 'Coseismic deformation, field observations and seismic fault of the 17 November 2015 M = 6.5, Lefkada Island, Greece earthquake', *Tectonophysics*. Elsevier, 687, pp. 210–222. doi: 10.1016/J.TECTO.2016.08.012.
- Goldstein, R. M. and Werner, C. L. (1998) 'Radar interferogram filtering for geophysical applications', *Geophysical Research Letters*, 25(21), pp. 4035–4038. doi: 10.1029/1998GL900033.
- Gourmelen, N., Amelung, F. and Lanari, R. (2010) 'Interferometric synthetic aperture radar-GPS integration: Interseismic strain accumulation across the Hunter Mountain fault in the eastern California shear zone', *Journal of Geophysical Research: Solid Earth*, 115(9). doi: 10.1029/2009JB007064.
- Grzovic, M. and Ghulam, A. (2015) 'Evaluation of land subsidence from underground coal mining using TimeSAR (SBAS and PSI) in Springfield, Illinois, USA', *Natural Hazards*. Springer Netherlands, 79(3), pp. 1739–1751. doi: 10.1007/s11069-015-1927-z.
- GSI (2018a) *2018-Hokkaido Eastern Iburi Earthquake*. Available at: <http://www.gsi.go.jp/BOUSAI/H30-hokkaidoiburi-east-earthquake-index.html#1> (Accessed: 18 May 2019).
- GSI (2018b) *Fundamental Geospatial Data portal of GSI*. Available at: <https://fgd.gsi.go.jp/download/menu.php> (Accessed: 16 March 2018).
- Guéguen, Y. *et al.* (2009) 'Monitoring residual mining subsidence of Nord/Pas-de-Calais coal basin from differential and Persistent Scatterer Interferometry (Northern France)', *Journal of Applied Geophysics*. Elsevier, 69(1), pp. 24–34. doi: 10.1016/J.JAPPGEO.2009.02.008.
- Guglielmi, Y. *et al.* (2015) 'INDUCED SEISMICITY. Seismicity triggered by fluid injection-induced aseismic slip.', *Science (New York, N.Y.)*. American Association for the Advancement of Science, 348(6240), pp. 1224–6. doi: 10.1126/science.aab0476.

- Heimlich, C. *et al.* (2015) ‘Uplift around the geothermal power plant of Landau (Germany) as observed by InSAR monitoring’, *Geothermal Energy*. SpringerOpen, 3(1), p. 2. doi: 10.1186/s40517-014-0024-y.
- Ho Tong Minh, D., Van Trung, L. and Le Toan, T. (2015) ‘Mapping ground subsidence phenomena in Ho Chi Minh City through the radar interferometry technique using ALOS PALSAR data’, *Remote Sensing*, 7(7), pp. 8543–8562. doi: 10.3390/rs70708543.
- Hooper, A. *et al.* (2004) ‘A new method for measuring deformation on volcanoes and other natural terrains using InSAR persistent scatterers’, *Geophysical Research Letters*, 31(23), pp. 1–5. doi: 10.1029/2004GL021737.
- Hooper, A. *et al.* (2012) ‘Recent advances in SAR interferometry time series analysis for measuring crustal deformation’, *Tectonophysics*, pp. 1–13. doi: 10.1016/j.tecto.2011.10.013.
- Hooper, A. J. (2008) ‘A multi-temporal InSAR method incorporating both persistent scatterer and small baseline approaches’, *Geophysical Research Letters*, 35(16). doi: 10.1029/2008GL034654.
- Hooper, A. and Zebker, H. A. (2007) ‘Phase unwrapping in three dimensions with application to InSAR time series’, *Journal of the Optical Society of America A*, 24(9), p. 2737. doi: 10.1364/JOSAA.24.002737.
- Hsieh, C. S. *et al.* (2011) ‘Using differential SAR interferometry to map land subsidence: A case study in the Pingtung Plain of SW Taiwan’, *Natural Hazards*, 58(3), pp. 1311–1332. doi: 10.1007/s11069-011-9734-7.
- Imakiire, T. and Koarai, M. (2012) ‘Wide-area land subsidence caused by “the 2011 off the Pacific Coast of Tohoku Earthquake”’, *Soils and Foundations*, 52(5), pp. 842–855. doi: 10.1016/j.sandf.2012.11.007.
- Ishii, I. *et al.* (2017) ‘DESIGN OF GRID-WALL SOIL IMPROVEMENT TO MITIGATE SOIL LIQUEFACTION DAMAGE IN RESIDENTIAL AREAS IN URAYASU’, *Journal of JSCE*. JSCE, 5(1), pp. 27–44. doi: 10.2208/journalofjsce.5.1\_27.
- Ji, L. *et al.* (2016) ‘Detecting land uplift associated with enhanced oil recovery using InSAR in the Karamay oil field, Xinjiang, China’, *International Journal of Remote Sensing*. Taylor & Francis, 37(7), pp. 1527–1540. doi: 10.1080/01431161.2016.1154222.
- Jo, M.-J., Jung, H.-S. and Won, J.-S. (2017) ‘Measurement of precise three-dimensional volcanic deformations via TerraSAR-X synthetic aperture radar interferometry’, *Remote Sensing of Environment*. Elsevier, 192, pp. 228–237. doi: 10.1016/J.RSE.2017.02.022.
- Jones, C. E. *et al.* (2016) ‘Anthropogenic and geologic influences on subsidence in the vicinity of New Orleans, Louisiana’, *Journal of Geophysical Research: Solid Earth*, 121(5), pp. 3867–3887. doi: 10.1002/2015JB012636.
- Jordan, R. (1980) ‘The Seasat-A synthetic aperture radar system’, *IEEE Journal of Oceanic Engineering*, 5(2), pp. 154–164. doi: 10.1109/JOE.1980.1145451.
- Kampes, B. M. (2005) ‘Displacement parameter estimation using permanent scatterer interferometry’. Available at: <https://repository.tudelft.nl/islandora/object/uuid%3A9f11f2ef-2db4-4583-a763-ae88e06ee3b> (Accessed: 16 May 2019).

- Khakim, M. Y. N., Tsuji, T. and Matsuoka, T. (2012) 'Geomechanical modeling for InSAR-derived surface deformation at steam-injection oil sand fields', *Journal of Petroleum Science and Engineering*. Elsevier, 96–97, pp. 152–161. doi: 10.1016/J.PETROL.2012.08.003.
- Konagai, K. *et al.* (2013) 'Maps of soil subsidence for Tokyo bay shore areas liquefied in the March 11th, 2011 off the Pacific Coast of Tohoku Earthquake', *Soil Dynamics and Earthquake Engineering*, 53, pp. 240–253. doi: 10.1016/j.soildyn.2013.06.012.
- Konishi, T. and Suga, Y. (2018) 'Landslide detection using COSMO-SkyMed images: a case study of a landslide event on Kii Peninsula, Japan', *European Journal of Remote Sensing*. Taylor & Francis, 51(1), pp. 205–221. doi: 10.1080/22797254.2017.1418185.
- Koster, K., Erkens, G. and Zwanenburg, C. (2016) 'A new soil mechanics approach to quantify and predict land subsidence by peat compression', *Geophysical Research Letters*, 43(20), pp. 10,792-10,799. doi: 10.1002/2016GL071116.
- Lawrence, I., K. L. (1989) 'A Concordance Correlation Coefficient to Evaluate Reproducibility', *Biometrics*. International Biometric Society, 45(1), p. 255. doi: 10.2307/2532051.
- Li, X.; Li, W.; Gao, B.; Yang, D. (2012) 'Study on subsurface water injection in Qizhong area of Karamay oilfield', *Xinjiang Oil Gas*, 8, pp. 57-59 (In Chinese).
- Li, M. *et al.* (2016) 'Detection of coal-mining-induced subsidence and mapping of the resulting deformation using time series of ALOS-PALSAR data', *Remote Sensing Letters*. Taylor & Francis, 7(9), pp. 855–864. doi: 10.1080/2150704X.2016.1193794.
- Liu, W. *et al.* (2015) 'Estimation of three-dimensional crustal movements in the 2011 Tohoku-Oki, Japan, earthquake from TerraSAR-X intensity images', *Natural Hazards and Earth System Sciences*, 15(3), pp. 637–645. doi: 10.5194/nhess-15-637-2015.
- Massonnet, D. *et al.* (1993) 'The displacement field of the Landers earthquake mapped by radar interferometry', *Nature*. Nature Publishing Group, 364(6433), pp. 138–142. doi: 10.1038/364138a0.
- Masumi, Y. *et al.* (2013) 'APSAR2013 : 2013 Asia-Pacific Conference on Synthetic Aperture Radar (APSAR)', in *Conference Proceedings of 2013 Asia-Pacific Conference on Synthetic Aperture Radar (APSAR)*. Tsukuba, Japan: IEEE. Available at: <https://ieeexplore.ieee.org/abstract/document/6705060> (Accessed: 17 May 2019).
- McKeen, S. *et al.* (2005) 'Assessment of an ensemble of seven real-time ozone forecasts over eastern North America during the summer of 2004', *Journal of Geophysical Research*. John Wiley & Sons, Ltd, 110(D21), p. D21307. doi: 10.1029/2005JD005858.
- Moreira, A. *et al.* (2013) 'A tutorial on synthetic aperture radar', *IEEE Geoscience and Remote Sensing Magazine*, 1(1), pp. 6–43. doi: 10.1109/MGRS.2013.2248301.



- Ng, A. H. M. *et al.* (2012) 'Mapping land subsidence in Jakarta, Indonesia using persistent scatterer interferometry (PSI) technique with ALOS PALSAR', *International Journal of Applied Earth Observation and Geoinformation*, 18(1), pp. 232–242. doi: 10.1016/j.jag.2012.01.018.
- Nigorikawa, N. and Asaka, Y. (2015) 'Leveling of long-term settlement of Holocene clay ground induced by the 2011 off the Pacific coast of Tohoku earthquake', *Soils and Foundations*, 55(5), pp. 1318–1325. doi: 10.1016/j.sandf.2015.09.029.
- Normand, J. C. L. and Heggy, E. (2015) 'InSAR Assessment of Surface Deformations in Urban Coastal Terrains Associated with Groundwater Dynamics', *IEEE Transactions on Geoscience and Remote Sensing*, 53(12), pp. 6356–6371. doi: 10.1109/TGRS.2015.2437368.
- Normile, D. (2018) 'Slippery volcanic soils blamed for deadly landslides during Hokkaido earthquake', *Science*. doi: 10.1126/science.aav3821.
- Okada, N. *et al.* (2011) 'The 2011 eastern Japan great earthquake disaster: Overview and comments', *International Journal of Disaster Risk Science*, 2(1), pp. 34–42. doi: 10.1007/s13753-011-0004-9.
- Osmanoğlu, B. *et al.* (2016) 'Time series analysis of InSAR data: Methods and trends', *ISPRS Journal of Photogrammetry and Remote Sensing*, pp. 90–102. doi: 10.1016/j.isprs.2015.10.003.
- Ozawa, S. *et al.* (2011) 'Coseismic and postseismic slip of the 2011 magnitude-9 Tohoku-Oki earthquake', *Nature*. Nature Publishing Group, 475(7356), pp. 373–376. doi: 10.1038/nature10227.
- Pan, F. *et al.* (2012) 'Evaluation of ecological sensitivity in Karamay, Xinjiang, China', *Journal of Geographical Sciences*. SP Science Press, 22(2), pp. 329–345. doi: 10.1007/s11442-012-0930-5.
- Pang, P. (2001) 'The first large oil field in China-Karamay oil field', *J. Univ. Pet. China*, 17, pp. 29–32.
- Pasquali, P. *et al.* (2015) 'Monitoring land subsidence in the Tokyo region with SAR interferometric stacking techniques', in *Engineering Geology for Society and Territory - Volume 5: Urban Geology, Sustainable Planning and Landscape Exploitation*, pp. 995–999. doi: 10.1007/978-3-319-09048-1\_191.
- Pepe, A. and Calò, F. (2017) 'A Review of Interferometric Synthetic Aperture RADAR (InSAR) Multi-Track Approaches for the Retrieval of Earth's Surface Displacements', *Applied Sciences*. Multidisciplinary Digital Publishing Institute, 7(12), p. 1264. doi: 10.3390/app7121264.
- Perissin, D. and Wang, T. (2012) 'Repeat-Pass SAR Interferometry With Partially Coherent Targets', *IEEE Transactions on Geoscience and Remote Sensing*, 50(1), pp. 271–280. doi: 10.1109/TGRS.2011.2160644.
- Plank, S. (2014) 'Rapid Damage Assessment by Means of Multi-Temporal SAR — A Comprehensive Review and Outlook to Sentinel-1', *Remote Sensing*. Multidisciplinary Digital Publishing Institute, 6(6), pp. 4870–4906. doi: 10.3390/rs6064870.
- Plank, S. *et al.* (2016) 'Landslide Mapping in Vegetated Areas Using Change Detection Based on Optical and Polarimetric SAR Data', *Remote Sensing*. Multidisciplinary Digital Publishing Institute, 8(4), p. 307. doi: 10.3390/rs8040307.

- Pradhan, B. *et al.* (2014) 'Land subsidence susceptibility mapping at Kinta Valley (Malaysia) using the evidential belief function model in GIS', *Natural Hazards*, 73(2), pp. 1019–1042. doi: 10.1007/s11069-014-1128-1.
- Prati, C., Ferretti, A. and Perissin, D. (2010) 'Recent advances on surface ground deformation measurement by means of repeated space-borne SAR observations', *Journal of Geodynamics*. Pergamon, 49(3–4), pp. 161–170. doi: 10.1016/J.JOG.2009.10.011.
- Qu, F. *et al.* (2015) 'Mapping ground deformation over Houston-Galveston, Texas using multi-temporal InSAR', *Remote Sensing of Environment*, 169, pp. 290–306. doi: 10.1016/j.rse.2015.08.027.
- Raspini, F. *et al.* (2014) 'Ground subsidence phenomena in the Delta municipality region (Northern Greece): Geotechnical modeling and validation with Persistent Scatterer Interferometry', *International Journal of Applied Earth Observation and Geoinformation*, 28(1), pp. 78–89. doi: 10.1016/j.jag.2013.11.010.
- Regional disaster prevention project of Urayasu City - earthquake disaster* (2011). Available at: [https://www.city.urayasu.lg.jp/\\_res/projects/default\\_project/\\_page\\_/001/002/417/1-4.pdf](https://www.city.urayasu.lg.jp/_res/projects/default_project/_page_/001/002/417/1-4.pdf) (Accessed: 19 June 2018).
- Roback, K. *et al.* (2018) 'The size, distribution, and mobility of landslides caused by the 2015 Mw7.8 Gorkha earthquake, Nepal', *Geomorphology*. Elsevier, 301, pp. 121–138. doi: 10.1016/J.GEOMORPH.2017.01.030.
- Rosen, P. A. *et al.* (1996) 'Surface deformation and coherence measurements of Kilauea Volcano, Hawaii, from SIR-C radar interferometry', *Journal of Geophysical Research: Planets*, 101(E10), pp. 23109–23125. doi: 10.1029/96JE01459.
- Rosen, P. A. *et al.* (2000) 'Synthetic aperture radar interferometry - Invited paper', *Proc. {IEEE}*, 88(3), pp. 333–382.
- Ruch, J. *et al.* (2008) 'Caldera-scale inflation of the Lazufre volcanic area, South America: Evidence from InSAR', *Journal of Volcanology and Geothermal Research*. doi: 10.1016/j.jvolgeores.2008.03.009.
- Samsonov, S., d'Oreye, N. and Smets, B. (2013) 'Ground deformation associated with post-mining activity at the French–German border revealed by novel InSAR time series method', *International Journal of Applied Earth Observation and Geoinformation*. Elsevier, 23, pp. 142–154. doi: 10.1016/J.JAG.2012.12.008.
- Sánchez-Gómez, P. *et al.* (2017) 'Glacier Surface Velocity Retrieval Using D-InSAR and Offset Tracking Techniques Applied to Ascending and Descending Passes of Sentinel-1 Data for Southern Ellesmere Ice Caps, Canadian Arctic', *Remote Sensing*. Multidisciplinary Digital Publishing Institute, 9(5), p. 442. doi: 10.3390/rs9050442.
- Satyabala, S. P. (2016) 'Spatiotemporal variations in surface velocity of the Gangotri glacier, Garhwal Himalaya, India: Study using synthetic aperture radar data', *Remote Sensing of Environment*. Elsevier, 181, pp. 151–161. doi: 10.1016/J.RSE.2016.03.042.

- Schulz, W. H. *et al.* (2017) 'Landslide kinematics and their potential controls from hourly to decadal timescales: Insights from integrating ground-based InSAR measurements with structural maps and long-term monitoring data', *Geomorphology*. Elsevier, 285, pp. 121–136. doi: 10.1016/J.GEOMORPH.2017.02.011.
- Shao, X. *et al.* (2019) 'Planet Image-Based Inventorying and Machine Learning-Based Susceptibility Mapping for the Landslides Triggered by the 2018 Mw6.6 Tomakomai, Japan Earthquake', *Remote Sensing*. Multidisciplinary Digital Publishing Institute, 11(8), p. 978. doi: 10.3390/rs11080978.
- Shirzaei, M. *et al.* (2016) 'Surface uplift and time-dependent seismic hazard due to fluid injection in eastern Texas.', *Science (New York, N.Y.)*. American Association for the Advancement of Science, 353(6306), pp. 1416–1419. doi: 10.1126/science.aag0262.
- Sowter, A. *et al.* (2013) 'Dinsar estimation of land motion using intermittent coherence with application to the south derbyshire and leicestershire coalfields', *Remote Sensing Letters*. doi: 10.1080/2150704X.2013.823673.
- Strozzi, T. *et al.* (2013) 'Interpretation of Aerial Photographs and Satellite SAR Interferometry for the Inventory of Landslides', *Remote Sensing*. Multidisciplinary Digital Publishing Institute, 5(5), pp. 2554–2570. doi: 10.3390/rs5052554.
- Sun, H. *et al.* (2017) 'Monitoring land subsidence in the southern part of the lower Liaohe plain, China with a multi-track PS-InSAR technique', *Remote Sensing of Environment*. Elsevier, 188, pp. 73–84. doi: 10.1016/J.RSE.2016.10.037.
- Tamburini, A. *et al.* (2010) 'Retrieving surface deformation by PSInSAR™ technology: A powerful tool in reservoir monitoring', *International Journal of Greenhouse Gas Control*. Elsevier, 4(6), pp. 928–937. doi: 10.1016/J.IJGGC.2009.12.009.
- Tantianuparp, P. *et al.* (2013) 'Characterization of Landslide Deformations in Three Gorges Area Using Multiple InSAR Data Stacks', *Remote Sensing*. Multidisciplinary Digital Publishing Institute, 5(6), pp. 2704–2719. doi: 10.3390/rs5062704.
- Tessler, Z. D. *et al.* (2015) 'Profiling risk and sustainability in coastal deltas of the world', *Science*, 349(6248), pp. 638–643. doi: 10.1126/science.aab3574.
- Tofani, V. *et al.* (2013) 'Technical Note: Use of remote sensing for landslide studies in Europe', *Natural Hazards and Earth System Sciences*, 13(2), pp. 299–309. doi: 10.5194/nhess-13-299-2013.
- Tokimatsu, K. *et al.* (2012) 'Building damage associated with geotechnical problems in the 2011 Tohoku Pacific Earthquake', *Soils and Foundations*, 52(5), pp. 956–974. doi: 10.1016/j.sandf.2012.11.014.
- Tokimatsu, K. *et al.* (2013) 'Geotechnical Problems in the 2011 Tohoku Pacific Earthquakes', in *International Conference on Case Histories in Geotechnical Engineering*. 2. Missouri University of Science and Technology. Available at: <http://scholarsmine.mst.edu/icchge/7icchge/session12/2/>.

- Tokimatsu, K. and Katsumata, K. (2012) ‘Liquefaction-induced damage to buildings in Urayasu city during the 2011 Tohoku Pacific earthquake’, in *Proceedings of the International Symposium on Engineering Lessons Learned from the 2011 Great East Japan Earthquake*, pp. 665–674.
- Tosi, L., Teatini, P. and Strozzi, T. (2013) ‘Natural versus anthropogenic subsidence of Venice’, *Scientific Reports*, 3. doi: 10.1038/srep02710.
- Urayasu City (2009) *The Project of reclaimed land*. Available at: <http://www.city.urayasu.lg.jp/shisei/profile/profile/1000020.html> (Accessed: 16 March 2018).
- Urayasu City population statistics* (2018). Available at: <http://www.city.urayasu.lg.jp/shisei/toukei/jinko/1002267.html> (Accessed: 20 March 2018).
- Vázquez-Jiménez, R. *et al.* (2018) ‘Thresholding Algorithm Optimization for Change Detection to Satellite Imagery’, *Colorimetry and Image Processing*. doi: 10.5772/intechopen.71002.
- Watson, R. C. (2009) *Radar origins worldwide : history of its evolution in 13 nations through World War II*. Trafford Publishing.
- Werner, C. *et al.* (2004) ‘Interferometric point target analysis for deformation mapping’, in *IGARSS 2003. 2003 IEEE International Geoscience and Remote Sensing Symposium. Proceedings (IEEE Cat. No.03CH37477)*. IEEE, pp. 4362–4364. doi: 10.1109/IGARSS.2003.1295516.
- WILEY and A., C. (1985) ‘Synthetic aperture radars-A paradigm for technology evolution’, *IEEE Trans. Aerosp. Electron. Syst.*, 21(3), pp. 440–443. Available at: <https://ci.nii.ac.jp/naid/20001396512> (Accessed: 15 May 2019).
- Xu, B. (2013) ‘Consideration of Geomechanics for In-situ Bitumen Recovery in Xinjiang, China’, in *SPE Heavy Oil Conference-Canada*. doi: 10.2118/165414-ms.
- Xu, B. *et al.* (2016) ‘Coastal subsidence monitoring associated with land reclamation using the point target based SBAS-InSAR method: A case study of Shenzhen, China’, *Remote Sensing*, 8(8). doi: 10.3390/rs8080652.
- Yamagishi, H. and Yamazaki, F. (2018) ‘Landslides by the 2018 Hokkaido Iburi-Tobu Earthquake on September 6’, *Landslides*. Springer Berlin Heidelberg, 15(12), pp. 2521–2524. doi: 10.1007/s10346-018-1092-z.
- Yang, Q. *et al.* (2015) ‘InSAR monitoring of ground deformation due to CO<sub>2</sub> injection at an enhanced oil recovery site, West Texas’, *International Journal of Greenhouse Gas Control*. Elsevier, 41, pp. 20–28. doi: 10.1016/J.IJGGC.2015.06.016.
- Yasuda, S. *et al.* (2012) ‘Characteristics of liquefaction in Tokyo Bay area by the 2011 Great East Japan Earthquake’, *Soils and Foundations*, 52(5), pp. 793–810. doi: 10.1016/j.sandf.2012.11.004.
- Zebker, H. A. *et al.* (1994) ‘On the derivation of coseismic displacement fields using differential radar interferometry: The Landers earthquake’, *Journal of Geophysical Research: Solid Earth*. John Wiley & Sons, Ltd, 99(B10), pp. 19617–19634. doi: 10.1029/94JB01179.

- Zebker, H. A. and Villasenor, J. (1992) 'Decorrelation in interferometric radar echoes', *IEEE Transactions on Geoscience and Remote Sensing*, 30(5), pp. 950–959. doi: 10.1109/36.175330.
- Zhang, L., Ding, X. and Lu, Z. (2011) 'Modeling PSInSAR Time Series Without Phase Unwrapping', *IEEE Transactions on Geoscience and Remote Sensing*, 49(1), pp. 547–556. doi: 10.1109/TGRS.2010.2052625.
- Zhang, L., Ding, X. and Lu, Z. (2015) 'Ground deformation mapping by fusion of multi-temporal interferometric synthetic aperture radar images: a review', *International Journal of Image and Data Fusion*. Taylor & Francis, 6(4), pp. 289–313. doi: 10.1080/19479832.2015.1068874.
- Zhou, L. *et al.* (2017) 'Wuhan surface subsidence analysis in 2015-2016 based on sentinel-1A data by SBAS-InSAR', *Remote Sensing*, 9(10). doi: 10.3390/rs9100982.
- Zhu, W. *et al.* (2014) 'Landslide monitoring by combining of CR-InSAR and GPS techniques', *Advances in Space Research*. doi: 10.1016/j.asr.2013.12.003.
- Zou, W. *et al.* (2009) 'Improvement of the Accuracy of InSAR Image Co-Registration Based On Tie Points – A Review', *Sensors*. Molecular Diversity Preservation International, 9(2), pp. 1259–1281. doi: 10.3390/s90201259.